Structure and Dynamics of Water and Ions in Solution - Soft X-Ray Absorption and Emission Studies

im Fachbereich Physik der Freien Universität Berlin
eingereichte Dissertation

zur Erlangung des akademischen Grades der
Doktorin der Naturwissenschaften (Dr. rer. nat.)

vorgelegt von

Kathrin Maria Lange

Berlin

Februar 2012

1. Gutachter: Prof. Dr. Emad Flear Aziz Bekhit
2. Gutachter: Prof. Dr. Holger Dau
Disputation am 11.04.2012

Contents

1. Introduction

Even though it is one of the smallest existing molecules, our life is unimaginable without it: The water molecule. Its three aggregate states enable life on Earth. In its gaseous state, as water vapor, it is the main absorber of sunlight in the atmosphere, contributing to the greenhouse effect and a warm and comfortable life. Upon cloud formation the sunlight is backscattered, and this protects from global warming. As ice, for instance in glaciers, it shapes landscapes and as part of the cryosphere it determines our world's climate. Liquid water, as is found in the oceans, covers more than 70 % of the earth's surface. It is the natural habitat of hundreds of thousands of different species [28] and it is the main component of the human body, accounting for two thirds of its volume. Its capacity to ionize and to hydrate enables ionic charge transfer processes inside the body, as well as protein folding and function, earning water the surname "matrix of life". [113]
Accordingly, it is not surprising that for centuries, scientists have been interested in disclosing water's secrets, and its interaction with ions and biological molecules. Despite its size and omnipresence, water is far from being a typical molecule. [13] There are over 60 known anomalies, or instances where the behaviour of water differs from expectations. And often life depends on these anomalies. For example, its specific density behaviour prevents the bottoms of oceans and lakes from freezing, allowing survival of aquatic life in cold temperature. Further, a high heat capacity and a high thermal conductivity reduce local thermal fluctuations, which is important for the temperature control of our body or for a moderate climate and life conditions on earth, amongst other examples.
It is known that the origin of many of the complex and anomalous properties of water lies in the hydrogen bond network that water molecules form between each other. But the exact appearance of this network is still under discussion among scientists today. Even the number of hydrogen bonds per water molecule varies (depending on the method applied) between 2.2 and 3.5. [36, 122]
In the framework of this thesis an X-ray absorption (XA) and high resolution X-ray emission (XE) spectrometer on a liquid micro-jet was built in order to investigate the electronic structure of water molecules and of ions in heterogeneous media. An introduction to the water molecule and to hydrogen bonding as well as fundamental concepts of ion solvation are

presented in chapter 2. One of the research questions was which influence the hydrogen bond network has on the occupied and unoccupied molecular orbitals. In order to adress this question, X-ray absorption (XAS) and X-ray emission spectroscopy (XES) were carried out at the third generation synchrotron facility BESSY II of the Helmholtz-Zentrum Berlin at the undulator beamline U41 PGM. The basic principles of XAS and XES are presented in chapter 3, followed by information about the synchrotron and the beamline (see 4.1 and 4.2).
The main challenge was the development and setting up of a novel spectrometer, the LiXEdrom, which allows the investigation of the electronic structure of liquid systems via these photon-in photon-out processes in the soft X-ray regime. Using soft X-rays the K-edges of life elements like oxygen and nitrogen can be investigated, as well as the L-edges of transition metals. For a long time, the required vacuum conditions for measurements with soft X-rays prevented the investigation of liquid samples. Techniques for bypassing this problem are either to separate the vacuum and the liquid by using a thin X-ray transparent membrane, or the micro-jet technique, [39] where a liquid jet of 20μm thickness is pumped into the vacuum with a speed of around 40 m/s. In the new LiXEdrom setup the micro-jet technique is used for measuring X-ray absorption and high resolution X-ray emission spectra in a totally membrane-free configuration. Also measurements with a membrane-containing flowcell are presented in this thesis, which were carried out using the Liquidrom setup. Details about both setups can be found in chapter 4.
Before interpreting spectral data, the spectra need to be normalized, background corrected or further treated. In chapter 5 this processing is explained for the presented spectra. Furthermore, effects that can distort the spectra are discussed.
In the chapter on the experimental studies, the results of this thesis are presented. It begins with the first measurements of the LiXEdrom spectrometer, where the oxygen K-edge of pure water and the nickel L-edge of aqueous nickel ions at varying concentration were investigated using XAS and XES (see section 6.1). After this proof of principle, the hydrogen bond network of water was in the focus of investigation. In a pre-study based on FT-IR spectroscopy, the changes of the hydrogen bond network of water upon dilution in different oxygen-free organic solvents were systematically analysed. For the further oxygen K-edge XA and XE studies, acetonitrile was chosen as a solvent. Upon varying the water-acetonitrile ratio the hydrogen bond coordination per water molecule changes, and the influence of this effect on the XA and XE spectra was investigated (see section 6.3).
In the following study the hydrogen bond surrounding was varied upon dilution with acetonitrile, too. Here, instead of H_2O, D_2O was used, where the hydrogen atoms are replaced by the isotope deuterium. Due

to the heavier deuterium the proton dynamics are in D_2O slower than in H_2O. By this study the effect of the dynamics could be separated from the effect of hydrogen bonding on the XE spectra (see section 6.4).
The solvation of ions and the driving forces behind it are the topic of the last presented study. Whereas a large number of datasets exists concerning the macroscopic, thermodynamic behaviour of ion-solutions, microscopic pictures of the electronic structures around the ions are rather scarce. In order to explain the discrepancies between theories and experiments regarding the non-ideality in the free energy of solvation, we present a microscopic picture of sodium ions dissolved in water-alcohol mixed solvents upon measuring Na K-edge XA spectra using the Liquidrom flowcell setup. The effect of counter-ions was also considered. The obtained microscopic picture of the solvation shell delivers valuable information about the thermodynamic behaviour of these systems. Furthermore a radiation induced effect in some of these systems will be presented, highlighting the specific role of the water molecule and its strong hydrogen bond.

2. Water and Aqueous Solutions

The water molecule H_2O is behind H_2 the most abundant molecule in our universe. Water is the basis of all known life; it is required for processes ranging from enzymatic activity up to ecosystem function. Despite the apparent simplicity of the water molecule up till date the special properties and anomalies of water are subject of intensive investigation and debate. [13, 74] The hydrogen bond network is playing a key role for the unusual behavior of water in ice and liquid phase, making it a focus of interest. In the following sections some introductory information about the isolated water molecule and its molecular orbitals are presented, as well as about the hydrogen bond interaction of water molecules in liquid phase. It is briefly explained which information can be revealed via soft X-ray spectroscopies and FT-IR spectroscopy about the electronic and the vibrational structure of the water molecules and how this can be correlated to the hydrogen bonds. A detailed theoretical and experimental description of these methods follows in chapter 3 and 4. Furthermore the role of water as a solvent for ionic compounds is discussed and theoretical descriptions of the solvation process are presented.

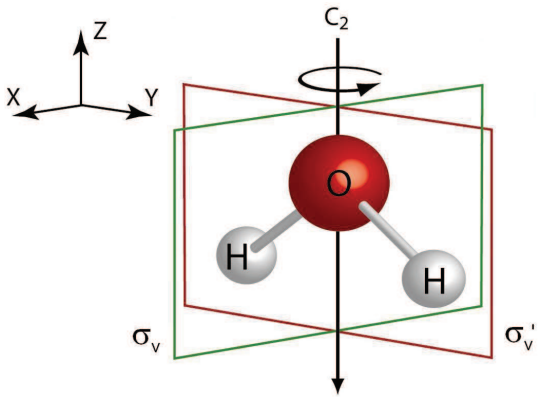

Figure 2.1.: Water molecule with the rotational symmetry axis C_2 and the two symmetry planes σ_v and σ_v'

2.1. The Isolated Water Molecule

Water is composed of two hydrogen atoms which are in v-shape covalently bound to an oxygen atom. In an isolated water molecule the O-H distance is of around 0.96 Å and the H-O-H angle of around 104.5°. [31] The negative centre of charge is found near the oxygen atom and the positive one between the two hydrogen atoms. Due to the v-shape the negative and positive centre of charge do not coincide, which causes a molecular dipole moment of $6.19 \cdot 10^{-30}$ Cm and the polar nature of water. [31]

2.1.1. The Molecular Orbitals of Water

In this thesis soft X-ray spectroscopies were applied to probe the molecular orbitals (MOs) of water. For an isolated water molecule the ground state configuration of the occupied MOs is:

$$(1a_1)^2(2a_1)^2(1b_2)^2(3a_1)^2(1b_1)^2 \tag{2.1}$$

The first two subsequent unoccupied MOs are named $4a_1$ and $2b_2$. Using the Gaussian 03 program [42] the equipotential surfaces of the MOs were calculated and are presented in figure 2.2. The labeling of the MOs is based on their symmetry. The water molecule belongs to the C_{2v} symmetry group. Its 2-fold rotational axis C_2 and the two symmetry planes σ_v and σ'_v are shown in figure 2.1. From the character table of the C_{2v} point group (see Table 2.1) the symmetries of each water orbital can be identified. The lowest two MOs $1a_1$ and the bonding $2a_1$ are mainly composed of the 1s and 2s atomic orbitals of the oxygen and are accordingly almost spherical (see figure 2.2 a and b). The $1b_2$ state is of bonding character and consists of a linear combination of O $2p_y$ and H 1s orbitals, whereas the $3a_1$ state is composed of O $2p_z$ and H1s contributions. The non-bonding lone-pair $1b_1$ orbital has mainly O $2p_x$ character. The unoccupied $4a_1$ and $2b_2$ are antibonding orbitals. Further details about the atomic contributions to each molecular orbital based on Gaussian calculations are presented in the appendix.

C_{2v}	E	C_2	σ_v(xz)	σ'_v (yz)
A_1	1	1	1	1
A_2	1	1	-1	-1
B_1	1	-1	1	-1
B_2	1	-1	-1	1

Table 2.1.: Character table of the C_{2v} point group [98]

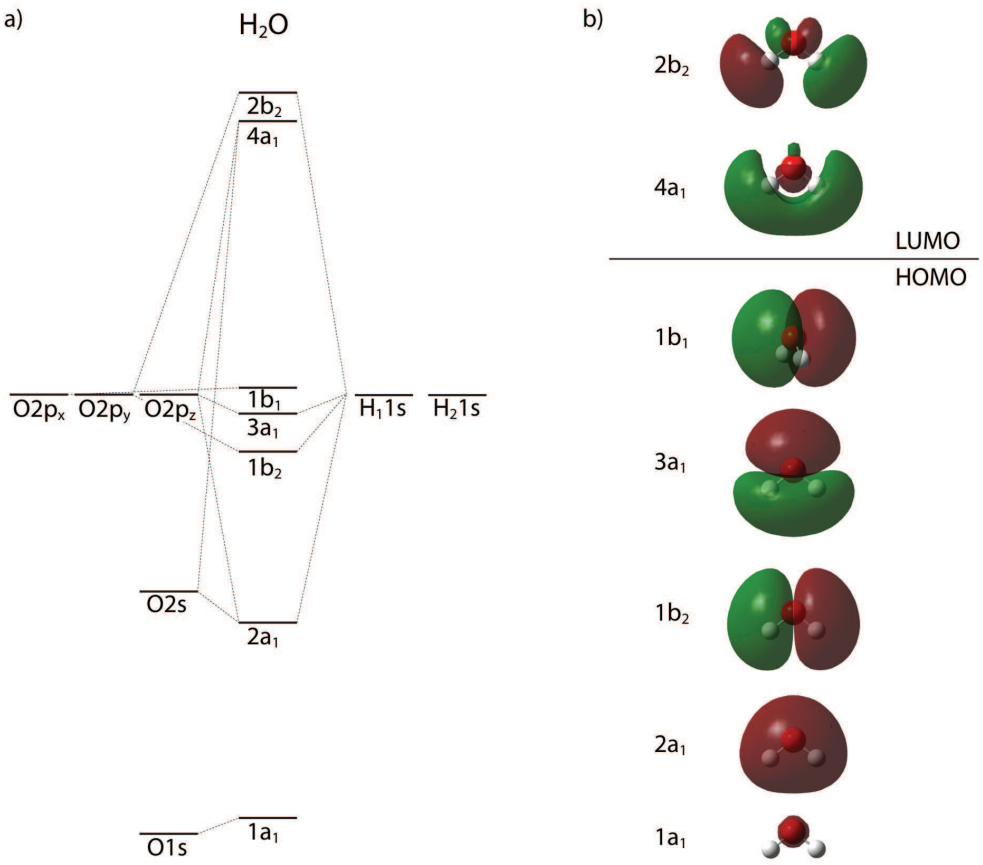

Figure 2.2.: a) Energy level diagram for one single water molecule b) The occupied and the first two unoccupied molecular orbitals of a single water molecule. The orbitals were calculated using the Gaussian 03 program [42]

Using XES and XAS the occupied and the unoccupied molecular orbitals (MO) of a water molecule can be experimentally probed. [88] Note that both processes underlie the dipole selection rules, which allows to obtain also information about the symmetry of the MOs. In the XE process, a core-hole in the $1a_1$ level is created via photoexcitation. This hole is filled by the electrons of higher occupied MOs, which can emit upon relaxation a fluorescence photon. The energy of these fluorescence photons is characteristic for the electronic transition. By energy dispersive detection the unoccupied orbitals can be mapped. In figure 2.3a the XE [104] spectrum of gas phase water is presented. It shows the spectral features correlated to the occupied $1b_2$, $3a_1$ and $1b_1$ MOs. The bonding character of the $1b_2$ and $3a_1$ orbital lead to a broadening of the spectral features. In the XA process the unoccupied MOs are mapped. As a function of incoming X-ray energy the excitation rate is recorded. The resulting spectrum for water in the gas phase is shown in figure 2.3b. The peaks originating

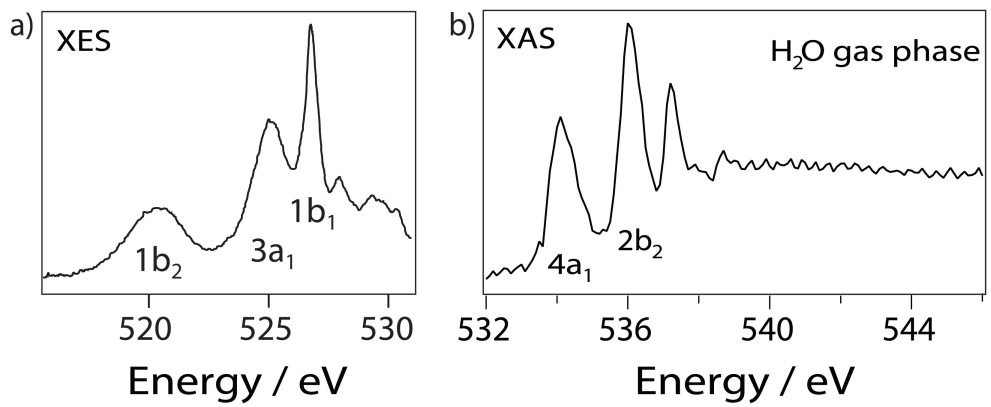

Figure 2.3.: a) X-ray emission [104] and b) X-ray absorption spectra [69] of gas phase water. The correlation of the peaks to the respective occupied and unoccupied molecular orbitals is indicated in the figure.

from the $4a_1$ and $2b_2$ MO can be identified. Energetically above, higher unoccupied MOs and Rydberg states follow.
In liquid phase the electronic structure of the isolated water molecule is distorted due to interactions with neighboring water molecules. Probing the electronic structure of water molecules in liquid phase allows, accordingly, deriving information about these interactions, such as hydrogen bonding, as will be discussed in the next section.

2.2. The Hydrogen Bond of Water

In the liquid phase the above presented MO of the isolated water molecule are affected by the interactions with the neighboring water molecules. The hydrogen atoms, which are covalently bound to the oxygen, are partially positively charged and can thus interact with the electronegative oxygen of another water molecule. Upon creation of a hydrogen bond the intramolecular distance between the oxygen and the hydrogen of the donor molecule increases, whereas the intermolecular distance between the oxygen atoms of the two water molecules is decreased. The strength of such intermolecular hydrogen bonds lies in between the weaker van der Waals interaction and the stronger covalent bond. [55] Per water molecule two hydrogen bonds can be donated via the hydrogen atoms and two accepted in the region of the lone-pairs. Ideally this leads to a tetrahedral arrangement of the water molecules, as approximately found in ice phase. Upon melting this structure becomes more disordered. Fluctuations in the hydrogen bond network become possible, an average lifetime of a hydrogen bond is around 1 ps and the molecules have thus a chance to approach closer to each other. [13] This is causing the well known density anomaly

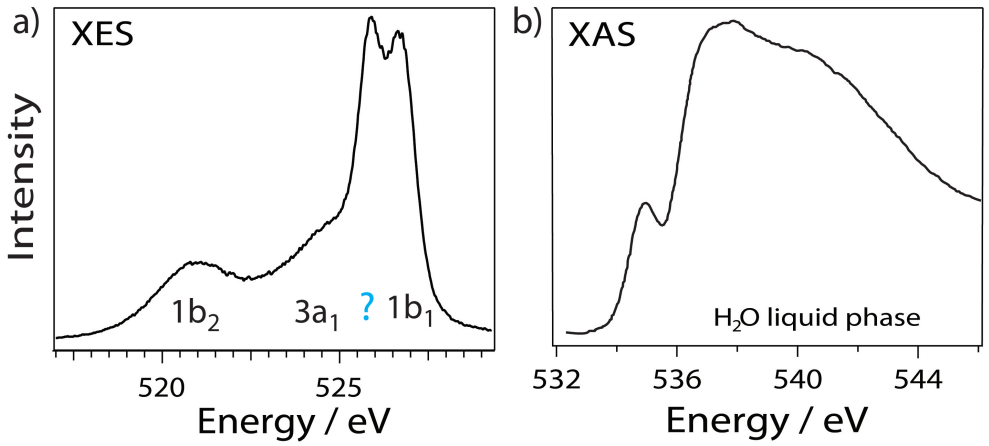

Figure 2.4.: a) X-ray emission [66] and X-ray absorption spectra [122] of liquid water. The correlation of the peaks to the respective occupied and unoccupied molecular orbitals is for the liquid phase more complex than for gas phase and is discussed in the text.

on freezing. [13] The predicted average number of hydrogen bonds per water molecules in liquid phase is under debate, varying between 3.5 (based on neutron scattering [36]) and 2.2 (based on XAS combined with density functional theory (DFT) calculations [122]). The concept of defining the number of hydrogen bonds per molecule has however some ambiguity, since it depends on the geometric definition of the hydrogen bond with regard to the maximum O-O distance in dependence of the distortion angle.

The changes of the electronic structure due to condensation effects can be revealed upon comparing the XA and XE spectra of gas phase water (see figure 2.3) with the respective spectra of liquid water (see figure 2.4). In the XA spectrum of liquid water a direct correlation to the MOs is not possible anymore. Three spectral features can be distinguished: A pre-edge around 535 eV, a main-edge around 537 eV and a post-edge around 542 eV. Based on experimental and theoretical approaches, these features were correlated to water molecules with different hydrogen bond coordinations. [82, 122] The pre- and main-edge intensities are assumed to be caused by configurations with broken or weak hydrogen bonds, whereas the post-edge intensity is rather correlated to strong hydrogen bonds and tetrahedral structures. In the XE spectrum the most drastic change is the appearance of a fourth spectral feature in the liquid phase spectrum. This additional feature was experimentally observed for the first time by Fuchs *et al.*, using a membrane-containing high-resolution XE spectrometer. [43] In anterior publications the energy resolution was usually not sufficient to resolve the splitting of the sharp spectral feature. [50] Until now the origin of this additional feature is under debate. [43, 94, 116, 118] The newly developed spectrometer, in which the samples are not con-

tained behind a membrane but provided by a liquid micro-jet, could first of all clarify, whether this feature is a membrane induced artifact (see section 6.1). [66] Furthermore, the influence of the hydrogen bonds on the MOs was investigated by varying the number of hydrogen bonds among water molecules in water-acetonitrile mixtures and recording respective XA and XE emission spectra (see section 6.3). [67] To determine, at which water concentration the water molecules are isolated within the organic solvents, FT-IR spectroscopy was applied as a complementary approach (see section 6.2), probing the vibrational modes of water. [65]

2.2.1. The Vibrational Modes of Water

Fourier transform infrared (FT-IR) measurements in the mid-infrared region ($\approx$ 4000-400 cm^{-1}) were carried out in this thesis. Water shows in this mid-infrared region strong absorption bands. They are correlated to vibrational excitations of the water molecule. The main vibrations are the symmetric stretch vibration ν_1, the bending vibration ν_2 and the asymmetric stretch vibration ν_3 (see figure 2.5). For gas phase water ν_1 is located at 3657 cm^{-1}, ν_2 at 1595 cm^{-1} and ν_3 at 3756 cm^{-1}. [129] Furthermore, overtone bands can be observed e.g. for the ν_2 vibration, where the absorption of a photon leads to a double excited vibrational state. The respective absorption band is found at around twice the energy of the normal absorption band. In the liquid phase the rotational modes are due to the hydrogen bonds hindered, leading to librational motions. Energetically, mainly the stretching modes are affected by hydrogen bonding. Typically these vibrations show a shift to lower frequencies and an increase of intensity in the IR spectra upon hydrogen bond formation and strengthening. [52] This can be observed by comparing the IR spectra of liquid water and ice (see figure 2.6). The red-shift can be understood in terms of a lengthening and weakening of the intramolecular O-H bond. [52] For a series of mixtures with water the frequency shift of the vibrational bands can be accordingly used as a measure for the binding energy, as presented in section 6.2.

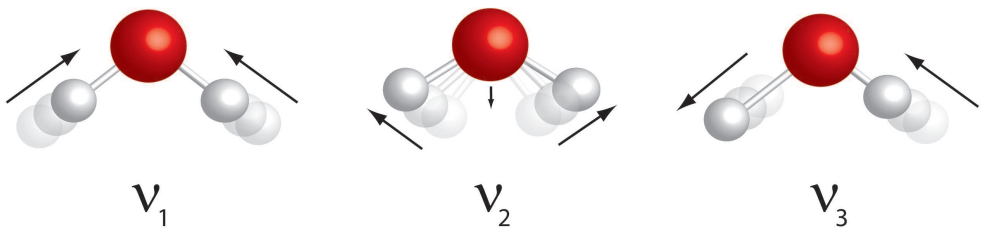

Figure 2.5.: The main vibrational modes of the water molecule: the symmetric stretch ν_1, the bending ν_2 and the asymmetric stretch vibration ν_3

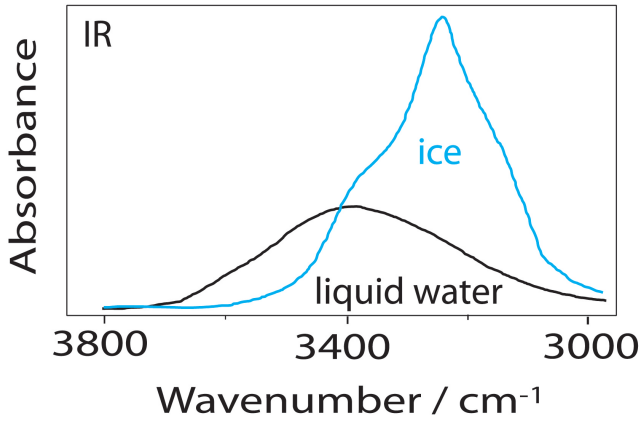

Figure 2.6.: IR absorption spectra of liquid water and ice. [27,101] The broad features contain amongst others the modes of the symmetric and asymmetric stretch vibration ν_1 and ν_3 as well as the overtone vibration $2\nu_2$. The stronger hydrogen bonds in ice lead to a red-shift and an increase in absorbance. [52]

2.3. Aqueous Solutions of Ions

Its small size, polar nature and high dielectric constant make water a highly efficient solvent for polar and ionic compounds and salts. In this thesis the special role of water as a solvent was investigated on ions in aqueous solutions in comparison to other solvents like alcohol or water-alcohol mixtures (see section 6.5).
In an ionic solid the cations and anions are arranged in an extended three-dimensional lattice (see figure 2.7a). [51] Dissolving this crystal in a solvent requires that the sum of the electrostatic interaction between the ions and the solvent and the entropy exeeds the sum of electrostatic ion-ion interaction and the entropy inside the crystal. The polar nature of the water molecules allows Coulomb interaction between the electronegative oxygen and cations and between the partially positively charged hydrogens and anions. The water molecules orient themselves accordingly with the hydrogen atoms towards anions and with the oxygens towards the cations of a crystal. If the attractive force of the oriented water molecules is sufficient, it can overcome the attractive force between the cations and anions and remove them from the crystal structure. The water molecules surround the ions and create a hydration shell. Figure 2.7b shows the conventional view of the orientation of the water molecules in such solvation shell. [51] Neutron scattering results suggest rather an orientation as presented in figure 2.7c. [109] The high dielectric constant of the water molecule allows a shielding of the Coulomb attraction between ions of opposite charge, preventing their accumulation.

Theoretically, the ionic solvation was first described quantitatively by the Born model of the free enthalpy of solvation. [19] In this simplest model the ions are regarded as charged hard spheres and the influence of the solvent is represented by a uniform dielectric constant ϵ:

$$\Delta G_{Born} = -\frac{Z^2 e^2}{8\pi\epsilon_0 R}(1 - \frac{1}{\epsilon}) \tag{2.2}$$

Here, ΔG_{Born} is the Gibbs energy of solvation for an ion with point charge $Z{\cdot}e$ and of radius R. Further refinement of the model was done, e.g., with the Debye-Pauling model, which includes a varying dielectric constant in the surrounding of an ion, in order to represent the saturation of the dielectric in the field of the ion. [41] Further approaches include variation of the ionic radii. In more detailed models, based on methods of statistical mechanics, the solvent medium itself is treated as an assembly of many single identical particles. For these Hamiltonian models the challenge lies in finding an appropriate potential energy function, describing the interaction between the particles of the configuration. For the mean spherical approximation (MSA) model ions are considered as charged hard spheres and the solvent molecules as hard spheres with multipoles (dipoles, quadrupoles). The MSA approach delivers quite accurate results for the correlation functions and thermodynamic coefficients of hard spheres, which can be used in a next step for perturbation methods of statistical mechanics with more realistic potentials. Hybrid models combine the Hamiltonian and the Born approach by treating the interaction between ion and first solvation shell solvent molecules in terms of intermolecular forces, whereas the interaction of this complex with the remaining solvent is calculated according to the Born model. All these mod-

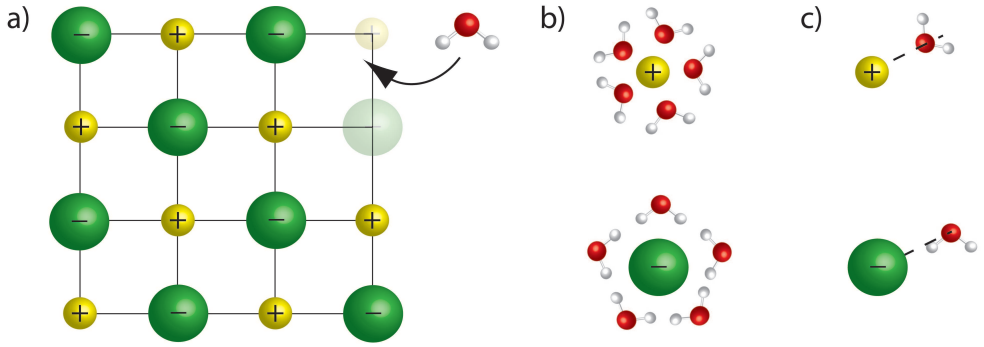

Figure 2.7.: Schematic of the solvation of cations an anions. a) shows the dissolving of the ionic crystal, b) the conventional picture of the hydration shell and c) the orientation of the water molecules in the hydration shell as revealed by neutron diffraction [13]

els represent however just an approximation to the real systems, showing often not insignificant deviations from experimental data. In section 6.5 of this thesis spectroscopic studies of sodium halide solutions are presented which aim to resolve disagreement between experimental data and theoretical predictions based on MSA theory by revealing information about the first solvation shell. There, the theoretical models of ion solvation and the agreement with experimental results are further discussed.

3. Soft X-Ray Spectroscopies

X-ray spectroscopic techniques are widely used for disclosing the electronic and geometric structure of atoms, molecules, solids, liquids and surfaces. The K-edges of elements essential for life like oxygen and nitrogen, and the L-edges of transition metals like iron, nickel and cobalt lie in the regime of soft X-rays (from ca. 30 eV to 1500 eV). In this work soft X-ray based experimental techniques were used for investigating the electronic structure of water molecules as well as of ions in solution. In this section the fundamentals of these techniques, namely X-ray absorption spectroscopy (XAS) specifically focusing on the near edge X-ray absorption fine structure (NEXAFS) and X-ray emission spectroscopy (XES) including resonant inelastic scattering (RIXS) are presented. References for more detailed theoretical descriptions can be found at the end of each section.

3.1. Interaction of X-Rays with Matter

When an X-ray beam of intensity I_0 passes through matter, it is attenuated. The intensity I after transition through a sample of thickness d and density ρ is given by:

$$I = I_0 e^{-\mu d \rho} \tag{3.1}$$

where the mass attenuation coefficient μ comprises the different interaction processes of light with matter. In the X-ray regime these are mainly the photoelectric excitation, and coherent and incoherent scattering. The probability for each processes is represented by the respective energy dependent coefficients σ_p, σ_{cs} and σ_{is}. In the soft X-ray regime, which was the photon energy mainly used in this work, the contribution of the cross section σ_p, which is defined as the number of electrons excited per unit time, divided by the number of incident photons per unit time, is dominantly contributing to the total cross section σ_{tot} (see figure 3.1). The theoretical description of the photoelectric excitation will be discussed in the following X-ray absorption section.

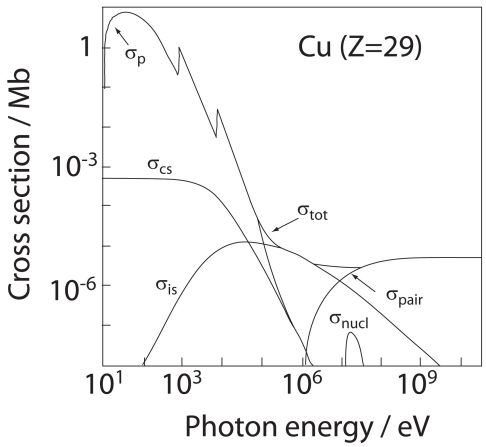

Figure 3.1.: a) Using the example of the transition metal atom Cu the X-ray cross sections for different interactions with light are presented, where σ_p, σ_{cs} and σ_{is} are the cross sections for X-ray absorption, coherent scattering and incoherent scattering, respectively. σ_{pair} and σ_{nucl} are the cross sections for pair production and nuclear photoabsorption, which lie out of the soft X-ray regime. σ_{tot} is the sum of all contributions. [54]

3.2. X-ray absorption

3.2.1. Theoretical approach

In the photoelectric absorption process an electron is excited from an initial state ψ_i to a final state ψ_f upon creation of a core hole. Quantum-mechanically, this process can be described by time-dependent perturbation theory, [23] where H_0 represents the molecular Hamiltonian and $V(t)$ the time-dependent interaction with an plane electromagnetic wave of vector potential $\boldsymbol{A}(t)$, giving the total Hamiltonian:

$$H = H_0 + V(t) \tag{3.2}$$

The time-dependent interaction between the incoming wave and the electron of charge e and the mass m can be described as follows:

$$V(t) = -\frac{e}{m}\mathbf{P}\cdot\mathbf{A} - \frac{e}{m}\mathbf{S}\cdot\mathbf{B} + \frac{e^2}{2m}\mathbf{A}^2 \tag{3.3}$$

The third term contains a square dependence on the amplitude A_0 of the vector potential $\mathbf{A}$. For typical light source intensities it can be neglected with respect to the first and the second term, which linearly depend on A_0. Setting up the ratio between the first and the second term reveals

that the latter one, that describes the interaction of the magnetic moment of the electron spin **S** with the magnetic field **B**, can be neglected as long as:

$$\frac{a_0}{\lambda} \ll 1, \tag{3.4}$$

where a_0 is the Bohr radius and λ the wavelength of the incoming light. This condition is fulfilled for the photon energies of the soft X-ray regime. Accordingly only the first term containing the momentum operator **P** is considered in the following:

$$V(t) = \frac{e}{mc}\boldsymbol{A}(\mathbf{t}) \cdot \boldsymbol{P} \tag{3.5}$$

with

$$\boldsymbol{A}(\mathbf{t}) = \epsilon\frac{A_0}{2}(e^{i(\boldsymbol{k}\cdot\boldsymbol{x}-wt)} + e^{-i(\boldsymbol{k}\cdot\boldsymbol{x}-wt)}) \tag{3.6}$$

where m and e are the mass and the charge of the electron and ω, k and ϵ the frequency, the wave vector and the polarization vector of the incoming photon, respectively. In the so called dipole approximation only the first term of the Taylor series ($e^{\pm i\boldsymbol{kx}} = 1 \pm i\boldsymbol{kx} - ...$) is considered. For soft X-rays, e.g. for the oxygen K-edge at 540 eV and atoms or small molecules like water, $k \cdot x \ll 1$ is satisfied, which justifies this simplification. Based on the dipole approximation the transition probability per unit time W_{fi} from ψ_i to ψ_f can be described by Fermi's golden rule [111]:

$$W_{fi}(E) = \frac{\pi e^2 A_0^2}{2\hbar c^2 m^2} |\langle\psi_f| \epsilon \cdot \mathbf{P} |\psi_i\rangle|^2 \rho_f(E) \tag{3.7}$$

where ρ_f is the energy density for the final states. The absorption cross section σ_p is defined as the transition rate W_{fi} per unit photon flux and can be accordingly described as follows [111]:

$$\sigma_p = \frac{4\pi^2 e^2}{m^2 c\omega} |\langle\psi_f| \epsilon \cdot \mathbf{P} |\psi_i\rangle|^2 \rho_f(E) \tag{3.8}$$

If the dipole matrix element in equation 3.8 between the states $|\psi_i\rangle$ and $\langle\psi_f|$ differs from zero, an electric dipole transition may take place. Otherwise the transition is dipole-forbidden. By inserting the wavefunctions for the initial and final states, the following selection rules for dipole transitions with regards to the angular momentum quantum number ℓ and magnetic quantum number m can be derived:

$$\Delta\ell = \pm 1 \tag{3.9}$$

$$\Delta m = -1, 0, +1 \tag{3.10}$$

More details about the theoretical description of the XA process, the absorption cross section and the selection rules can be found in literature, e.g. in references [23] and [111].

3.2.2. Experimental approach

A direct way to determine experimentally the absorption cross section is to measure according to equation 3.1 the incoming and the transmitted X-ray intensity upon scanning through the binding energy of a core shell. This approach is however limited since it requires for each sample an energy dependent optimization of thickness and/or concentration. A simpler and often followed approach is to determine the absorption of a sample indirectly through concomitant processes. After a finite lifetime the core-hole created in the absorption process collapses. It is filled by an electron of lower binding energy. The loss of potential energy can lead to competing processes, of which the two most important are the ejection of an Auger electron and the emission of a fluorescence photon. A

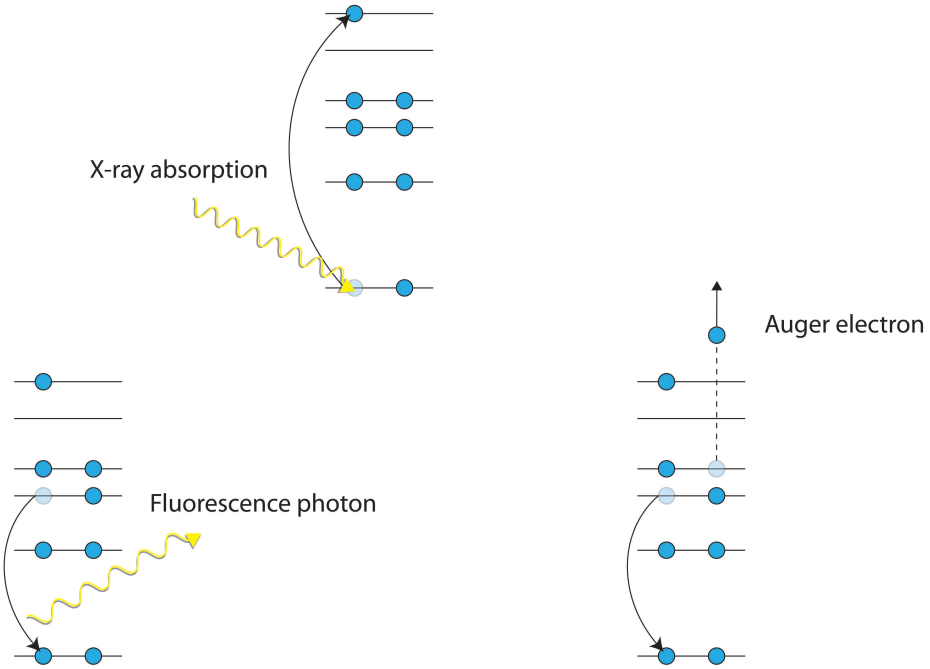

Figure 3.2.: The absorption of an X-ray photon leads to a core excited state as shown in the top of the figure. The relaxation can take place via fluorescence decay or via Auger electron decay.

schematic of these processes is presented in figure 3.2. The total electron yield (TEY) and the total fluorescence yield (TFY) are assumed to be for diluted or thin samples proportional to the absorption cross section (the limits of this assumption are discussed in detail in chapter 5) and are therefore often used for recording X-ray absorption spectra. The energy dependent probability for each process is presented in figure 3.3. Upon core-excitation with soft X-ray photons the emission of Auger electrons is the dominant process. The high yield and the short mean free path of electrons makes the electron detection the method of choice for surface or near-surface measurements. Even though orders of magnitude less efficient, the TFY is usually chosen when the bulk structure of a sample is of interest. A further advantage of the detection of photon compared to electron yield is that it is insensitive to sample charging and can be carried out also in presence of electric or magnetic fields. Also the use of membranes for separating a liquid sample from the vacuum (see section 4.3.1) is only possible for photon detection.
For measuring absorption spectra, the incoming light is scanned through the binding energy of a core shell. The abrupt increase of the absorption cross section gives rise to an absorption edge. The resulting spectra can be divided into two spectral regions: the near edge region and the extended region. For near edge X-ray absorption spectroscopy (NEXAFS), which was used in this thesis, the energetic region close to the edge-jump is of interest. It represents excitations from a core level to the unoccupied electronic states. The nature of these unoccupied states, e.g. their energetic position or width, is characteristic for a molecular species. Accordingly, NEXAFS can be used for the identification of molecular species and can reveal information about the interaction of the unoccupied molec-

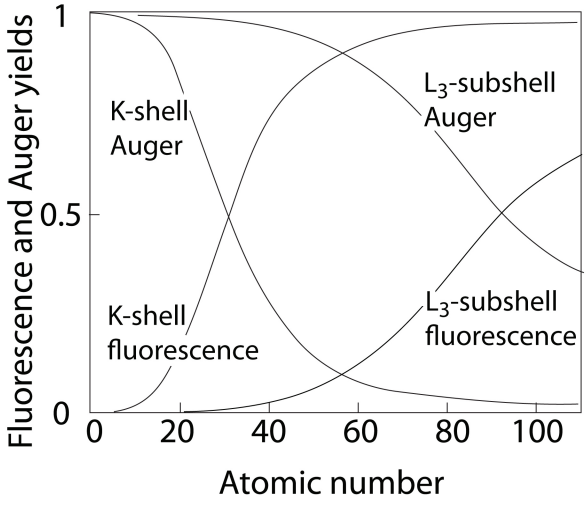

Figure 3.3.: Fluorescence vs. Auger yields for K- and L_3-shells in dependence of the atomic number [3]

ular orbitals with the surrounding. Since the electron transitions follow the dipole selection rules (see section 3.2.1), NEXAFS data furthermore allows conclusions on the local symmetry of the molecules. More details about NEXAFS spectroscopy can be found in reference [111].
The extended X-ray absorption fine structure (EXAFS) of an absorption spectrum can reveal information about the local geometric structure of the surrounding of a probed atom. In the extended region behind the absorption edge the absorption cross sections shows oscillations. These are caused by scattering events of the electron removed during the photo absorption process on neighboring atoms. By using Fourier transform procedures information about the distance of the probed atom to the nearest neighbors as well as the coordination number can be derived. Further details about EXAFS spectroscopy can be found in reference [114].

3.3. X-Ray Emission

In the previous section the XE process was presented as one decay channel after the XA process (see figure 3.2). Besides probing the unoccupied states via the TFY mode, the XE photons can reveal valuable information about the occupied orbitals of an atom or molecule. For this, the photon energy of the emission photons is of relevance. There are two approaches for describing the process of photoinduced emission theoretically. In the two-step model the process of absorption and emission are considered as two decoupled processes. Accordingly, the transition probability to the final state is described by the product of the probability of the excitation to the intermediate state (the absorption process) and the probability for the relaxation to the final state (the emission process). This model is time independent so that it cannot reveal information about the dynamics of a system. It is valid, when only one intermediate state exists, so that there is only one possible channel for excitation as well as one for relaxation. When several intermediate states are accessible the various channels can interfere and the two-step model cannot be applied. The two-step model is a good approximation, when the electron is excited to states of sufficiently long lifetime. Practically this can be the case for states significantly above the threshold, leading to the ionization of the molecule. In this thesis such spectra are called non-resonantly excited X-ray emission spectra.
When the lifetime of the intermediate state is relatively short, the two-step model of absorption and emission is not valid anymore. Due to interference effects, the emission process cannot be considered to be decoupled from the absorption. The process has to be treated then as a one-step scattering process, called resonant inelastic X-ray scattering (RIXS), as

will be presented in the following. [45] The differential cross section for the scattering of an incoming photon with the frequency ω into a solid angle Ω can be described based on second order perturbation theory. It describes the transition from an initial state i to a final state f through an intermediate state m, which appears by including the second order of the perturbation theory:

$$\frac{d^2\sigma(\omega',\omega)}{d\omega' d\Omega} = r_0^2 \frac{\omega'}{\omega} \sum_f |F_f|^2 \Delta(\omega' + \omega_{fi} - \omega, \Gamma_f) \tag{3.11}$$

where r_0 is the classical electron radius, ω' the frequency of the scattered photon, ω_{fi} the frequency of the transition from the initial to the final state, Γ_f the final state life time broadening and Δ a Lorentzian function with the half-width at half-maximum Γ which reflects the energy conservation law. The Kramers-Heisenberg formula [63] gives a description for the scattering amplitude F_f:

$$F_f = (\boldsymbol{\epsilon}' \cdot \boldsymbol{\epsilon}) \langle f | \sum e^{i(\mathbf{p}'-\mathbf{p})\mathbf{r}} |i\rangle \qquad direct \tag{3.12}$$

$$-\sum_n \sum_m \omega_{mf}\omega_{mi} e^{i(p'-p)R_n} \Big(\frac{\boldsymbol{\epsilon}' \cdot \boldsymbol{D}^+_{fm} \boldsymbol{\epsilon} \cdot \boldsymbol{D}_{mi}}{\omega - \omega_{mi} + i\Gamma_m} \qquad resonant$$

$$- \frac{\boldsymbol{\epsilon} \cdot \boldsymbol{D}^+_{fm} \boldsymbol{\epsilon}' \cdot \boldsymbol{D}_{mi}}{\omega' + \omega_{mi}} \Big) \qquad non\ resonant$$

where $\boldsymbol{\epsilon}$ and $\boldsymbol{\epsilon}$' are the polarization vector for the incoming and the scattered photon, respectively, $\boldsymbol{p}$ and $\boldsymbol{p}$' are the X-ray photon momentum before and after scattering, $\boldsymbol{D}$ the total electronic dipole moment of the atom or molecule, Γ_m the lifetime width of the intermediate state and R_n is the coordinate of the core-excited atom. The summations are over all coordinates n of the Z electrons and over all intermediate states m. As indicated in equation 3.12 there are three qualitatively different contributions to the Kramers-Heisenberg scattering amplitude, representing the direct, the resonant and the non-resonant scattering process. The meaning of these three contributions can be best visualized in a Feynman diagram, where the different possible scattering processes are presented in space-time (see figure 3.4). In the case of resonant scattering the system is in the initial state i. After absorbing a photon at time t_1 it becomes state m until at t_2, upon emitting a photon, it changes into state f (figure

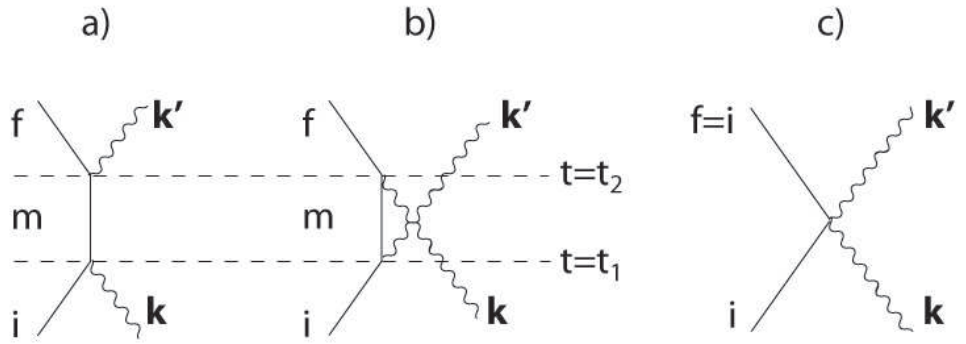

Figure 3.4.: Feynman diagram showing schematically the different possible scattering processes of light, a) resonant b) non-resonant c) direct scattering

3.4a). The intermediate state of the scattering process has virtual character, hence the time of the photon absorption as well as for the photon emission are not known exactly. Accordingly, the sequence of absorption and emission can be permutated, leading to the sequence shown in figure 3.4b. This process is represented by the non-resonant contribution in equation 3.12. Compared to the other terms, the non-resonant contribution is very small and can be neglected. The sudden scattering without intermediate state, which is also called Thompson scattering, is shown in figure 3.4c and described by the direct term. For the soft X-ray region only elastic scattering ($\omega = \omega'$) contributes to this term.
More details about the theoretical description of the RIXS process can be found in the literature, e.g. in references [45] and [103]. A detailed experimental description of XE spectroscopy is presented in the following chapter.

4. Experimental Methods and Setups

4.1. Synchrotron Radiation

Synchrotron radiation is the electromagnetic radiation which is emitted when relativistic charged particles are deflected in a magnetic field. The synchrotron radiation was already predicted theoretically in 1945 when the future Nobel Prize winner J. S. Schwinger developed a mathematical description of radiation from accelerated relativistic electrons. [106] Amongst others, this theory describes that for relativistic electrons the typical dipole radiation pattern is transformed to a strongly forward peaked distribution which gives synchrotron radiation its highly collimated property. Inquiring the reason of energy losses, the predicted synchrotron radiation was for the first time visually observed in 1947 at a betatron (a magnetic-induction electron accelerator) of the General Electric Research Laboratory in Schenectady, New York. [115] Recognizing its high potential, scientists soon moved from the initial parasitic operation at high energy facilities onto storage rings which were dedicated for the creation of synchrotron radiation. A further development to the so called third generation took place when storage rings were optimized for insertion devices like wigglers and undulators. An undulator as schematically shown in figure 4.1 is an array of closely spaced vertically oriented dipole magnets of alternating polarity. An electron beam passing through this array of magnets is forced by the magnetic field on a slalom course. The radiation cones that are emitted at each turn of the trajectory interfere with each other, leading to a highly collimated beam with a spectrum of a few energetically narrow peaks. The advantage of the synchrotron radiation from an undulator is its high spectral brightness (flux per area of radiation source, per solid angle of the radiation cone, per spectral bandwidth).
The BESSY II synchrotron, at which the experiments of this thesis were carried out, is a facility of the third generation. Free electrons are created via a hot cathode and are accelerated by an anode voltage up to an energy of 100 keV. Further acceleration takes place after injection into the orbit of the microtron which contains two deflection magnets of constant magnetic field strength and a high frequency linear accelerator. The energy gain by passing through the linear accelerator leads to an increas-

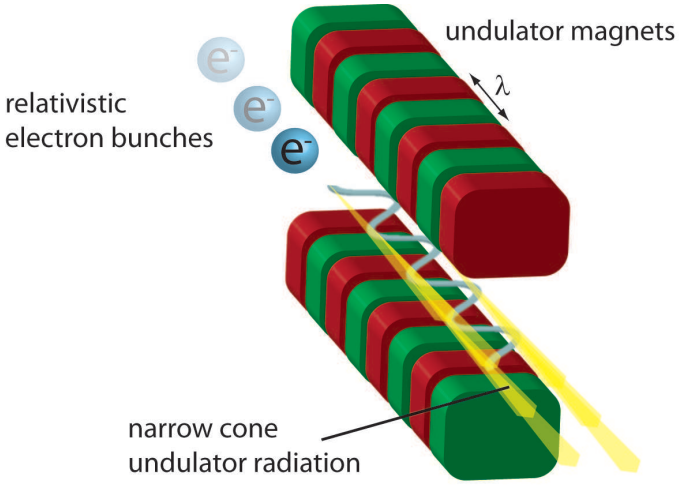

Figure 4.1.: Schematic depiction of the creation of synchrotron radiation within an undulator

ing turning radius of the electrons in the field of the deflection magnets. When the electrons reach an energy of 50 MeV they are passed into the synchrotron, where they are further accelerated to the final energy of 1.7 GeV by alternating fields of a cavity resonator. The field strength of the magnets, which hold the electrons on the synchrotron orbit, is continuously adapted to the increasing kinetic energy of the electrons. Through a transfer channel the electrons are afterwards injected into the storage ring, where bending magnets, wigglers, and undulators are used for the creation of the synchrotron radiation, which is transferred through the 46 beamlines to the experimental endstations. The measurements presented in this work were carried out at the undulator beamline U41 PGM (plain-grating monochromator), which will be presented in the following section.

4.2. Beamline U41 PGM

In order to measure liquid samples from a micro-jet of around 20 μm diameter, an X-ray source is required which provides an accordant small focus with a high flux density. The microfocus beamline U41-PGM (see figure 4.2), at which the experiment presented in this thesis were carried out, meets these requirements. [56] The undulator serving the beamline has a magnetic array of 80 periods and a period length λ of 41 mm. It is installed in a low beta section of the storage ring. Within the beamline the linear polarized synchrotron radiation passes first through a monochromatization stage. A gold-coated toroidal mirror images the source onto

the exit slit in the horizontal plane and collimates the light vertically. Monochromatization of the light is achieved by a combination of a plain grating (600 $\frac{1}{mm}$) and a plain mirror which allow, upon varying the fix-focus constant c_{ff}, to obtain either a high photon flux or a high energy resolution, according to the experimental requirements. Photon energies ranging from 170 eV up to 1800 eV can be provided. At 540 eV a maximum energy resolution of approximately 180 meV is obtained with a 20 μm slit. A cylindrical mirror focuses the monochromatic collimated beam vertically onto the exit slit. The size of the exit slit can be varied between 20, 40, 100, 200, 500, 2000 and 3000 μm. Since the resolution increases with decreasing slit-size, all X-ray absorption measurements presented in this work were carried out with a 20 μm slit, whereas for the X-ray emission measurements, which require a high incoming flux, a 40 μm or a 100 μm slit was used. The monochromatization stage is followed by a refocusing stage, in which a toroidal mirror refocuses the synchrotron radiation. By this a spot size of 23 μm (hor.) x 12 μm (ver.) with a flux of 10^{13} can be achieved (ring current: 100 mA; cff value: 0.65; slit: 100 μm) at the experiment. Upon measuring the current I_0 caused by the photoelectrons ejected upon synchrotron irradiation from the refocusing mirror, variations in the incoming flux can be segregated from the measured data of the experiment.

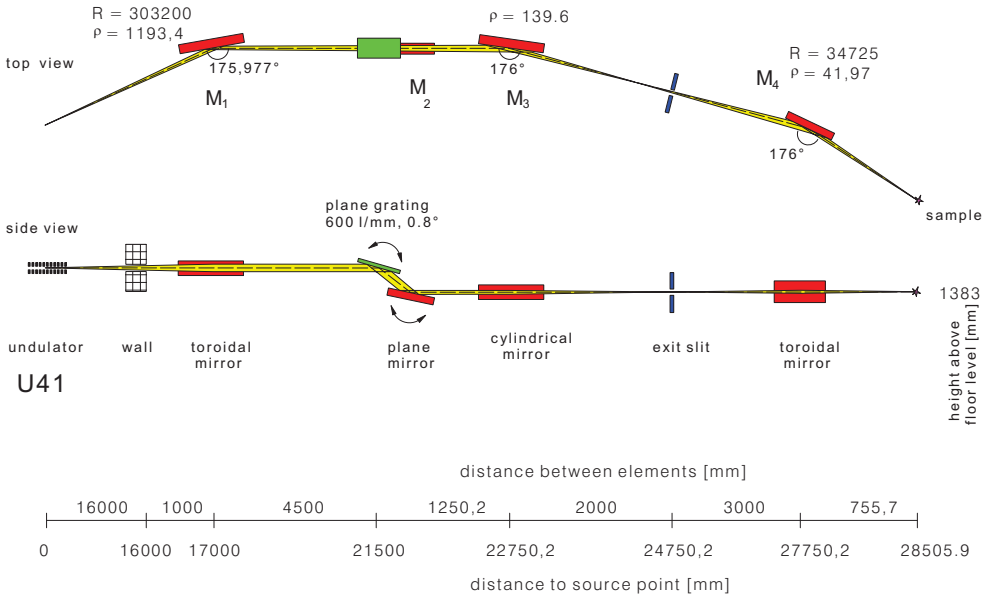

Figure 4.2.: Schematic of the U41-PGM beamline at the BESSY II synchrotron facility [57]

4.3. Experimental Setups

For the synchrotron based measurements presented in this work one well established experimental endstation was used, and one endstation was newly developed and built. Both setups are presented in this section. The XA spectra of the shared solvation of ions and the correlated irradiation induced effects (see section 6.5) were measured using the Liquidrom setup. The XA and XE hydrogen bond studies of water and aqueous ions (see sections 6.1, 6.3 and 6.4) were carried out on the newly developed LiXEdrom setup. This novel setup, which is the first of its kind at a synchrotron facility, was built in the framework of this thesis and a detailed description is presented here. The FT-IR spectrometer used for the measurements of water in different organic solvents (see section 6.2) is presented in the end of this chapter.

4.3.1. Liquidrom

The Liquidrom is an experimental endstation designed for XAS measurements of liquid samples by various techniques. The setup was used for the XA measurements of sodium ions in water, different alcohols, and their mixtures (see section 6.5).

In this setup the incoming synchrotron beam first passes through the two pinholes of a differential pumping chamber which separates the vacuum of the refocusing chamber (10^{-9} mbar) from the measuring chamber of the setup (10^{-5} mbar). Inside the main chamber the liquid sample is contained in a flow-cell (see figure 4.3a)). A Si_3N_4 membrane of 150 nm thickness, which is almost transparent for the incoming X-rays separates the liquid from the vacuum. Note, however, that no membrane is ideally transparent. For low concentrated samples the reduction of intensity by

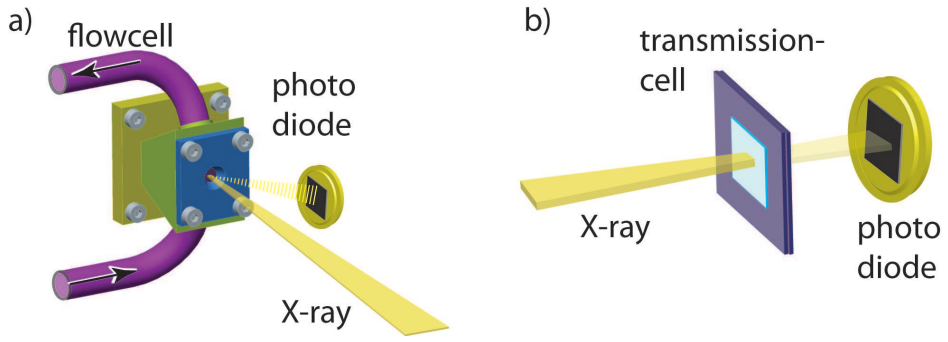

Figure 4.3.: Schematic of the flow-cell and the transmission cell that can be used in the Liquidrom setup for soft X-ray spectroscopy on liquids

the membrane can be crucial. Furthermore, the edges of the elements contained in the membrane material (Si and N) cannot be investigated. To avoid X-ray induced damage fresh sample can be continuously introduced to the flow-cell via an external pump. In order to investigate irradiation induced effects as in section 6.5 a closed sample loop configuration can be chosen or the flow is simply stopped. The total fluorescence yield is recorded using a GaAsP diode. The quantum yield function of such diodes covers an energy range from visible light (a few eVs) up to hard X-rays (> 2 keV), allowing the detection of a large number of parallel radiative decay channels. The diode is positioned in an angle of 45° with respect to incoming synchrotron radiation. Alternatively spectra can be also recorded in transmission mode, where a drop of the sample is contained between two Si_3N_4 membranes and the transmitted light is recorded by a diode positioned behind, as shown in figure 4.3b). Since the sample cannot be refreshed in this configuration, the risk of sample damage has to be evaluated and the necessary/possible precautions have to be taken. Such precautions can be the reduction of the incoming flux and shorter measuring times.

4.3.2. LiXEdrom

The novel LiXEdrom spectrometer is the first setup which allows obtaining XA as well as high resolution XE spectra from a liquid micro-jet in the soft X-ray regime in a membrane-free configuration. Its development and its setting into operation was one of the main challenges of this thesis. Here, first the setup and the mode of operation are presented, followed by a detailed discussion of particular components and aspects.

In figure 4.4 a schematic drawing of the LiXEdrom is presented. The samples are introduced via a liquid-micro-jet. XA spectra can be recorded in TFY mode using a GaAsP diode. The XE spectrometer is based on Rowland circle geometry (see figure 4.5). This geometry allows achieving wavelength dispersion and focusing by using only one optical element, e.g., a spherical grating. It requires that source point, grating, and detector are located along the Rowland circle, whose diameter is defined by the radius of the grating. In the LiXEdrom spectrometer, one of four different gratings can be selected, whereas each one has a different radius and line density optimized for a specific energy region. Accordingly, the size of the respective Rowland circle varies with the grating. The four gratings are mounted on a rotable holder. In order to avoid stray light, the incoming emission light can be narrowed down to the dimensions of the grating surface by using baffles. All four gratings together cover an energy range from 20 eV up to 1000 eV. By this, life elements like carbon, nitrogen, and oxygen can be probed through the K-edges. Also the L-edges of 3d-

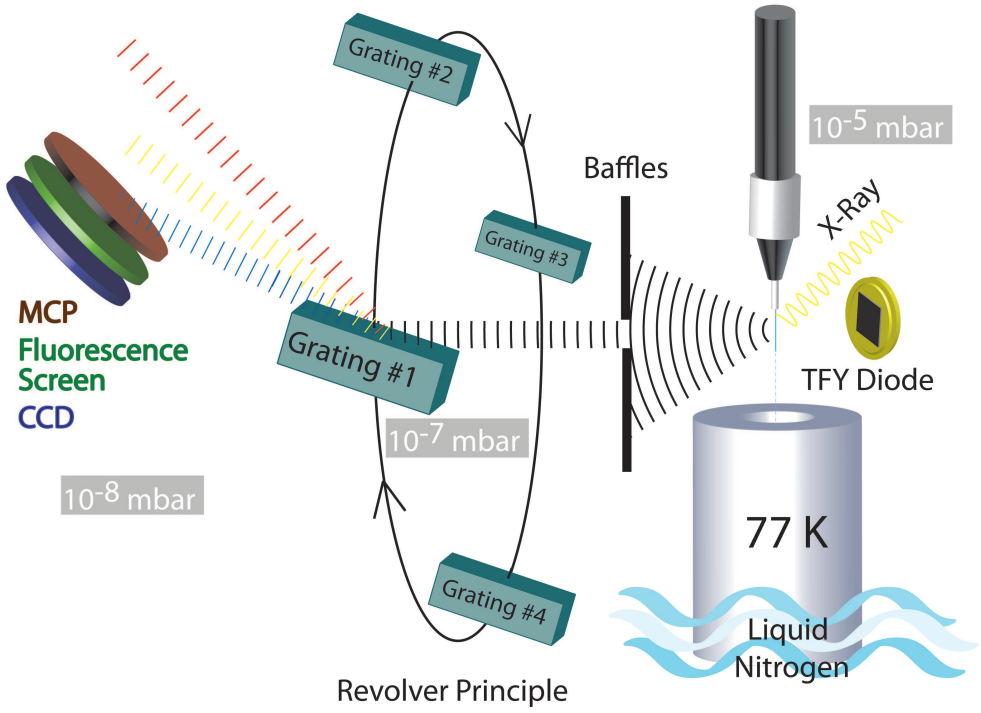

Figure 4.4.: Schematic drawing of the LiXEdrom setup. [66] The liquid sample is delivered via a micro-jet and trapped inside a container cooled down by liquid nitrogen. The emitted light is collected via total fluorescence yield (TFY) XAS or with the help of blazed gratings energy dispersed (XES).

transition metals like manganese, iron, and cobalt can be investigated, as well as the edges of many different lanthanides and actinides. The detection unit of the setup consists of two multi-channel plates, a phosphor screen, and a CCD camera, allowing to record two-dimensional data matrices of the incoming emission light. The procedure of converting these data matrices to emission spectra is presented in section 5.2. The high voltage applied to the detection unit requires a vacuum of around 10^{-8} mbar to 10^{-7} mbar in the detection chamber. Also in the beamlines of the synchrotron, to which the setup is connected, a vacuum of 10^{-9} mbar to 10^{-8} mbar prevails. How to ensure these high vacuum conditions despite a free flowing liquid micro-jet in a membrane free configuration is one of the topics explained in the following sections. Moreover, detailed descriptions of the individual components of the LiXEdrom spectrometer are presented.

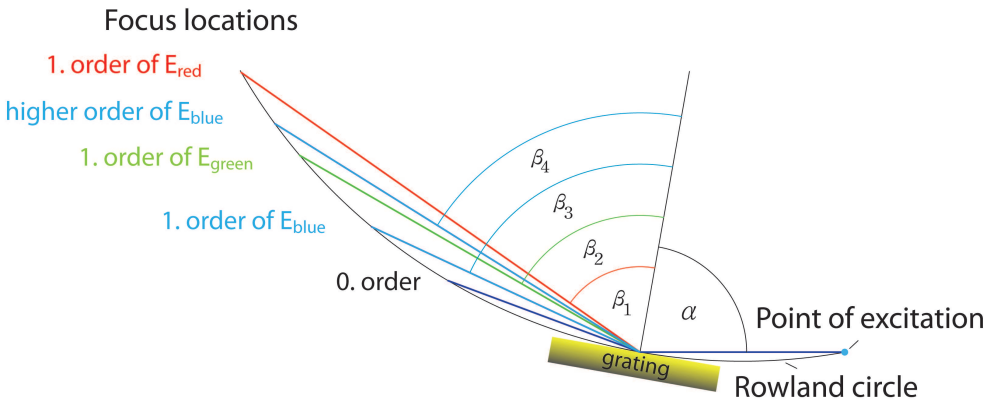

Figure 4.5.: Schematic of the Rowland circle principle. The light coming from a point of excitation is energetically dispersed and refocused via a curved grating. When the point of excitation and the grating lie on a circle with half the radius of the grating curvature, also the focus locations of the refocused light are found on this circle.

The Gratings

In the Rowland circle based spectrometer the gratings are the optical elements that are used for the energy dependent dispersion of the X-rays as well as the refocusing. In the soft X-ray regime conventional optics cannot be applied due to the strong absorbance by matter. Since the wavelengths of soft X-rays are too long to use natural crystals for Bragg reflection, artificial gratings created, e.g., by holographic or mechanic techniques have to be used.
To obtain a significant reflectivity, the gratings are used in total internal reflection geometry. This is possible since for soft X-rays the vacuum has a higher refractive index than the material of the grating. In table 4.1 the four different incidence angles used in the LiXEdrom spectrometer are listed with respect to the grating normal.
The grating equation 4.1 describes the relation between the incoming wavelength λ, the incidence angle α, and the angle of the diffracted light β for a grating with the grating constant d. Note that n is an integer.

$$d \cdot (sin\alpha - sin\beta) = n \cdot \lambda \tag{4.1}$$

According to this equation the line density of the grating has to be increased to keep a comparable resolution for increasing energies. In table 4.1 the line densities of the gratings used in the presented spectrometer are presented. Furthermore, the grating equation shows that the light for one specific energy is not only dispersed to one angle, but that also higher orders are possible, as indicated by the n in the formula. By us-

Grating	Radius [m]	Line density [mm^{-1}]	Incidence angle α [deg.]	Energy range [eV]
1	2	400	83.50	20-50
2	3.71	600	86.66	50-175
3	5	1200	87.52	175-400
4	7.5	1200	88.35	400-1000

Table 4.1.: Grating parameters of the LiXEdrom setup [22]

ing blazed gratings the intensity distribution between the different orders can be optimized for a specific energy range. Unlike a normal grating the groove surface of a blazed grating is not parallel to the grating surface. Instead, the grooves are saw tooth shaped with one long and one short flank. The angle of this tooth shape with respect to the grating normal leads to an additional path difference depending on where the incoming light hits the groove surface. The intensity distribution of the dispersed light has the maximum intensity for a blazed grating when the incoming angle of the light on the tilted groove surface is equal the emergent angle. In the LiXEdrom spectrometer blazed gratings are used for which the blaze angle is optimized for the energy range shown in table 4.1.
Besides the energy dispersion, the gratings should refocus the X-rays on the Rowland circle. Therefore spherical gratings are used. For increasing photon energy an increasing grating radius is used to achieve comparable resolution (see table 4.1). According to the grating radius the diameter of the Rowland circle varies as well.
In the LiXEdrom setup the four gratings are mounted on a rotable grating holder, which allows exchanging gratings according to the revolver principle. The axis of the irradiating emission light is fixed and the angle of every grating was adjusted at ambient conditions using a theodolite. The adjustment proved to be stable, enduring also a transport of the setup.

The Detection Unit

A two-dimensional area detector assembly from VG Scienta was used for recording the spectra. Figure 4.6 shows a schematic drawing of this detector. The core of the unit consists of two multi-channel plates (MCP). High negative voltage (-1.67 kV) is applied on the upper MCP, whereas the bottom one is grounded. In order to enhance the efficiency for the photo-electron production, the upper MCP is coated with CsI. Striking emission photons kick out electrons which are multiplied down the MCP by the applied high voltage. An additionally negatively charged deflection plate (-1.76 kV) positioned above the MCPs reassures, that the free

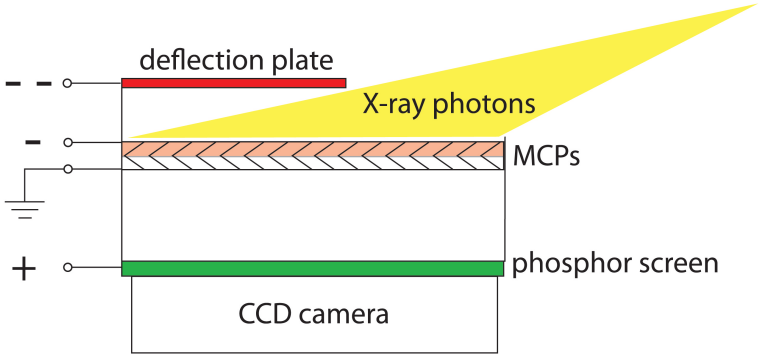

Figure 4.6.: Schematic of the XE detection unit

electrons are accelerated downwards. The electrons are attracted by the positively charged phosphor screen. Upon hitting the phosphor screen, the electrons cause light flashes. The picture of the phosphor screen is recorded from underneath by a Basler Scout 17FM CCD camera. The resolution of this camera is 1392 x 1040 pixels and the maximum frame rate is 17 frames per second. Examples for recorded camera pictures and the resulting energy resolved spectra are presented in section 5.2.

The Liquid Micro-Jet

Soft X-ray based experiments require vacuum conditions which make the investigation of liquids challenging. Faubel and coworkers presented in 1988 a novel method to maintain a liquid surface in high vacuum. [37] In a following study they proved the efficiency of their micro-jet technique

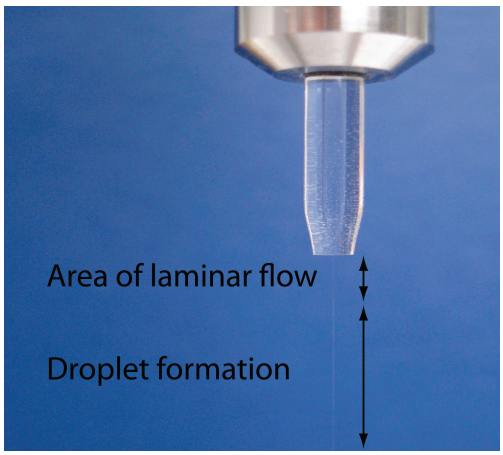

Figure 4.7.: Photo of a liquid micro-jet. After a region of laminar flow (≈ 3-5 mm) the jet decays into a stream of droplets.

by combining it with photoelectron spectroscopy, which requires high vacuum conditions, due to the short mean free path of electrons in a gas. [39]
The photo in figure 4.7 shows an enlargement of a liquid micro-jet. The liquid, in this case water, is pumped through a glass nozzle, which has an exit port of 5-25 μm. A cylindrical water jet with a very smooth surface and a length of 3-5 mm is created. The length of this laminar area varies with the flow-speed and with the pressure build up in the nozzle. A fast flow velocity and the small diameter prevent the laminar area from freezing due to rapid evaporative cooling in the vacuum environment. After several millimeters the jet decays into a stream of droplets.

The flow velocity v_{flow} can be determined geometrically from:

$$v_{flow} = F/(\pi r_0^2) \tag{4.2}$$

where F is the flow rate and r_0 the radius of the micro-jet. For an 18 μm jet diameter and a flow rate of 0.5 ml/min, as used in the experiment in section 6.1 this leads to a velocity of approximately 33 m/s.
The temperature of a sample can have influence on its properties. For the emission spectra of liquid water, e.g., temperature dependent variations have been observed. [43] Therefore it is important to estimate, which temperature the measured sample has. In the vacuum the temperature of a liquid-jet decreases along the jet-axis due to evaporative cooling. This position dependent behavior is described by the following expression: [38, 124]

$$\frac{dT_0}{dz} = -2\frac{\dot{r}_0(T_0)}{v_{jet}}\frac{\Lambda}{C_p}r_0^{-1} \tag{4.3}$$

where T_0 is the temperature of the liquid at the axial jet position z [cm]. v_{jet} [cm/s] is the jet velocity, Λ [J/mol] the enthalpy of vaporization, C_p [J/mol K] the specific heat and $\dot{r}(T_o)$ [cm/s] the radial evaporative ablation rate. This latter rate describes how much the radius of the micro-jet decreases due to evaporation. It depends on the vapor pressure and accordingly on the temperature of the jet. It can be described as follows:

$$\dot{r}(T_0) = \bar{v}(T_0)\frac{\rho_{vapor}(T_0)}{\rho_{liquid}} \tag{4.4}$$

where $\bar{v}$ is the mean velocity of the evaporating molecules, which is for a

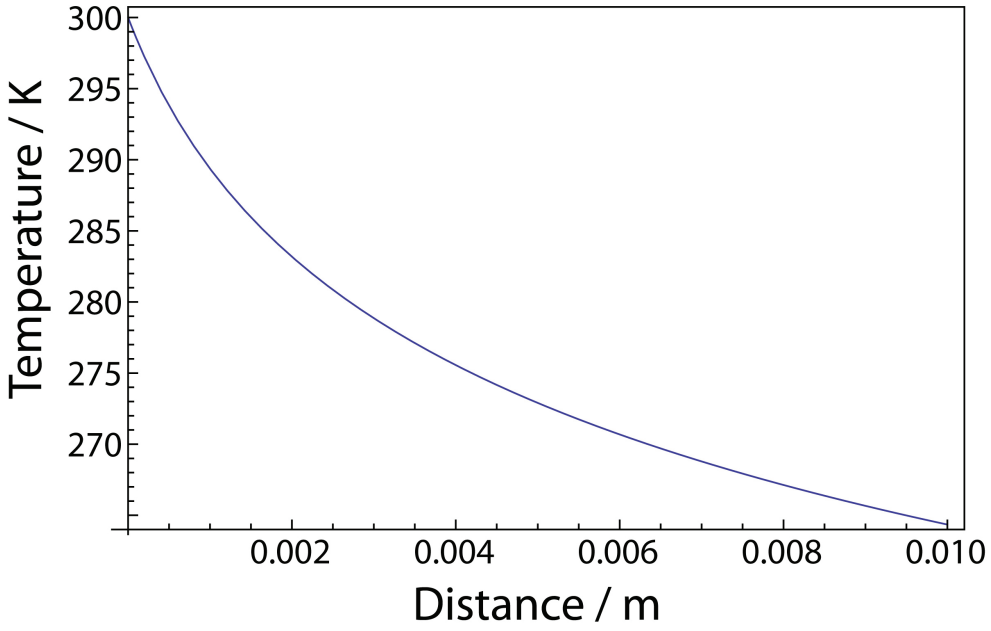

Figure 4.8.: Calculated temperature profile of a 20 μm liquid micro-jet along the jet axis. The distance refers to the nozzle opening.

Maxwellian distribution:

$$\bar{v} = \sqrt{\frac{8kT}{\pi m}} \tag{4.5}$$

Upon describing the vapor density ρ_v according to the Clausius Clapeyron formula and introducing a reference temperature T_{ref} the expression can be reduced to:

$$\dot{r}(T_0) = \dot{r}_{ref}\sqrt{\frac{T_0}{T_{ref}}}exp(-\frac{\Lambda}{kT_{ref}}(\frac{T_{ref}-T_0}{T_0})) \tag{4.6}$$

Equation 4.3 can be solved numerically. By fitting experimentally obtained temperature curves based on Raman spectroscopy, it was shown that for jet diameter larger than 10 μm an ablation rate of ≈ 0.055 cm/s is an appropriate value. [124] In figure 4.8 a calculated temperature profile based on the above equations for a nozzle of 20 μm and a flow of around 0.4 ml/min is presented. More details about the temperature and thermodynamics of a liquid jet in vacuum can be found in references [124] and [38].

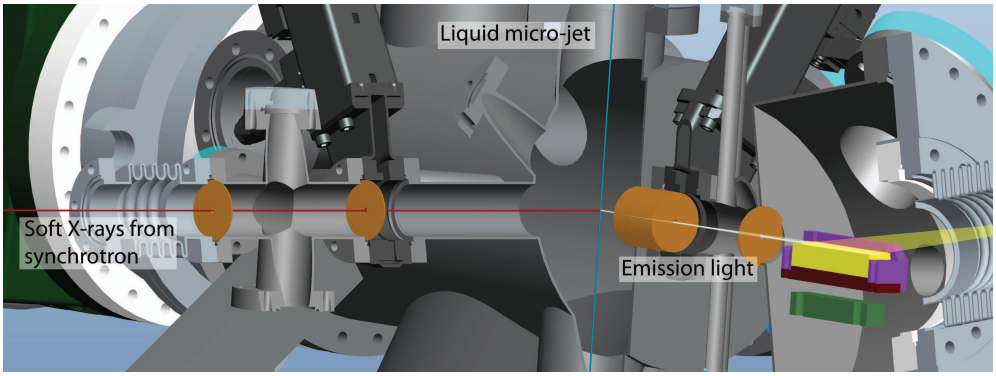

Figure 4.9.: Differential pumping arrangement in the LiXEdrom setup. The differential pumping stage on the left side separates the pressure of the main chamber from the beamline, whereas the one on the right side assures the high vacuum conditions for grating chamber and detector.

Bridging the Pressure Gap between Liquid and Vacuum

The measurements with soft X-rays require high vacuum conditions due to the large absorption cross section of air in this energy range. In the refocusing chamber of the beamline, to which the experimental endstations are connected, a pressure of 10^{-9} mbar should prevail. Also, in the chamber of the MCP-CCD detector used for the XE spectra, a pressure of 10^{-7} mbar should not be exceeded. Regarding the fact, that the LiXEdrom is a membrane free spectrometer in which fresh sample is constantly delivered via a free liquid micro-jet, several precautions have to be made in order to maintain stable vacuum conditions.
In large parts the liquid from the micro-jet is detained from evaporating by freezing. Underneath the micro-jet a steel container is connected, which is cooled from outside by liquid nitrogen. The frozen sample deposits on the inner walls of this container. The container has to be cleaned out after around 8 hours of operating time, depending on the physical properties of the sample, the nozzle diameter and the flowrate.
The pump performance of 1250 l/s of the turbopump connected to the liquid jet chamber is not sufficient to obtain the required vacuum conditions. The use of additional cryotraps allows obtaining a pressure of 10^{-6} mbar to 10^{-5} mbar in the jet chamber. Steel containers filled with liquid nitrogen were used as cryotraps. On their cold outer surface vapor molecules condense. In the LiXEdrom setup there are cryotrap surfaces of around 1700 cm^2. Figure 4.9 shows an insight into the main chamber of the LiXEdrom, to which the liquid micro-jet is introduced. The differential pumping stage towards the beamline is on the left of the jet-chamber. Two pinholes of 1 mm and 4 mm diameter combined with a CF 63 turbopump and an additional cryotrap separate the vacuum of the

beamline from the main chamber. Towards the grating and the detector chamber on the right in figure 4.9 an extended pinhole of 5 mm diameter and 50 mm length and a second pinhole of 8 mm diameter and 20 mm length comprise a volume pumped by a CF 35 turbopump. These two differential pumping stages allow obtaining the required vacuum conditions towards beamline and detector.

4.4. The Fourier-Transform Infrared Spectrometer

Usually the recording of a spectrum requires monochromatizing the probing or the emitted/transmitted light, as presented before for the monochromatized synchrotron light and the emission spectrometer. Also for the infrared (IR) spectroscopy such dispersive spectrometers were initially used. In the 1970s these spectrometers were widely replaced by Fourier-Transform Infrared (FT-IR) spectrometers [16], which allow measuring all frequencies over a wide spectral range at the same time. The centerpiece of an FT-IR spectrometer is an interferometer, as invented by Michelson in the 1880. A schematic drawing of a Michelson-interferometer is presented in figure 4.10. From a point source S broadband infrared light is emitted. The beamsplitter BS reflects one half of this light and transmits the other half. The reflected light is after a distance L reflected back to the beamsplitter by the mirror M_1, so that the reflected light covered a distance of 2L. The transmitted beam is reflected back by the mirror M_2, which is mounted on a movable stage. This stage allows to vary the optical path difference δ between the reflected and the transmitted light, when they merge again at the beamsplitter. From there the light propagates through the sample before its interference pattern is recorded by the detector. The intensity recorded as a function of δ is called interferogram. At zero path difference, ideally, the light of all wavenumbers interferes constructively and the maximum intensity is recorded at the detector. By Fourier transforming the interferogram I(δ) one would ideally obtain the absorption spectrum S in dependence of the wavenumber ν:

$$S(\omega) = \int_{-\infty}^{\infty} I(\delta) cos(2\pi\nu\delta) d\delta = 2 \int_{0}^{\infty} I(\delta) cos(2\pi\nu\delta) d\delta \qquad (4.7)$$

Since in practice the interferograms cannot be recorded for infinite δ-values, the a discrete Fourier transform of the digitalized detector signal is used as an approximation for the continuous Fourier series.
There are several advantages of an FT-IR spectrometer with respect to dispersive or grating spectrometers. Instead of slits, as for dispersive

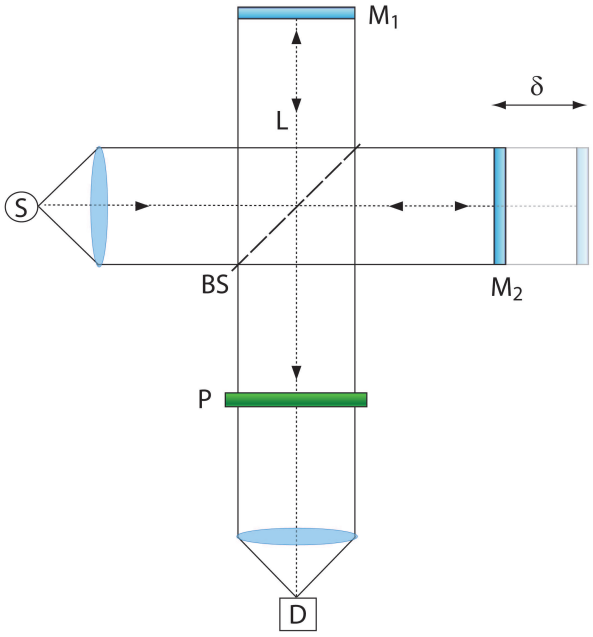

Figure 4.10.: Schematic of an ideal Michelson interferometer, which is the centerpiece of FT-IR spectrometers [15]

spectrometers, circular apertures can be used which enhance significantly the light throughput and accordingly the singal-to-noise ratio (Jacquinot advantage). For the FT-IR spectrometer a HeNe laser is used to determine the position of mirror M_2. This leads to a very high accuracy for determining δ and ν and no additional external frequency calibration is required (Connes advantage). Since it is possible to shine in and to detect all wave numbers at the same time, the measuring time is significantly reduced compared to dispersive spectrometers (Fellgett advantage). More details about FT-IR spectroscopy can be found in reference [15].
The FT-IR spectra in section 6.2 were recorded in transmission mode using a Vertex 80V FT-IR spectrometer with a liquid-nitrogen-cooled MCT detector and a KBr-beamsplitter. The samples were kept inside a liquid cell with 2 mm thick CaF_2-windows and PTFE spacers. The recorded vibrational modes showed a high sensitivity for temperature variations. Therefore, a liquid cell was used, where the temperature can be controlled.

5. Data Analysis and Theoretical Modeling

Before analyzing and interpreting the experimentally obtained spectra, a treating of the data, e.g., normalization or background correction, is necessary. The treatment of the XA and XE raw data of the spectra shown in this work is explained in sections 5.1 and 5.2. For the XA spectroscopy, effects that can disturb the direct proportionality between the TFY signal and the absorption cross section are discussed in section 5.1.2 and 5.1.3. The data analysis of the FT-IR spectra is explained in section 5.3.
In most of the studies in this thesis the data was interpreted based on a purely experimental approach, e.g., by combining several experimental methods or by systematically varying one parameter. For the aqueous Ni^{2+} ions (see section 6.1) the nature of the unoccupied molecular orbitals was revealed using Gaussian simulations. The Gaussian03 program is presented in section 5.4 of this chapter.

5.1. X-Ray Absorption Spectra

5.1.1. Normalization

It has been assumed that the fluorescence intensity of the XA spectra is directly proportional to the incident X-ray intensity. Therefore, the spectra have to be normalized when the incoming intensity is not constant. At the synchrotron the ring current decreases by time due to instabilities of the electron bunches in the storage ring. Accordingly, the resulting synchrotron radiation intensity decreases. The optics in the beamline cause further effects. Energy dependent reflectivity and contaminations of gratings and mirrors vary the X-ray intensity at the experiment. In order to compensate for these effects, the incoming X-ray signal is monitored parallel to the measurements. In the U41 PGM beamline it is possible to measure the photoelectron signal from the last mirror before the experimental station by reading out the mirror current I_0. The absorption spectra are normalized by dividing them by this in parallel recorded I_0

signal. For liquid spectroscopy of a solute, a spectrum of the pure solvent can be used additionally for normalizing the data. More details about this procedure can be found in reference [111].

5.1.2. Saturation Effect

The FY for thin layers as well as for dilute samples is considered to be in most cases directly proportional to the absorption coefficient. However, for concentrated bulk samples this correlation is not valid. [32, 35] The spectra suffer from distortions, called saturation effects, which lead to an overemphasizing of low intensity spectral features with respect to high intensity ones. This effect depends on the geometry of the experiment. [35] For grazing-incidence and normal-takeoff geometry (see figure 5.1a) maximal distortions are expected, since all photons are absorbed close to the surface of the sample. Due to the short way out of the sample, almost all fluorescence photons emitted in the direction of the detector can reach the detector. Accordingly, the energy dependent fluorescence signal loses its proportionality to the absorption cross section. In normal-incidence grazing-takeoff geometry (see figure 5.1b) also all photons will be absorbed, but the energy dependent absorption cross section varies the penetration depth of the photons. A large absorption cross section leads to a short penetration depth; the resulting fluorescence photon has a high chance to leave the sample without being absorbed on the way out. A small absorption cross section leads to a higher penetration depth, which increases the chance for the fluorescence photon to be absorbed on the way

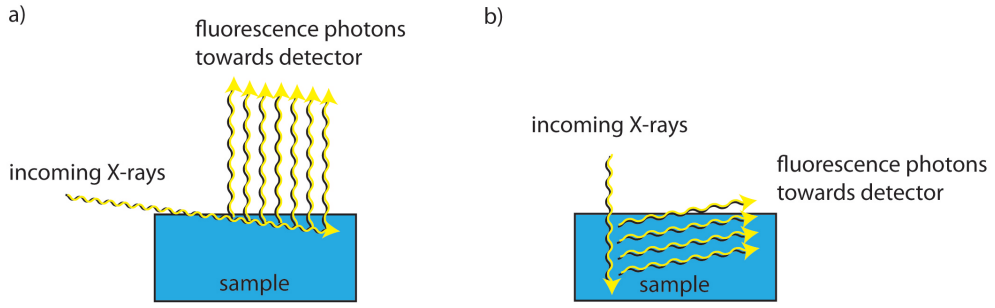

Figure 5.1.: a) Excitation by grazing incident light and detection of photons with a normal take-off angle with respect to the sample surface. For this geometry saturation effects can strongly contribute to the TFY spectra b) Excitation by photons with perpendicular incidence angle with respect to the sample surface. The fluorescence yield is detected in grazing take-off geometry. In this case the self-absorption of the fluorescence photons on the way out reduces saturation effects.

out. Accordingly, the self-absorption within the sample compensates the saturation effects. More details about this effect as well as an approach to calculate the saturation effect can be found in reference [35]. In this thesis examples for the saturation effect can be found in chapter 6 in the XA spectra of pure water. The reduction of the saturation upon diluting pure water as a bulk sample with acetonitrile is presented in section 6.3.

5.1.3. Background and Dark Channel Fluorescence Yield

At an absorption edge one usually expects a steep rise of the fluorescence signal of the investigated element. This is however not necessarily the case. Recently published FY spectra of transition metals in aqueous solution exhibit 'dips' instead of peaks at the transition metal L-edge (see figure 5.2). [9] For understanding this observation it has to be considered that for these systems the fluorescence signal before the transition metal absorption L-edge differs from zero. For iron ions in aqueous solutions the iron L-edges at around 715 eV load on a strong background created mainly by the oxygen K-edge of the water, which lies at around 535 eV (see figure 5.3). Upon scanning across the iron L-edge, absorption and fluorescence by the iron ions set in. By this, however, the number of photons available

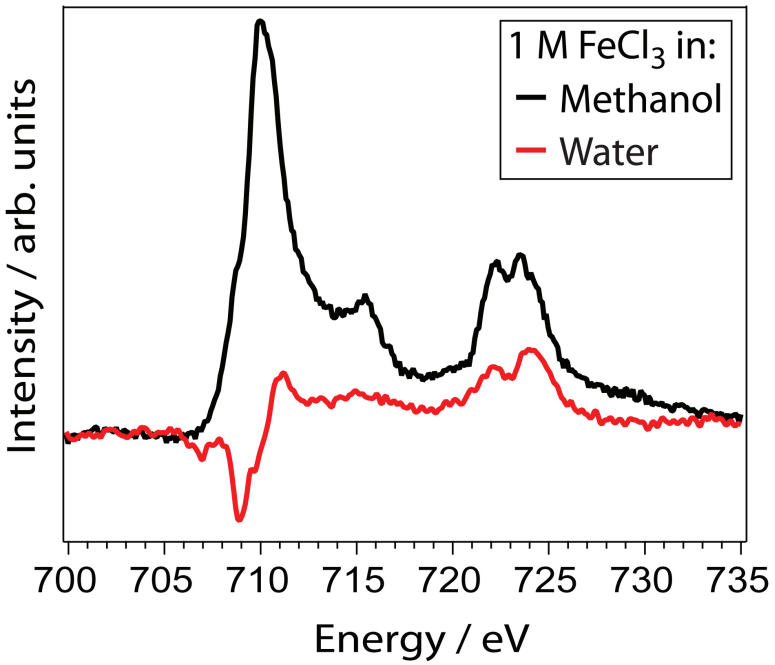

Figure 5.2.: L-edge TFY-XA spectra of $FeCl_3$ in water and methanol. The spectrum in water shows 'dips', where the fluorescence signal drops under the background intensity. [9]

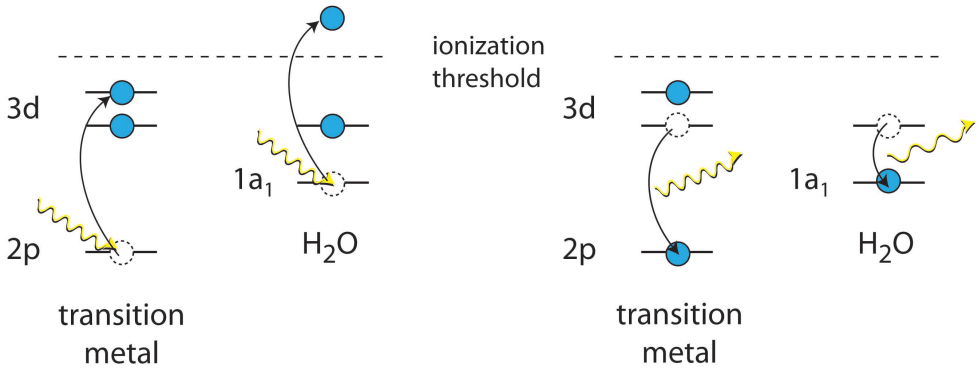

Figure 5.3.: Upon exciting the L-edge of a transition metal aqueous solution (e.g. of iron at around 715 eV), the K-edge of the oxygen of the water is excited simultaneously. The fluorescence of the oxygen contributes to the background signal of the iron L-edge TFY-XA spectra.

for exciting the oxygen of the water is reduced. Accordingly, there is a competition between the fluorescence of the solute and the solvent.
Based on solvent, solute, and coordination dependent measurements it was furthermore proposed that besides the above described competition a competition between radiative and non-radiative channels is taking place for the transition metals. [9] A charge transfer from the transition metal to the solvent could lead to a reduction of the radiative decay channels. This proposed mechanism was named dark-channel fluorescence yield (DCFY). From the observation that the L_3-edge features are affected more than the L_2-edge features by the reduction of fluorescence intensity, the time scale of the DCFY was estimated. The core-hole lifetime of the L_2 edge (≈ 0.7 fs) is shorter than that of the L_3 edge (≈ 2 fs), [95] so that the L_2 would be less affected by such an electron transfer because of its higher radiative decay rate. This would also set an upper limit for an induced electron transfer from the transition metal to the ligand. [9] However, TFY or TEY studies cannot provide direct and quantitative information on the electronic relaxation pathways of the 2p-core excited transition metal ion in solution. By using photoelectron spectroscopy it was shown that the metal t_{2g} levels overlap energetically well with the valence band of water, [107] enabling strong orbital mixing, in agreement with previous density-functional theory calculations. [83] Such orbital overlap could affect the relaxation behaviour, as proposed in the DCFY. Further studies based on partial and inverse partial fluorescence yield measurements are currently running in our group. The deviations between the absoption spectra of aqueous Ni^{2+} ions obtained via electron and photon yield are presented in section 6.1. Based on additional XE spectra, the influence of possible charge transfer processes is discussed there briefly.

5.2. X-Ray Emission Spectra

In the XE spectrometer the energy dispersed light hits the surface of the multi-channel plates, from where it removes electrons, which are multiplied and accelerated onto a luminescence screen. Pictures of this screen are recorded by a CCD camera. How this 2-dimensional picture is treated and converted into a spectrum is explained in the following sections.

5.2.1. Curve Correction

As an example a picture recorded by the CCD camera is presented in figure 5.4 a) for liquid D_2O. It can be read out as a matrix containing the entries of 1400 x 1040 channels. The spectrum, shown in figure 5.4 b), is obtained by summing up the entries of the 1040 channels.

As recognizable in figure 5.4a, the lines, which belong ideally to one

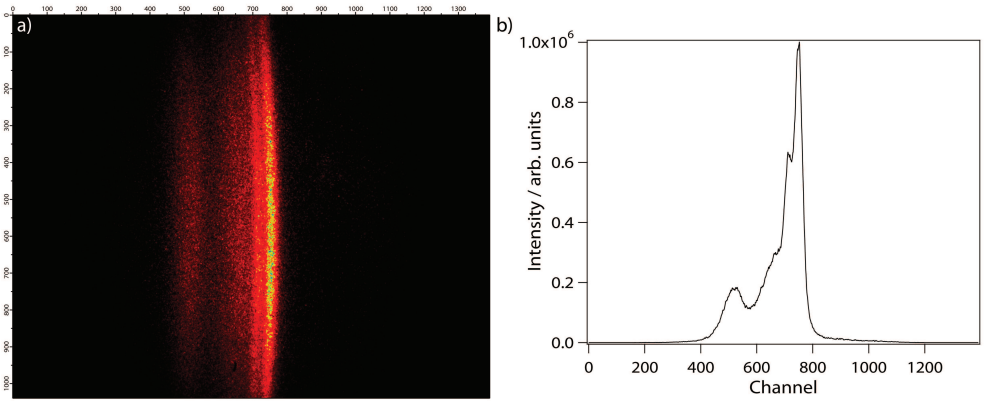

Figure 5.4.: a) Picture recorded with the CCD camera of the XE detector. A curvature is observable in the presented O K-edge emission lines of D_2O. b) Spectrum derived from the data matrix of the picture shown in a). The curvature leads to a smearing of the resolution

energy, are curved. The origin of this curvature can be understood as follows: The emission light originates ideally from a point source, it is divergent. Therefore not all photons cross the grating on a course perpendicular to the grooves. The light dispersed on the outer edges of the grating sees a larger distance between the grooves which means a larger grating constant d. From the grating equation 4.1 it can be easily seen that for a larger d, a larger λ is required, when the angle is fixed. Accordingly, the light hitting the detector on the outer edges will be curved towards lower energies.
Since the channels of every vertical row in picture 5.4a are summed up to obtain the spectrum, the curvature of the lines leads to a smearing of

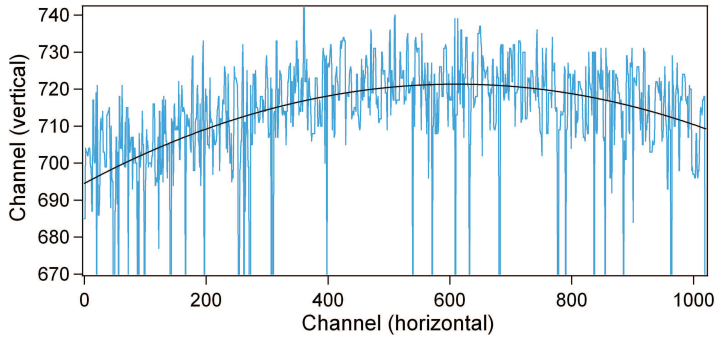

Figure 5.5.: Position of the maximum matrix entry plotted against the channel number. The integer values of the fitted curve are used for the curve correction

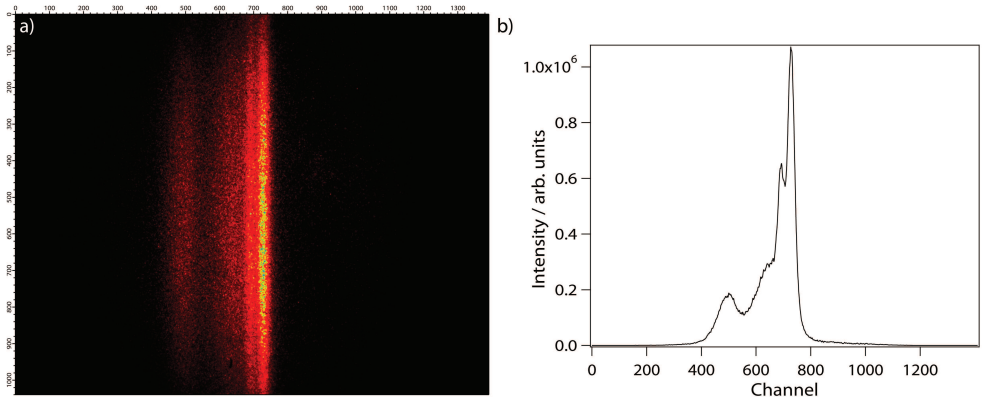

Figure 5.6.: a) Data matrix after the curve correction showing now straight emission lines. b) The spectrum derived from the curve corrected data matrix shows a higher resolution compared to the spectrum derived from the original data matrix.

the resolution. Therefore a curve correction is applied before deriving the spectra from the matrix.
The first step for the curve correction is to determine the curve progression. For this purpose the position of the maximum matrix entry in every of the 1040 channels is determined. The position of the maximum entry is then plotted against the channel number. Into this graph a polynomial with 1040 points is fitted, as shown in figure 5.5. The integer values of the fitted curve are used for the curve correction. After subtracting an offset (in this case of 694, as can be seen in figure 5.5) these integer values indicate how much the matrix entries have to be shifted to obtain a line instead of a curve. In figure 5.6a the data matrix is shown after curve correction. Upon comparing the spectrum derived from the curve corrected matrix, shown in figure 5.6b, to the original one in figure 5.4b, an enhancement of the resolution is evident.

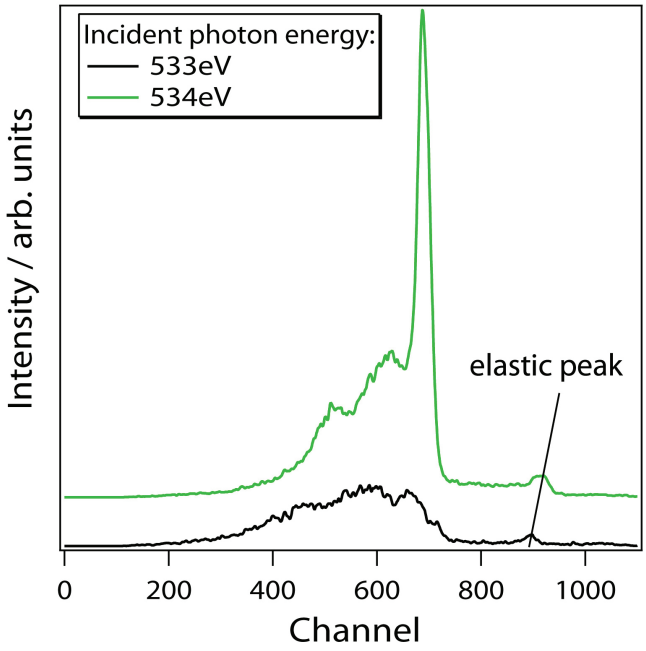

Figure 5.7.: The position of the elastic peak in the X-ray emission spectra can be used for the energy calibration.

5.2.2. Energy Calibration

As explained in the previous section, the spectrum obtained from the curve corrected data matrix is plotted against the channel number. In order to obtain instead an energy scale, an energy calibration is required. For the energy calibration the elastic peak in the spectrum or reference spectra from literature can be used. For the oxygen K-edge spectra presented in this thesis, the reference spectra were taken from reference [43] and [116]. Additionally the position of the elastic peak was used for verification (see 5.7).

5.3. FT-IR Spectra

In section 6.2, the FT-IR absorbance spectra of water mixtures with acetonitrile, benzene, and chloroform are presented. The region of interest for the water stretching vibrations ν_1 and ν_3 and the overtone bending vibration $2\nu_2$ lies between 4000 cm^{-1} and 3000 cm^{-1}. The main goal of these measurements was to monitor the changes of these bands upon varying hydrogen bond coordination, thus upon varying water concentration in acetonitrile. These bands overlap however strongly with the

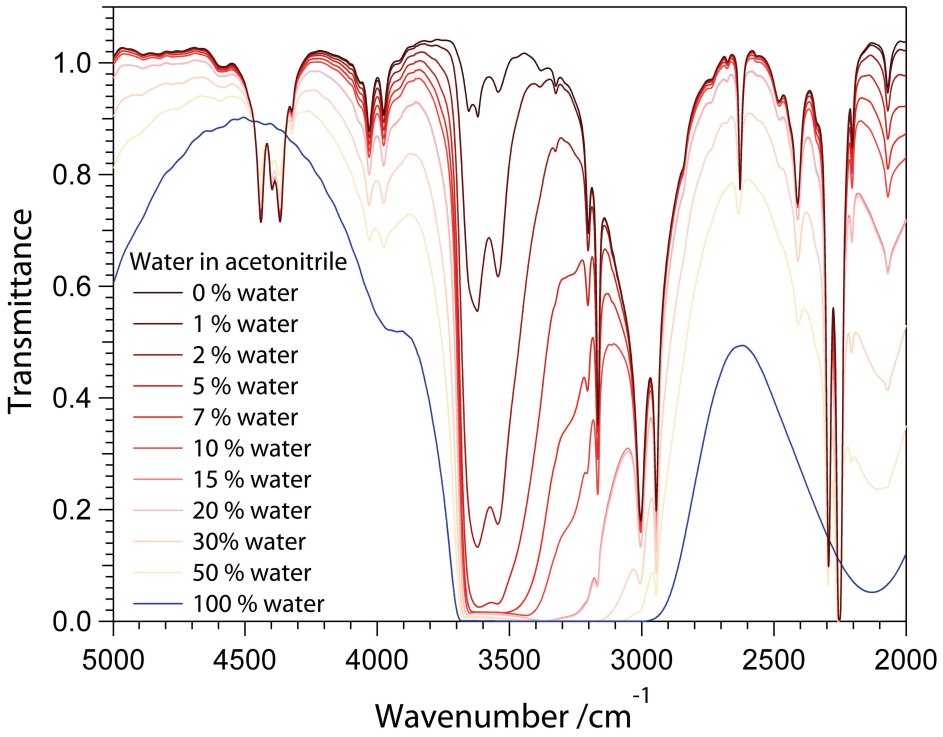

Figure 5.8.: Transmittance FT-IR spectra of water, acetonitrile and the respective mixtures.

absorption bands of the pure organic solvents. This is illustrated in figure 5.8, where the recorded spectra of pure water, acetonitrile, and the respective mixtures are shown. Note that these spectra are transmittance spectra. The transmittance T is defined as follows:

$$T = \frac{I}{I_0} \tag{5.1}$$

where I_0 is the intensity of the incoming light and I the intensity of the light transmitted through the sample. The first step of the data analysis is to transform these transmittance spectra to absorbance spectra. The absorbance of a sample is given by:

$$A = log_{10}\left(\frac{I_0}{I}\right) \tag{5.2}$$

After the transformation, the dominant absorption bands of the solvents have to be removed. For each measurement the absorbance spectrum of the pure solvent was subtracted from the measured spectra proportional to the respective water concentration. Accordingly, one refers to

Δ-absorbance spectra. The spectra shown in this work were normalized with respect to zero set at the position where the influence of the respective solvent was minor.

5.4. Theoretical Modelling: Gaussian

Gaussian03 is a computational chemistry program for modeling the electronic structure of systems. It allows predicting a wide range of molecular properties and reactions, including amongst others:

- Molecular energies and structures as well as energies and structures of transition states
- Molecular orbitals
- Atomic charges and electrostatic potentials
- Vibrational frequencies
- IR and Raman spectra

Predictions can be made for a wide variety of chemical environments. Also the simulation of solvation fields, as used for the calculations of aqueous Ni^{2+} ions (see section 6.1), is possible. In the following the used packages of the program are presented in detail.

Single Point Energy Calculation

The simplest type of calculation in the Gaussian program is the single point energy calculation. This approach allows predicting energy levels and related properties of a molecular system of specified geometry. The total energy of a system contains the electronic kinetic energy, the nuclear kinetic energy, the electron-nuclei interaction, the electron-electron interaction, and the nuclei-nuclei interaction. [26] The nuclear positions are fixed by the specified geometry. Accordingly, the nuclear kinetic energy is zero, whereas the electron-nuclei interaction is described by pseudopotentials. All the other energy and interaction terms mentioned above depend on the unknown charge density of the system. In the single point energy calculation the charge density has to be determined that minimizes the total energy of the system. The validity of the obtained results for the energy levels is strongly dependent on the availability of reasonable geometric input data. For optimized geometries, single point energy

calculations deliver highly accurate energy values. Furthermore, these calculations can be used for consistency checks on a molecular geometry used as a starting point for an optimization.

Geometry Optimization

Single point calculations require geometric input data. Variation of the geometry also varies the resulting energies and properties. Therefore a reasonable geometry of the molecular system of interest has to be determined. The geometry optimizations are based on the concept of potential energy surfaces. Each point on such a potential energy surface represents a specific molecular structure and the resulting energy of this system. For determining the equilibrium structures of a molecular system, the minima of the potential energy surface have to be found. Also the geometry optimization process requires geometric input data as a starting point. From this point the energy and the gradient of the potential energy surface are calculated to determine the direction of the next optimization step. When the convergence criteria and specific cutoff values are reached, the optimization process is complete.

Simulating Solvation Fields

The properties of molecules in gas phase can vary significantly from the ones in solution. A solvent with a high dielectric constant, for example, can reduce electrostatic effects significantly. The Gaussian program also allows considering solvent effects on molecular systems by different Self-Consistent Reaction Field (SCRF) models. In this approach the solvent is described by a uniform dielectric constant ϵ. Inside this reaction field a cavity with the solvent is placed. In the simplest SCRF model, the Onsager reaction field model, the cavity is defined as a sphere of radius a_0 within the solvent field. A dipole in the solute molecule induces a dipole in the medium. The electric field applied by the solvent dipole interacts in turn with the molecular dipole, leading to net stabilization. For the observation of solvation effects this model requires that the investigated system has a dipole moment. Otherwise the Onsager model calculations will give the same results as for the gas phase. More details about the Onsager model can be found in Ref. [96].
In the Tomasi's Polarized Continuum Model (PCM) the cavity is defined by overlapping and interlocking atomic spheres. Solvent polarization effects of the continuum are computed by numerical integration.
In the Isodensity PCM (IPCM) approach the cavity is defined as an isodensity surface of the molecule where the surface is determined by an

iterative process. In the Self-consistent Isodensity Polarized Continuum Model (SCI-PCM), additionally, the coupling between the isosurface and the electron density is considered which requires a folding of the solvation effects into the iterative SCF computation. More details about these models are discussed in literature (see references [79], [40] and [127]).

6. Experimental Studies

6.1. Proof of Principle for the LiXEdrom: Liquid Water and Aqueous Ni^{2+} ions

Lange et al., Chemical Physics 377, 1-3, pp 1-5 (2010)
http://www.sciencedirect.com/science/article/pii/S0301010410004052

6.1.1. Introduction

Spectroscopic techniques based on photon-in/photon-out processes using synchrotron radiation have proven to be highly sensitive tools for investigating the local electronic structure of condensed matter and of chemical and biological systems. Soft X-ray absorption [5, 6, 10, 47, 122] and emission spectroscopy [49,50,116,121] of liquid systems can probe the elements of life as e.g. C, O and N through the K-edges [8, 49, 121, 122] and transition metals through the L-edges [6, 7, 97]. Recently, the XAS technique was further extended for investigating in situ the preparation process of solar cells, [48, 70] as well as for probing the transition metal active centre of proteins and enzymes under physiological conditions. [7, 17, 97] In most of these recent XA studies on liquids, the samples were contained in a cell consisting of soft X-ray transparent thin (few hundreds of nm's) membrane windows made of silicon nitride (Si_3N_4). Flowing the liquid behind the membrane, as can be done with flow-cells, additionally reduces the risks of sample damage with respect to static drop-behind-membrane cells. However, in using a membrane several issues have to be considered:

- The membrane should be ideally transparent for the respective fluorescence light of interest. Therefore elements that are contained in the membrane material (Si and N) or are energetically close to them are not directly measurable.

- Since no membrane is ideally transparent for any energy range, measuring techniques which require a high incoming flux like, e.g. X-ray emission spectroscopy (XES), suffer from the loss of photons leading to long data acquisition times. [5] In the case of very low concentra-

tion samples, such as biochemical systems in physiological media, the loss of intensity is detrimental. [7, 17, 97]

- Interactions with the membrane, like hydrophobic or hydrophilic effects can induce artifacts in the spectra. As mentioned in the literature, the membrane can also react chemically upon X-ray radiation with the sample (e.g. oxidization of the inner surface of the Si_3N_4 membrane) and change its nature as a function of irradiation. [121] Such changes may affect the XA and XE spectra and cannot be neglected.

To overcome these issues, in this work fluorescence yield XAS and XES are combined for the first time with the micro-jet technique. This new approach is presented by investigations of the oxygen K-edge of liquid water and the Ni L-edge of a $NiCl_2$ aqueous solution under resonant and non-resonant excitation. The preliminary results are presented to demonstrate the capability of the new setup. A detailed discussion of the results, in particular for the case of aqueous Ni^{2+} ions will be given later. The series of XE spectra of water measured from the liquid-jet give qualitatively the same characteristics as what has been shown before for water behind an Si_3N_4 membrane and show a resolution comparable to the most recent publications on high resolution XES. [116, 121] For the aqueous $NiCl_2$, concentrations down to 250 mM were measured, but according to the signal to noise ratio, even lower ion concentrations can be measured with this setup. Moreover, the emission lines reflect what was recently proposed as the dark-channel- fluorescence-yield (DCFY) mechanism [9], which reveals electron delocalization in mixed orbitals between water and nickel. Since the DCFY is still under intense investigation by the F-N1 group, this issue will not be discussed in this thesis in details. For the interpretation of the emission spectra of aqueous $NiCl_2$, simple theoretical calculations using a Hartree-Fock (HF) approach combined with a self-consistent reaction field (SCRF) to include solvent effects were carried out.

6.1.2. Experimental Methods

The samples were measured with the LiXEdrom-setup at the U41 PGM beamline of BESSY II, which is in details described in section 6.1. For the measurements of the oxygen K-edge and the nickel L-edge a blazed grating of 7.5 m radius and 1200 lines mm^{-1} line density was used, optimized for the energy range of 400-1000 eV . The resolution reached with this configuration is comparable to recently published high resolution XES measurements of 350 meV at 530 eV for water behind a Si_3N_4

membrane. [116, 121] For the measurements of liquid water and $NiCl_2$ in aqueous solution a 23 μm and an 18 μm nozzle were used for the liquid-jet, respectively. The pressure inside the liquid-jet chamber during the measurements was in the range of 10^{-5}-10^{-6} mbar. Note, that the use of the liquid- jet technique allows measuring always a fresh sample, so that X-ray induced heating or sample damage is avoided. The electron yield (EY) spectra of aqueous $NiCl_2$ obtained from the liquid-jet were recorded as described before [22].

6.1.3. Theoretical Calculations

To reveal the nature of the molecular orbitals (MOs) of Ni^{2+} in water which are involved in the XE spectra ground state Hartree-Fock (HF) calculations were carried out using the Gaussian03 program package. [42] An often followed approach to include solvent effects into high level ab initio calculations are self-consistent reaction field (SCRF) methods. In these methods, the solvent is modeled as a continuum of uniform dielectric constant (called the reaction field) and the solute is placed into a cavity within the solvent. The different SCRF models differ in how they define the cavity and the reaction field. In this study the self-consistent isodensity polarized continuum model (SCI-PCM) was used, where the cavity around the Ni^{2+} ions is defined as an isodensity surface. The coupling between this isosurface and the electron density is considered by folding the solvation effects into the iterative SCF computation (see section 5.4).

6.1.4. Results and Discussion

In the following the results of the measurements obtained from liquid water will be discussed and compared to the recently published high resolution spectra of water. [116, 121] In the second section, the XE spectra obtained from Ni^{2+} resonant excitation around the L_3-edge of $NiCl_2$ aqueous solution will be presented. These results will be compared with previous results from drop-behind-membrane measurements at beamline 7, ALS-Berkeley lab [5] and verify the validity of the DCFY mechanism that was recently proposed. [9]

Pure Water

Using the example of liquid water in this section it is shown, that the newly developed liquid-jet XES spectrometer achieves a resolution com-

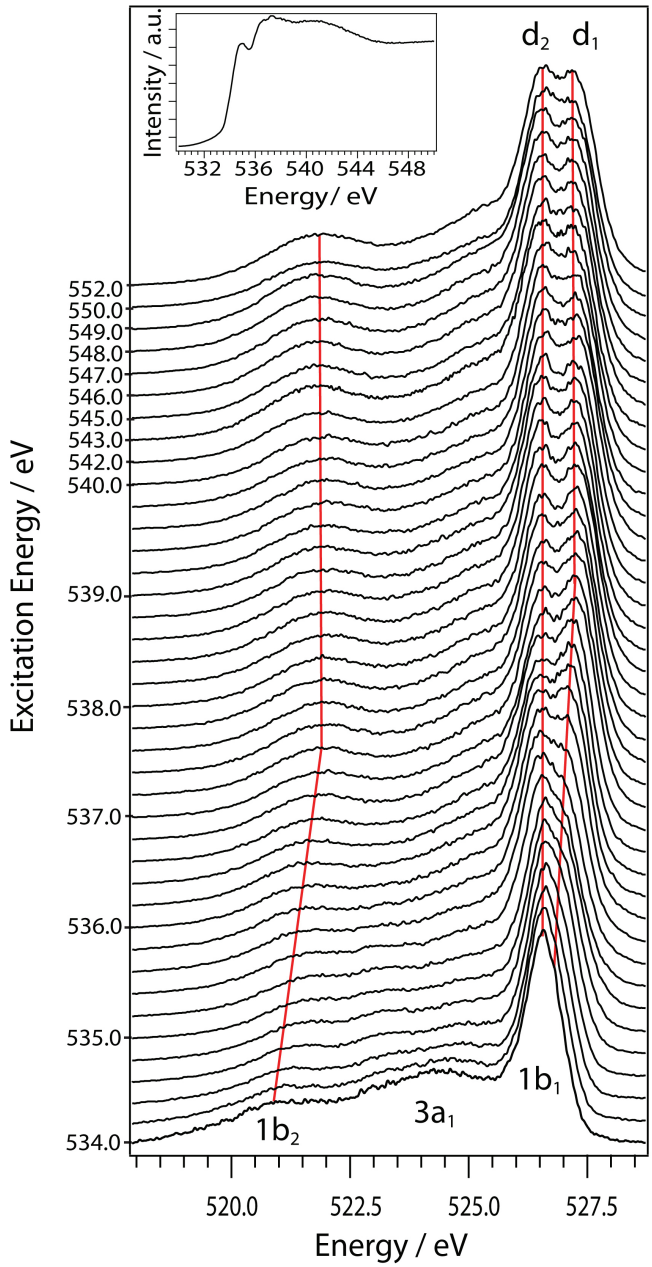

Figure 6.1.: O1s X-ray emission spectra of pure liquid water (15 °C) collected from the micro-jet at excitation energies from 534 eV up to 552 eV with 0.2 eV energy steps presented on the Y-axis; Inset: X-ray absorption spectrum of pure liquid water (15 °C) collected from the micro-jet with the main excitation energies marked. [66]

parable to the most recent published high resolution XES measurements carried out on membrane cells. [116, 121] In the top of figure 6.1 the XA spectrum of H_2O obtained with the micro-jet is presented, showing three characteristic spectral features: the pre-edge, the main-edge and the post-edge around 535, 537.5 and 540 eV, respectively. Note, that because of saturation effects the pre- and post-edge features are overemphasized with respect to the main-edge feature. The XES mapping, beginning with the resonant excitation of the pre-edge at 534 eV and proceeding upwards in 0.2 eV steps, is shown in the bottom part of figure 6.1. Whereas XAS probes the unoccupied density of electronic states, XES reveals information about the occupied electronic states, which for water are the $1b_2$, $3a_1$ and the $1b_1$ molecular orbitals (MO). The apparent broadening of the spectral features of the binding $1b_2$, $3a_1$ orbitals in comparison to non-bonding lone-pair $1b_1$ orbital is due to vibrational excitations. Upon increasing the excitation energy a splitting of the $1b_1$ spectral feature into the two peaks d_2 and d_1 sets in. [44] Whereas the former remains at its energetic position, the latter blue-shifts upon raising the excitation energy to 537 eV. For higher excitation energies the splitting of the two peaks stays constant. The origin of this splitting is much discussed in the literature. One interpretation correlates the two features to different hydrogen bonding states of the water molecule. [116] Another explanation proposes that ultrafast dissociation is causing the splitting, so that the d_2 can be correlated to dissociated OH species and the d_1 to intact water molecules. [44] Regarding the agreement of the experimental data obtained from the liquid-jet to the measurements of membrane cells, it can be concluded, that the latter results are not affected by long-range effects caused by the hydrophobic or hydrophilic interactions with the membrane. In the same way it can be concluded, that the measurements of liquid water on the liquid-jet are not suffering from a thermodynamic disequilibrium as was suspected by Weinhardt *et al.*. [121]

Aqueous Solution of Ni^{2+}

Recently a new mechanism for the electron transfer in aqueous metal-based atomic and molecular ions was proposed, focusing on the case of iron. [9] XA spectra obtained from aqueous transition metal L-edges by total fluorescence yield (TFY) measurements showed distortions compared to the respective non-aqueous transition metal solution spectra. Some of the TFY spectral components turned below the background of fluorescence light from the solvent, appearing as dips. The dips were attributed to an electron transfer from the X-ray excited state of the solute to the water molecules. The electron transfer occurs from states that delocal-

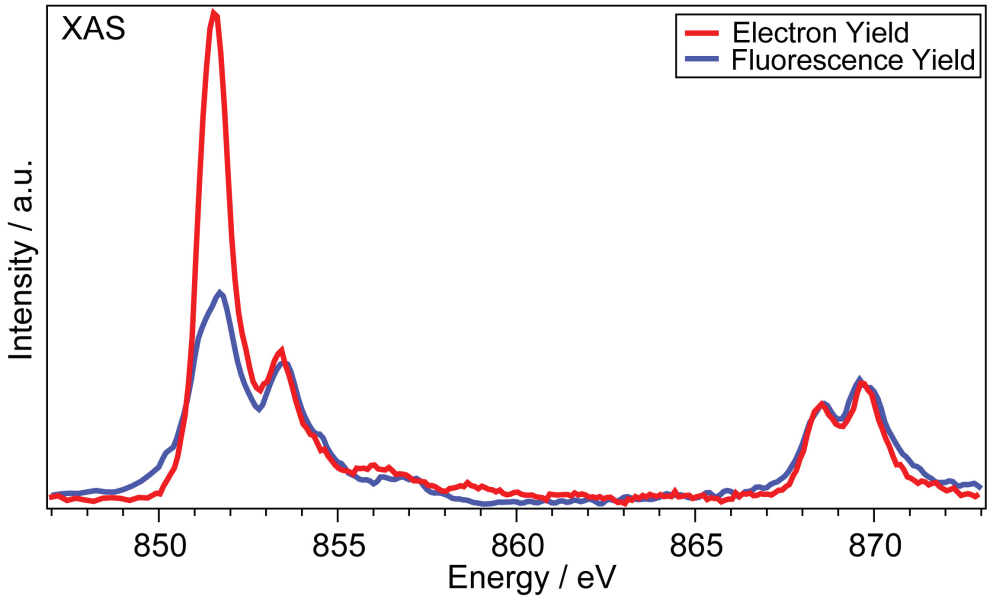

Figure 6.2.: Ni-2p X-ray absorption spectra of 1 M aqueous $NiCl_2$: comparison between total fluorescence yield and total electron yield [66]

ize in the electronic structure of the water continuum. The delocalized channel was called a 'dark channel' and the respective mechanism the 'dark-channel-fluorescence-yield' (DCFY). This observation was stressing the role of the water molecule, with respect to the other solvents, as it affects the electronic structure of the solute by forming a complex with its molecular orbitals. It was however stressed that any efficient electron transfer is correlated to a reduction of the fluorescence and that the DCFY is not necessarily depending on the water solvent. Examples where dips appear in the TFY spectra include metal-based molecular complexes undergoing intramolecular electron transfer. [9]

The excited intermolecular electron transfer from the metal to the water molecule reduces the X-ray fluorescence yield from the metal. However, the decay is largely (more than 99 %) dominated by Auger processes. Therefore, the comparison of FY and electron yield (EY) spectra of aqueous transition metals should also show directly the distortion caused by the DCFY. In this section is shown that L-edge XA spectrum of the aqueous solution of Ni^{2+} obtained from FY-technique differs from the one based on the EY-technique at the L_3-edge at 851.5 eV (see figure 6.2. In general, the 2p (L-edge) spectrum of Ni^{2+} splits into two main regions, the L_3-edge around 852 eV and the L_2-edge around 869 eV. Whereas the peaks at 851.5 eV as well as 868.5 eV are related to a $2p^5 3d^9$ final state of triplet character, the peaks at 853.8 and 869.8 eV are related to a singlet final state. [6] Accordingly, the splitting between the triplet

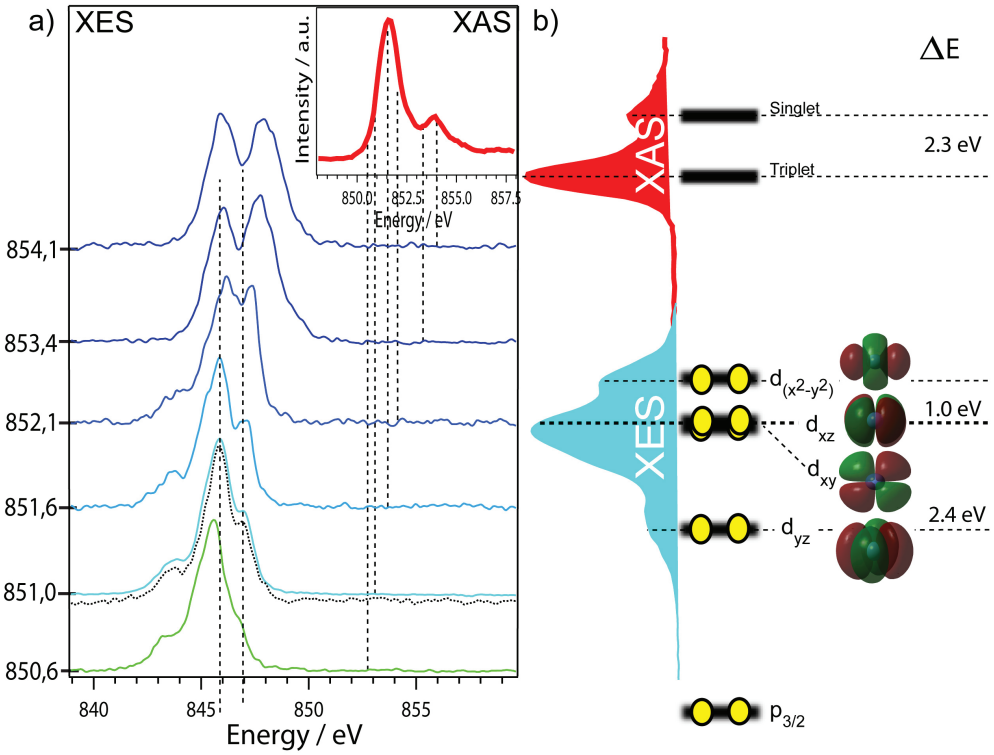

Figure 6.3.: Ni-2p X-ray emission spectra of 1 M aqueous $NiCl_2$: a) emission spectra at different excitation energies labeled in the inset XA spectrum of Ni-2p. For the excitation energy of 851.0 eV also the spectrum of a 0.25 M aqueous $NiCl_2$ sample is shown (dashed line). b) Schematic picture of the occupied and unoccupied Ni-orbitals of in aqueous $NiCl_2$ as obtained experimentally from the XA and XES measurements. The assignment of the orbitals is based on ground state HF-SCRF calculations. [66]

and the singlet states is 2.3 eV, as shown schematically in figure 6.3b. Interestingly, only the triplet state at 851.5 eV is showing a loss of intensity in the FY-spectrum in comparison to the EY-spectrum, which could indicate a weak DCFY, because in a strong DCFY as for the iron ions the spectral features turn to dips [9], as already mentioned. However, a detailed analysis including e.g. transmission, auger electron and partial fluorescence yield absorption measurements is required for separating the influence of the background, saturation effects and the possible DCFY from each other. Such studies were recently presented for Co^{2+} ions in aqueous solutions [107] and further studies also for the here presented system are currently in progress and in planning.
Using XES it is possible to observe the occupied MOs that correspond to the relaxation channels upon excitation into the mixed orbitals. The XE spectra obtained of the 1 M aqueous $NiCl_2$ upon increasing the excitation energy stepwise from 850.6 eV up to 854.1 eV are shown in figure 6.3a. In order to investigate the concentration dependence and the achievable signal to noise ratio for the jet-measurements, also 250 mM $NiCl_2$ in water were measured. Since the XES lines did not change much with respect to the high concentration case, only one spectrum at excitation energy of 851 eV is shown in figure 6.3a. In figure 6.3b, the occupied d-orbitals as obtained for 851 eV excitation energy are presented schematically. The dashed lines correspond to the experimental peak positions. Using ground state HF calculations combined with the SCRF approach, the experimental peaks are correlated to the respective d-orbitals and were labeled accordingly in figure 6.3c. Despite the ground state calculation, the theoretical calculations are in good agreement with the experimental results. Briefly, the theory shows d_{xy} and d_{xz} at the same energy ($\Delta E = 0$). ΔE obtained by HF between d_{yz} and d_{xy} or d_{xz} is 2.4 eV, whereas the experimental ΔE from d_{yz} to d_{xz} is around 2.2 eV. Furthermore, ΔE obtained by HF from d_{xy} or d_{xz} to $d_{x^2y^2}$ is 1.0 eV, whereas the corresponding experimental value is 1.1 eV. In figure 6.3b the emission spectra upon excitation into the triplet state (which could be affected by DCFY) are shown for excitation energies from 850.6 eV up to 852.1 eV. In the respective spectra the emission lines of all the above mentioned d-MOs are observed (see assignments in figure 6.3c). Upon exciting resonantly the electron to the singlet state, XE spectra with only two peaks were obtained (see figure 6.3b, excitation energies 853.4-854.1 eV). The peak correlated to the d_{yz} MO disappeared. According to the DCFY effects shown in the EY-FY comparison for this system, there are mixed Ni-water orbitals formed upon solvation. Upon excitation, the electron can delocalize in these mixed orbitals. If the lifetime of the respective excited state is sufficient, as it is for the triplet state, emission from all occupied d-orbitals is observed. On the other hand, for the singlet excited state with its shorter lifetime no relaxation from the d_{yz} takes place.

Interestingly, upon going to higher excitation energies a blue-shift of the peak correlated to the $d_{x^2y^2}$ MO is observed going along with an increase of intensity. The $d_{x^2y^2}$ MO is the highest of the occupied d-orbitals and therefore most involved in the interaction with the solvent. In principle, one can describe the bond between the Ni^{2+} and the water as semi-covalent bond, according to the MOs mixing pictures drawn here. The intensity increase and the energy shifting of the corresponding spectral feature could be therefore explained by vibronic coupling effects, affecting most the bonding orbitals. [47] Also a blue-shifting of the d_{xy}, d_{xz} and d_{yz} spectral features is observed upon increasing the excitation energy from 850.6 to 852.1. Upon excitation to the singlet state, this systematic shifting is not observed. For a clearer understanding of these effects, however, more systematic studies are required including variation of the solvent.
From the presented measurements the advantage of the micro-jet technique becomes obvious. Comparing the measuring time for the $NiCl_2$ spectra obtained from samples in a cell equipped with Si_3N_4 membrane [5] to the present ones, it was possible to reduce the data acquisition time down to a quarter. A time-dependent chemical reaction with the sample cannot be excluded for the membrane measurements. For larger organic or biological molecules this effect can be significant. Actually, the technique of using the thin membrane can be quite successful under two circumstances, first, short measuring times (in the range of minutes) and second, extensive cleaning between samples with the solvent of choice. Usually these requirements cannot be fulfilled using the XES technique, as for diluted samples (typical for biological and chemical applications) XE spectra can take up to many hours.

6.1.5. Conclusion

The new high resolution XE and XA spectrometer (LiXEdrom) setup for probing the local electronic structure of elements in aqueous solution has been used with a soft X-ray synchrotron light source and the micro-jet technique. With the advantages of the beamline U41-PGM at BESSY II, a small focus and a high flux, the spectrometer is able to probe freshly introduced liquid samples avoiding X-ray induced sample damage. As a demonstration of its capability, in this section two examples of XES results for the application of this spectrometer were presented; (A) liquid water, for which it was shown that the spectra from the micro-jet agree well with the high resolution XES measurements presented recently in the literature. From this, it is concluded that for water there are no long-range effects induced by the membrane affecting the spectra as well as no thermodynamic disequilibrium induced by the jet. (B) For an aqueous so-

lution of $NiCl_2$, it was shown that due to a membrane- less configuration a significant reduction of measuring time is achieved. Moreover, the spectral distortion of XA-FY spectra in comparison to EY spectra of aqueous $NiCl_2$ samples are presented. The vibronic-coupling in the XES peaks suggests a semi-covalent bond between the Ni^{2+} and the water hydration.

6.2. The Hydrogen Bond of Water in Solvents of Different Polarity: An FT-IR Study

Reprinted with permission from Lange et al., Journal of Physical Chemistry B 114, 50, pp. 16997-17001. Copyright 2010 American Chemical Society
http://dx.doi.org/10.1021/jp109790z

6.2.1. Introduction

Just recently, the long-standing textbook knowledge of a tetrahedrally oriented structure of the hydrogen bond network of the molecules in liquid water [18] was challenged, based on experimental XA studies of the oxygen K-edge of bulk water and ice as well as on DFT calculations. [122] Instead, a coexistence of strong and weak donor and acceptor hydrogen bonds was proposed. This interpretation was, however, strongly criticized later. [108] Actually, XAS as well as XES are particularly sensitive tools for probing the electronic structure, which allows conclusions on the geometrical structure of a molecular system. Just recent instrumental developments allowed investigation of the K-edge of the oxygen of liquid water using soft X-rays. [5, 86] A particular difficulty of hitherto studies of water is, however, that bulk water was the subject of study and accordingly the obtained spectra represent an average over a broad ensemble of hydrogen bonding states. In this pre-study an approach should be found to bypass this inherent ambiguity of studying the bulk liquid. The goal is to isolate water molecules in liquid phase by using organic solvents. The behaviour of the water molecules is monitored using FT-IR spectroscopy. FT-IR reveals information about the vibrational structure of a sample and is therefore a sensitive tool for determining the binding partners of the water molecule as well as the symmetry of the binding. In the next step (see section 6.3) these results are used for measuring XA and XE spectra of isolated water molecules and to determine the influence of hydrogen bonds on the experimental spectra by progressing successively from isolated water molecules to bulk states in the liquid phase.

6.2.2. Samples and Experimental Methods

In order to investigate experimentally the hydrophobic hydration, the solvents benzene (nonpolar) and chloroform (polar) and acetonitrile (hydrophilic) in mixtures with water are compared. The solvents were of the following quality characteristics: Acetonitrile, anhydrous, 99,8 % (Sigma-

Aldrich), Benzene, anhydrous, 99,8 %, water < 0.001 % (Sigma-Aldrich), Chloroform, anhydrous, stabilized with amylenes, > 99 %, water < 0.001 % (Sigma-Aldrich). To assure the purity of all solvents a molecular sieve (grain size 4 $\mathring{A}$) was used for further purification, which was added to the solvents 24 hours before the experiment. For the later XA as well as XE measurements at the oxygen K-edge it was important to use solvents without stabilizers containing oxygen. In order to avoid an uncontrolled take-up of water from the environment, the samples were prepared under helium atmosphere, or dry air flowing inside a glovebox. Furthermore, the use of the glovebox was necessary due to security reasons (The used solvents are highly flammable and noxious, respectively). The water which has been used in the experiments was deionized and filtered with a Millipore water purifier system, having a specific resistance of 18 MΩ. The sample solutions were prepared in an ultrasonic bath at a fixed temperature of 25.0 ± 0.1 °C, and injected directly into the FT-IR liquid cell using a syringe. In order to clear the liquid cell, as well as the supply and the drain tubes from remnant water, between the experiments the system was flushed successively with ethanol and acetone, followed by dry air or helium, and the respective pure solvent for each run. Due to the exceptional sensitivity of the method used, measurements with extremely low water concentrations (0.01 vol%) were possible, which allows to obtain spectra of isolated water molecules and to control their successive clustering upon increasing concentration.

6.2.3. Results

Figure 6.4 shows the intensity normalized IR spectra obtained from 0.01 g of water added to 50 g of acetonitrile (red), benzene (green), and chloroform (blue), in comparison to the spectra of bulk water [101] and ice [27], taken from literature. In the bottom of figure 6.4 the antisymmetric and the symmetric stretching modes ν_3 and ν_1 for the gas phase are marked. [71] It is clear that the vibration structure of the isolated molecule in vacuum differs from that of the isolated molecule in a solvent. In the spectrum of 0.01 g of water in 50 g of chloroform, the peaks belonging to the ν_3 and ν_1 modes appear at 3690 and 3607 cm^{-1}, respectively. [46] In benzene and acetonitrile, these modes are shifted to lower wavenumbers. For bulk water [101] and bulk ice, [27] the modes ν_3 and ν_1 appear at even lower wavenumbers, forming broad and intensive bands around 3400 cm^{-1} (superposed by the $2\nu_2$ mode) and 3250 cm^{-1}, as shown in the top part of figure 6.4. According to the Badger-Bauer rule, [11] this shifting to lower wavenumbers is caused by an increase of the hydrogen bond strength. Correspondingly, the IR spectrum of isolated water molecules in chloroform shows the weakest bonding interaction. This is due to the

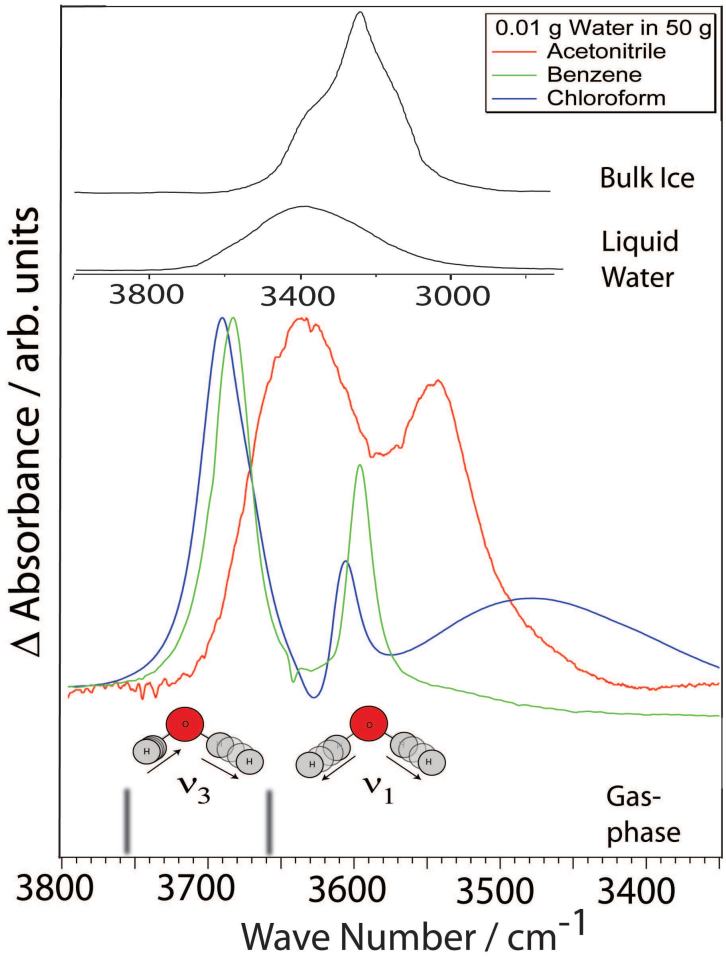

Figure 6.4.: FT-IR spectra of 0.01 g of water in 50 g of acetonitrile (red), benzene (green), and chloroform (blue). For comparison the IR spectra of bulk ice [27] and pure water [101] are presented as well as the energies of the gas phase stretching modes ν_3 and ν_1. [71]

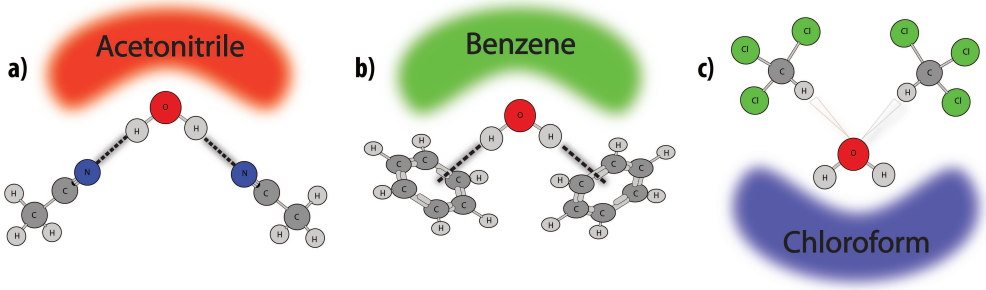

Figure 6.5.: Schematic picture of isolated water molecules in a) acetonitrile b) benzene and c) chloroform. [65]

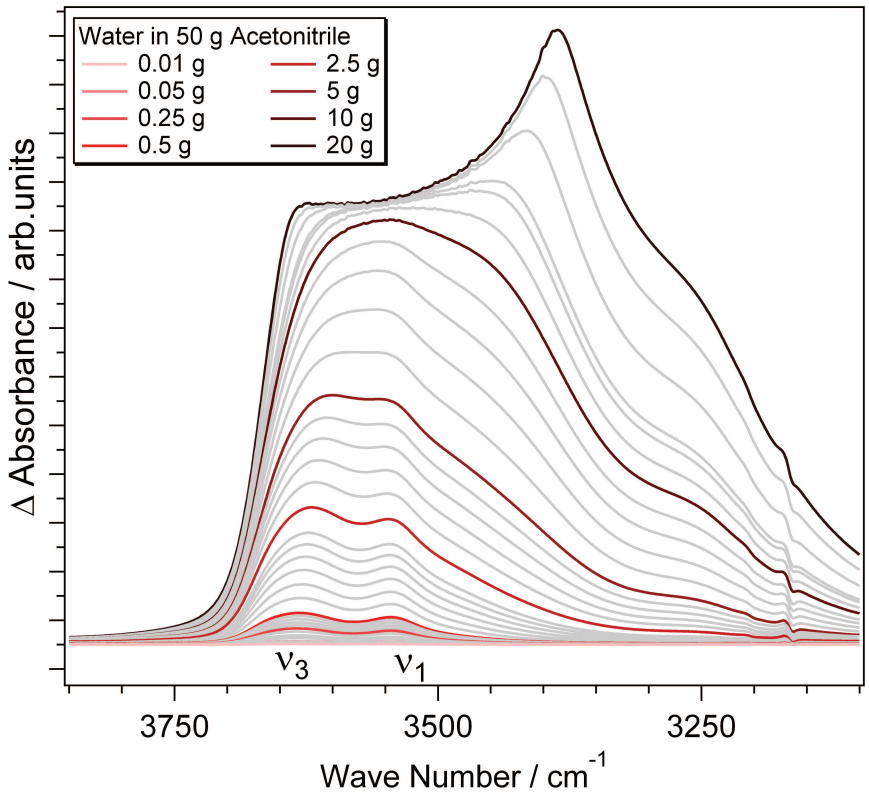

Figure 6.6.: FT-IR spectra of water-acetonitrile mixtures of different concentration ratios. [65]

fact that chloroform is a pure proton donor [72] and will bind exclusively with the lone pairs of the oxygen of the water molecule (see schematic picture in figure 6.5c). A stronger hydrogen bond is formed between the hydrogen of the water and the delocalized π-electron cloud of the aromatic ring of benzene (see schematic picture in figure 6.5b). [4] The strongest bond among the three systems is formed between the hydrogen atom of the water and the nitrogen atom of the acetonitrile, [30] which is a pure hydrogen bond acceptor [120] (see schematic picture in figure 6.5a). The broadening of the stretching bands in acetonitrile, compared to benzene and chloroform, is due to an increased hydrogen bond strength which is correlated to anharmonicity effects. [105] A comparatively strong hydrogen bonding takes place among the water molecules in bulk liquid water, which is still exceeded by the hydrogen bonding in ice. It is well-known that the two stretching modes ν_1 and ν_3 of the water molecule are coupled modes, which occur when both hydrogen atoms are exposed to substantially equivalent force fields; i.e., both are either bonded with a comparable strength or nonbonded. [46] If the bonding configuration is asymmetric and one of the OH groups is nonbonded, a respective stretching mode of the free OH group is expected in the spectrum between 3650

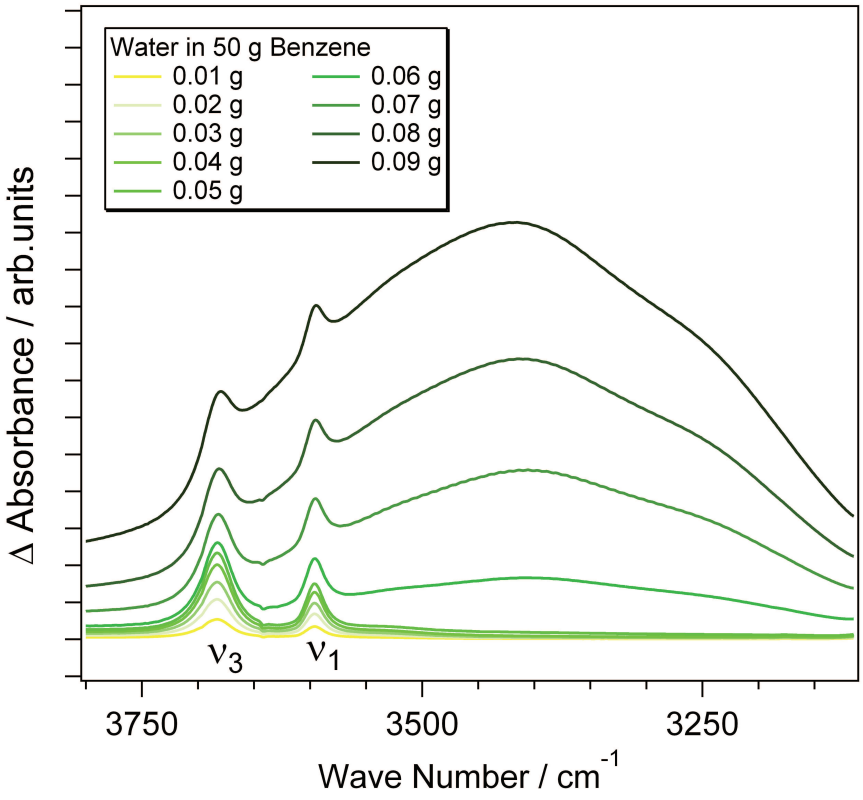

Figure 6.7.: FT-IR spectra of water-benzene mixtures of different concentration ratios. [65]

and 3800 cm^{-1}. [46] Thus, the FT-IR spectra reveal that, in acetonitrile and benzene at the lowest measured water concentration, the water molecules are isolated and symmetrically hydrogen bonded to the solvent. In the chloroform spectrum, the broad band around 3480 cm^{-1} appears. This feature is correlated to water clustering with cluster sizes larger than pentamers. [99] Therefore, referring to water clustering in the following always indicates a cluster size above pentamers. The shoulder at 3670 cm^{-1} fingerprints the occurrence of single free O-H groups in these clusters. For acetonitrile and benzene, no band belonging to free OH groups is observed.
The specific nature of the hydrogen bonding of liquid water reveals itself upon raising the concentration of water in these solvents. The distinct properties of the solvents in terms of polarity, hydrophobicity, and solubility for water allow a comprehensive investigation of the emerging water structures. In the IR spectra, the onset of hydrogen bonding among water molecules forming water clusters is indicated by the appearance of the respective bands around 3450 cm^{-1}. Note that neat water shows a broad band around 3400 cm^{-1}, as shown in figure 6.4. [101] For water in acetonitrile (figure 6.6), upon raising concentration an equal increase

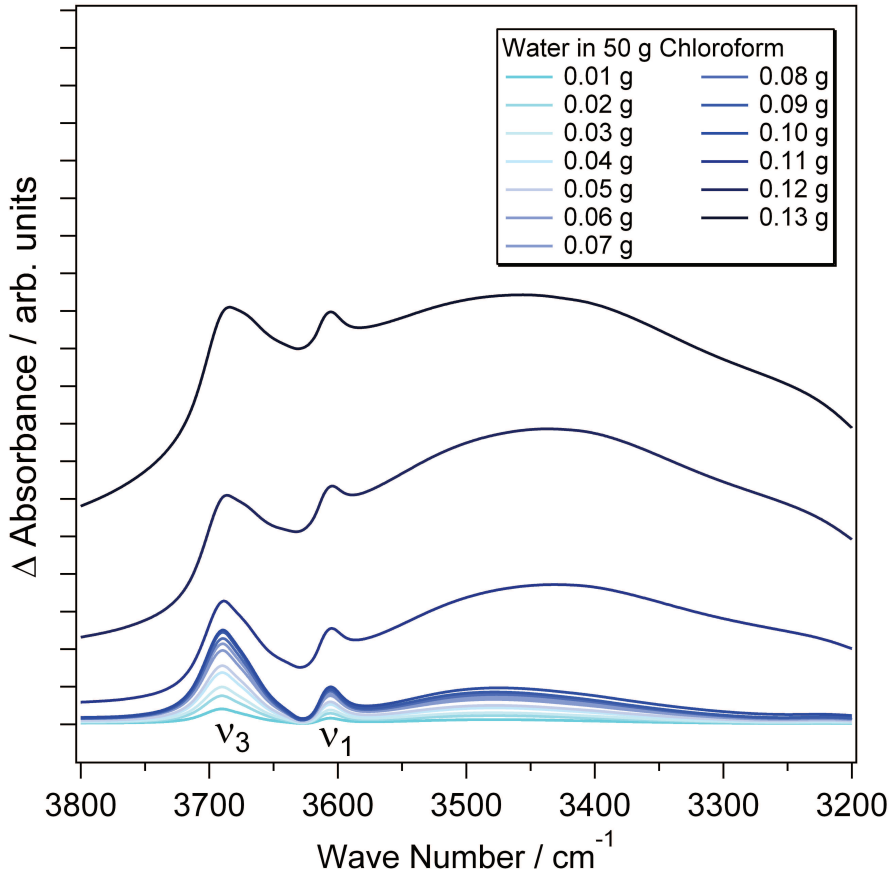

Figure 6.8.: FT-IR spectra of water-chloroform mixtures of different concentration ratios. [65]

of the ν_3 and the ν_1 bands intensity is observed, up to about 0.5 g of solute water. A further increase of the water content leads to the rise of additional bands around 3400 cm^{-1}. These bands indicate a clustering of water molecules within the solvent. In benzene (figure 6.7), water clustering occurs at much lower concentrations than in acetonitrile. For a water content of 0.03-0.04 g, water molecules bonding among each other are observed in the IR spectra. In chloroform, water clustering was observed already at the lowest concentration measured. Upon raising the content of water in the chloroform up to 0.1 g (see figure 6.8), the bulk water absorbance increases systematically, in parallel with a proportional rise of the ν_3 and ν_1 peaks. A further increase of the water concentration leads to a fast rising of the bulk water absorbance, which is proposed to result from the formation of bulk water conglomerates behind the membrane (phase separation), as in the case of high water concentrations in benzene.

6.2.4. Conclusion

In summary, in this chapter information about the hydrogen bond formation among water molecules in different organic solvents are provided. Depending on the nature of the solvent, significantly varying clustering behaviour was observed. For chloroform water clustering took place already at the lowest concentration measured, making it not an ideal candidate for the study of isolated water molecules. In benzene and acetonitrile the isolation of single water molecules was achieved. Both solvents could be accordingly used for further studies. Upon measuring XA and XE spectra of water-acetonitrile and water-benzene mixtures the influence of the different hydrogen bond types, for acetonitrile to a single nitrogen atom and for benzene to the π-electron cloud of an aromatic ring could be studied. The high solubility of water in acetonitrile makes it the first candidate of choice for the following XA and XE studies of the oxygen K-edge.

6.3. The Hydrogen Bond Network of Water: XA and XE Study of Water in Acetonitrile

Lange et al., Angewandte Chemie International Edition 50, 45, pp 10621-10625 (2011)
http://dx.doi.org/10.1002/ange.201104161

6.3.1. Introduction

XE spectroscopy probes the occupied electronic states upon detecting the energy distribution of the radiative decay of the core-hole state. The recent development of high resolution XE spectrometers for liquid samples drew particular attention to the observation of the splitting of the sharpest peak in the spectrum associated with the lone-pair orbital of the free water molecule. [43, 116, 118] In section 6.1 of this work, the first XE spectra of water obtained from a membrane free spectrometer confirmed, that this splitting is not a membrane-correlated artifact. Tokushima *et al.* interpreted the double feature as a further proof for the existence of two different structures, the tetrahedral and strongly distorted hydrogen-bonded species. [118] Fuchs *et al.* assign the two distinct peaks to emission from species before and after core-hole-induced ultrafast dissociation. [43] Experimental approaches to clarify the origin of the peak splitting included temperature-, isotope- and state of aggregation dependent measurements as well as the study of the proposed dissociated species.
To shed further light on this issue, in this chapter XA and XE spectra of the water molecule are presented in a chemical environment where the hydrogen bond configuration is radically different from that of liquid water. For this the water molecules were isolated in acetonitrile. According to the FT-IR results of the previous section, this is achieved in water-acetonitrile mixture with around 1 vol% water contribution. In this section the XA and XE of water acetonitrile mixtures down to 1 vol% water concentration are presented.

6.3.2. Experimental Methods

The experiments were carried out at the U41 PGM undulator beamline of the BESSY II synchrotron facility using the LiXEdrom setup. [66] The recorded spectra were curve corrected. The calibration of the spectra was done according to Tokushima *et al.*. [116]
The samples were filtered and degassed. For mixing a magnetic stir bar

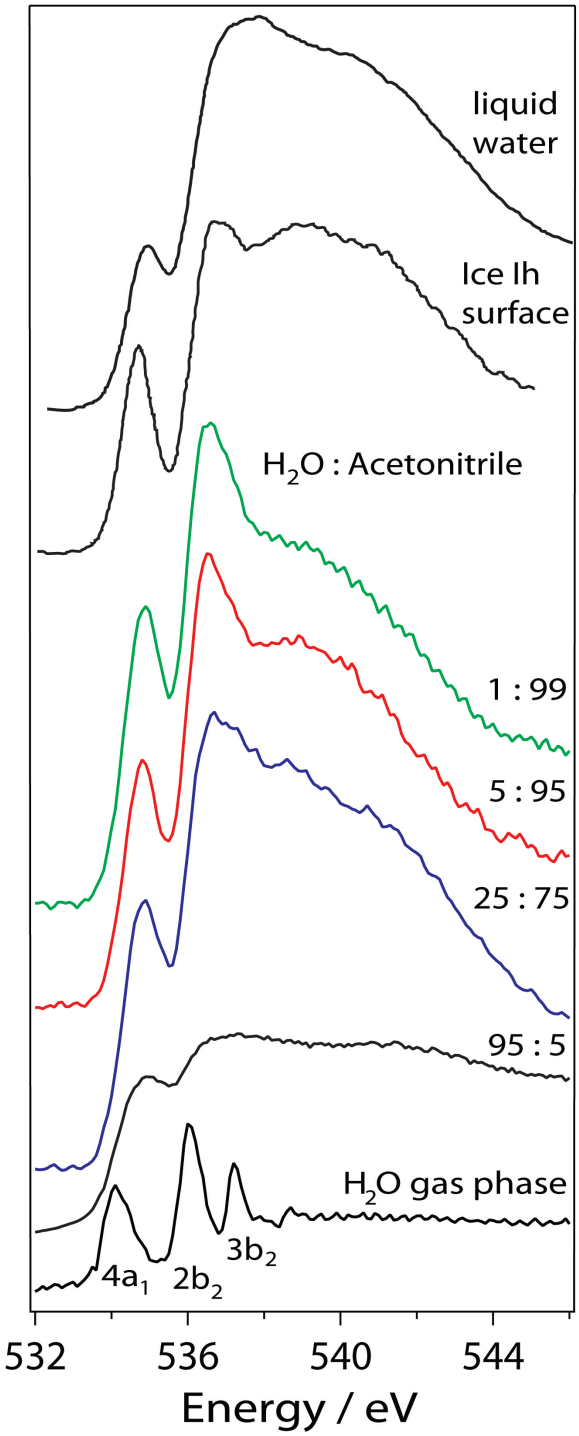

Figure 6.9.: Oxygen K-edge X-ray absorption spectra of water-acetonitrile mixtures of four different concentration ratios. The spectra of an Ih ice surface, [122] liquid [122] and of gas phase H_2O are shown for comparison

was used. The liquid micro-jet had a nozzle of around 16 μm diameter. The sample was introduced with a flow-rate of 0.4 ml/min to the setup. The spectra were recorded from the jet-region of laminar flow with a distance of around 1 mm with respect to the nozzle opening. Evaporative cooling leads to a decrease of temperature along the jet-axis. Based on the calculations and the experimental data in reference [124] the temperature of the liquid in the probing zone was estimated to be around 15 °C.

6.3.3. Results and Discussion

Figure 6.9 shows the total fluorescence yield XA spectra at the O K-edge of water-acetonitrile mixtures of 95, 25, 5 and 1 vol% water content. At 95 vol% the spectrum is very similar to the spectrum of neat liquid water, showing the three principal pre- (535 eV), main (537 eV) and post- (540 eV) edge features. However, it is strongly saturated [35] leading to an overemphasizing of pre- and post-edge with respect to the main-edge intensity. [84] With decreasing water concentration saturation is significantly reduced and compared to the pure liquid water spectrum a relative enhancement of the main-edge is observed. In addition, the shape of the spectrum changes character, so that at 1 vol% the pre-edge structure becomes clearly resolved, the main-edge appears as a sharp feature, and the relative intensity for the post-edge is attenuated. Thus, the XA spectrum of the 1 vol% water-acetonitrile mixture now deviates considerably from the spectrum of neat water and instead it increasingly resembles the spectrum of gas-phase water (figure 6.9), with the pre- and the main-edge correlating with the $4a_1$ and the $2b_2$ resonances of the free molecule. It has to be mentioned that the XA spectra shown here differ significantly from previous XA measurements using a membrane cell. [66] The present data is free from any artifacts which may be introduced by structuring due to interaction with a membrane. As the sample is rapidly renewed in the micro-jet setup also any photoinduced restructuring is ruled out. Previously published spectra may be influenced by such effects. [65]

Before the experimental results are discussed further, the molecular arrangement of water and acetonitrile in the mixture will be considered. The hydrogen bonds of each water molecule are considerably reduced compared to the hydrogen bonds of molecules in pure water. At 1 vol%, there are around 34 acetonitrile molecules per water molecule and the water molecules are mostly surrounded by the acetonitrile molecules. [30] Acetonitrile is usually considered to be a pure hydrogen bond acceptor, even though it has been proposed that also interactions of the methyl-protons of the acetonitrile with the oxygen of the water are possible. [62] Using molecular dynamics (MD) simulations in combination with infrared and far-infrared measurements, Venables *et al.* [120] concluded that the

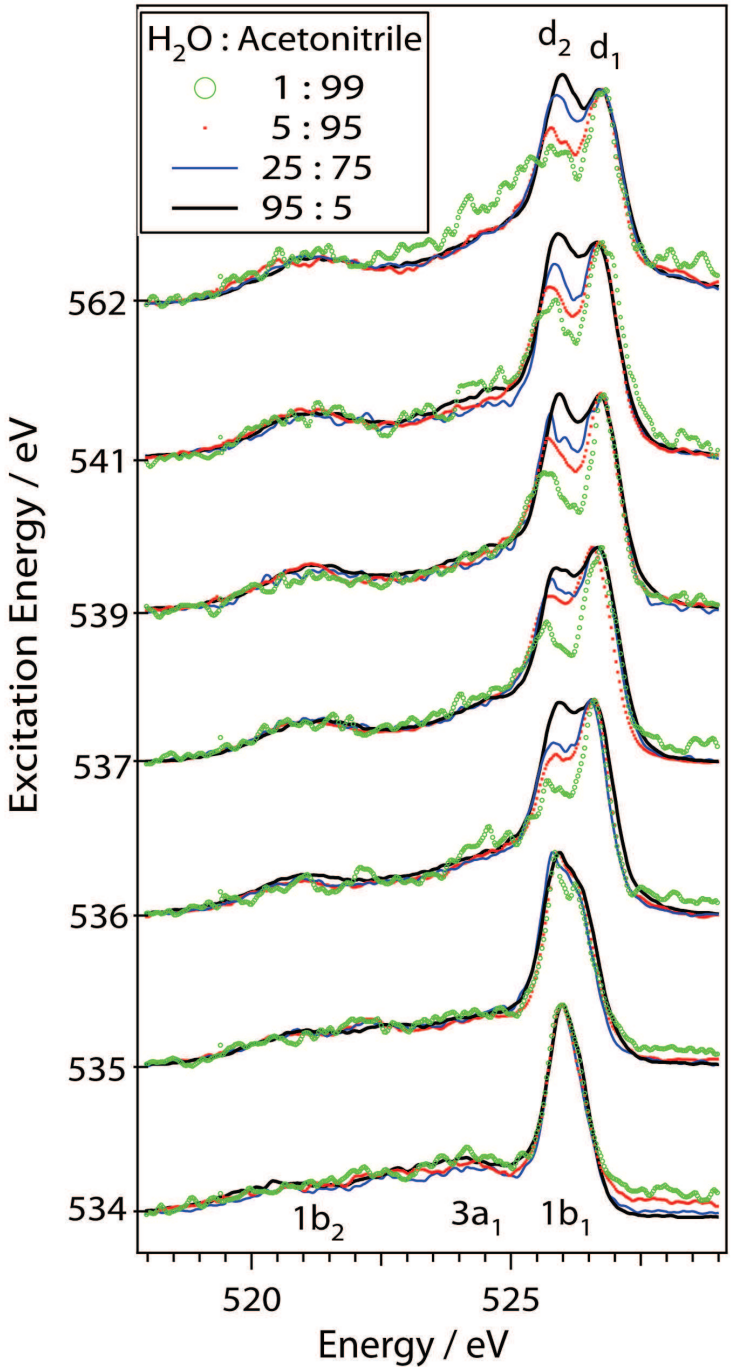

Figure 6.10.: Series of X-ray emission spectra of water-acetonitrile mixtures of four different concentration ratios obtained from a micro jet. The spectra are normalized on d_1 intensity.

number of hydrogen bonds accepted by a water molecule significantly drops from 1.75 for neat water to 0.5 for a 7 vol% mixture, whereas the number of donated hydrogen bonds decreases only slightly from 1.75 to 1.65. At lower concentrations, any water clustering is absent, and based on calibrated multiple attenuated total reflection spectroscopy Bertie and Lan concluded that the fraction of bonded OH-groups decreases from 0.865 in neat water to 0.45 in the limit of low water concentration, [18] in which the remaining O-H···N donor bonds are weaker than the O-H···O bonds in liquid water. [65] As compared to the free molecule one can observe that condensation effects are present even without hydrogen bonds, and one can expect that features corresponding to resonances in the free molecule will be broadened and shifted due to dipole-dipole interaction and different relaxation in gas and condensed phase. Also in the absence of hydrogen bonds Rydberg resonances will be smeared out in the liquid due to the large extension of the orbitals.

Thus, hydrogen bonds break with decreasing water concentration, and in the 1 vol%-solution one may expect only some remaining donor bonds to acetonitrile. In general, this explains why the 1 vol%- spectrum shows similarities with the gas-phase spectrum. The character of the first two unoccupied orbitals is retained to the level where they give rise to two distinct peaks, and the third gas-phase resonance is smeared out due to its Rydberg character. The relative attenuation of post-edge intensity is in line with its interpretation as due to highly coordinated water molecules and with the absence of a corresponding resonance in the gas-phase. Similar trends are observed in the XA spectrum of an Ih surface layer of ice (Ref. [122], shown in figure 6.9 for comparison) where asymmetric hydrogen bonding prevails. For the surface molecules it was estimated that the molecules have 1.2 donor hydrogen bonds on average. Note that the here presented XA spectra are very similar to recently measured hard X-ray Raman spectra of acetonitrile-water solutions. [53]

For each water-acetonitrile mixture a series of XE spectra was recorded (see figure 6.10). For high water concentrations the spectra are in agreement with previously published XE spectra of liquid water, [44, 66, 116, 118] showing a sharp $1b_1$ lone-pair-derived peak around 527 eV, followed by broader $3a_1$ (∼525 eV) and $1b_2$ (∼521 eV) derived features. With increasing excitation energy the $1b_1$-feature splits up into two distinct features, labeled in the following d_1 (high-energy) and d_2 (low-energy) as by Fuchs *et al.*. [44] The relative intensity of the d_2 feature is dramatically attenuated when the water concentration is reduced. Following the discussion above this behaviour can be unambiguously attributed to the breaking of hydrogen bonds. Conversely, this directly demonstrates that a substantial part of the d_2 intensity indeed is due to the formation of hydrogen bonds, in line with earlier interpretations. [116,118] In addition one should note that apart from this striking influence of hydrogen bond

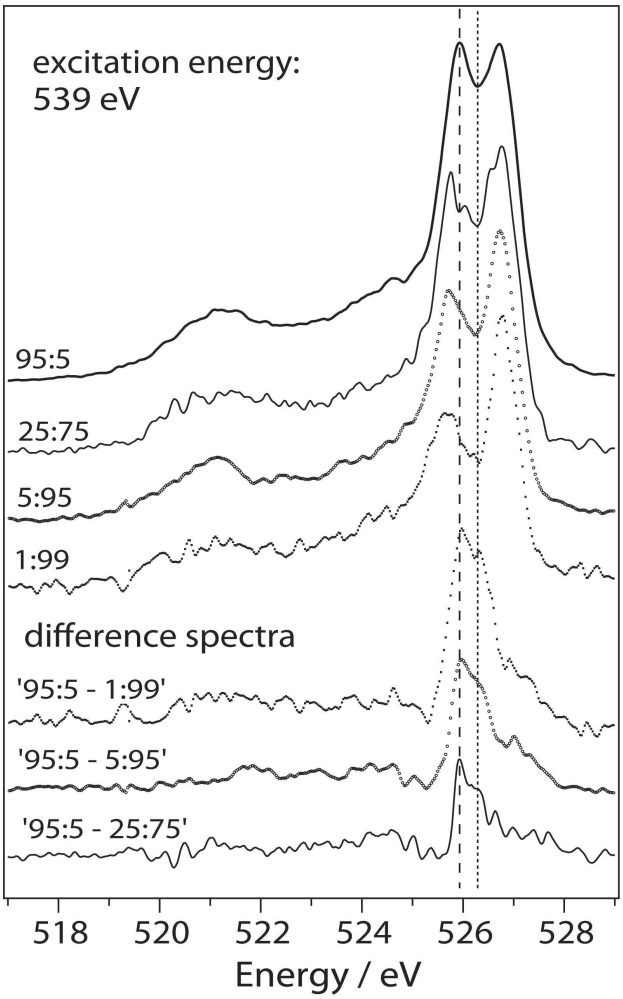

Figure 6.11.: Spectra of water-acetonitrile mixtures excited at 541 eV and difference spectra. In order to avoid negative residuals weight factors were used for the subtraction.

formation the spectra (figure 6.10) seem rather little influenced by the chemical environment. The non-resonantly excited spectrum approaches with decreasing water concentration to gas-phase spectra, which show only one $1b_1$ related feature. [60, 118] Note, however, that even for the 1 vol% solution the additional d_2 feature is still present. Although published gas-phase spectra differ considerably in intensity ratios and peak broadening from each other, [60, 118] the further major difference compared to the low-concentration spectra appears to be a uniform energy shift.

The expected XE shift going from gas-phase to liquid water can be estimated by comparing the shift of the binding energies of the core and valence holes states. According to Ref. [89] the core-level binding energy decreases by 1.91 eV while the $1b_1$ shift is 1.39 eV. Neglecting differ-

ences in excitation dynamics between direct photoemission and XE one would thus expect a low-energy shift of the $1b_1$-derived feature of 0.52 eV, whereas a direct measurement [118] gives a low-energy shift of around 0.3 eV if the d_1 feature is identified with the $1b_1$ hole state. For weakly interacting molecules it is known that the major effect of condensation is a uniform shift of all spectral features, while the overall spectral shape is preserved. [90] The observations are fully consistent with the notion that the water molecules in the low-concentration solution interact only weakly with the surrounding. At increasing water concentration the interaction increases, and the changes in the spectra can be unambiguously assigned to this interaction. Obviously the spectrum is largely independent of the stronger hydrogen bond interaction, while the most striking change is the increasing relative intensity of the d_2 feature.
The association of the d_1 feature to less coordinated species and a major part of the d_2 intensity to highly coordinated species can thus be done on a firm experimental ground. This conclusion is reached without any advanced theoretical considerations, which in complex situations like this necessarily invoke approximations which can be questioned.
In the following some details will be discussed in the light of the current debate on the origin of the splitting of the lone-pair derived feature. [43,44]
To emphasize the spectral changes induced by hydrogen bond formation the spectra of solutions with low water content were subtracted from the 95 vol% spectrum for three different excitation energies (see figures 6.11, 6.12, 6.13). The result of the subtraction is critically dependent on the relative normalization of the spectra, and in the presented spectra the maximum intensity which does not lead to negative residual intensity was chosen.
The difference spectra are completely dominated by a feature at an emission energy around 526.0 eV, and this energy position is independent of concentration. Furthermore it has internal structure showing intensity not only at the d_2 peak but also a high-energy shoulder extending under the d1 peak (see dashed and dotted line in figures 6.11, 6.12, 6.13). In the case of ultrafast dissociation one would expect the residual to resemble the XE spectrum of the dissociation product OH^- which is as Fuchs *et al.* point out upon resonant excitation dominated by a peak very close in energy to the d_2 peak. Although this is in line with the present observations, the internal structure observed in the residuals shows the limitation of any attempt to describe the water XE spectra as a simple superposition of emission from intact and dissociated species. If the d_2 emission were due to intact molecules [116] one would expect that the residuals resemble a shifted water molecule spectrum. Recently it was predicted that hydrogen bonds influence an asymmetry in the d_1 peak towards lower energies, and that the variation in relative intensity of this low-energy flank significantly contributes to the apparent variation of the

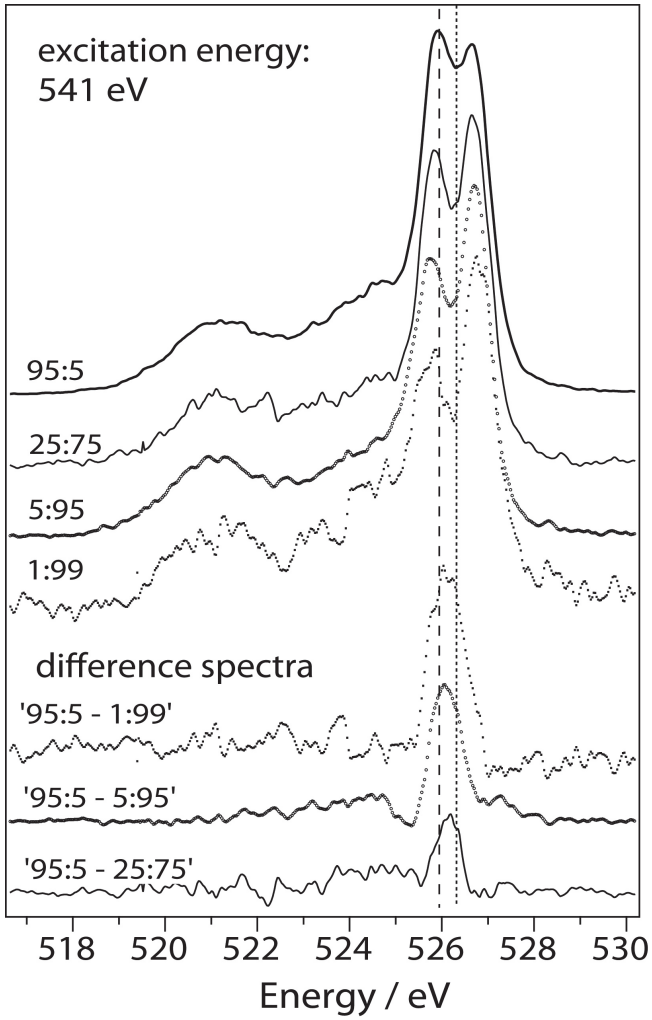

Figure 6.12.: Spectra of water-acetonitrile mixtures excited at 541 eV and difference spectra. In order to avoid negative residuals weight factors were used for the subtraction.

d_2 intensity. [73] The fact that much intensity in the difference spectra is found between the d_1 and d_2 peaks speaks is in line with this prediction. If the residual has contributions both from d_2 and changes in the asymmetry of the d_1 peak, $1b_2$ and $3a_1$ intensity of the shifted spectrum may be below the detection limit.
Finally one can observe that the spectra resonantly excited at the XA pre-peak are virtually independent of the water concentration. This is in line with the notion that the pre-peak largely is due to species where hydrogen bonds are already broken in the liquid water and that the excitation in this case is local at a specific molecular site.

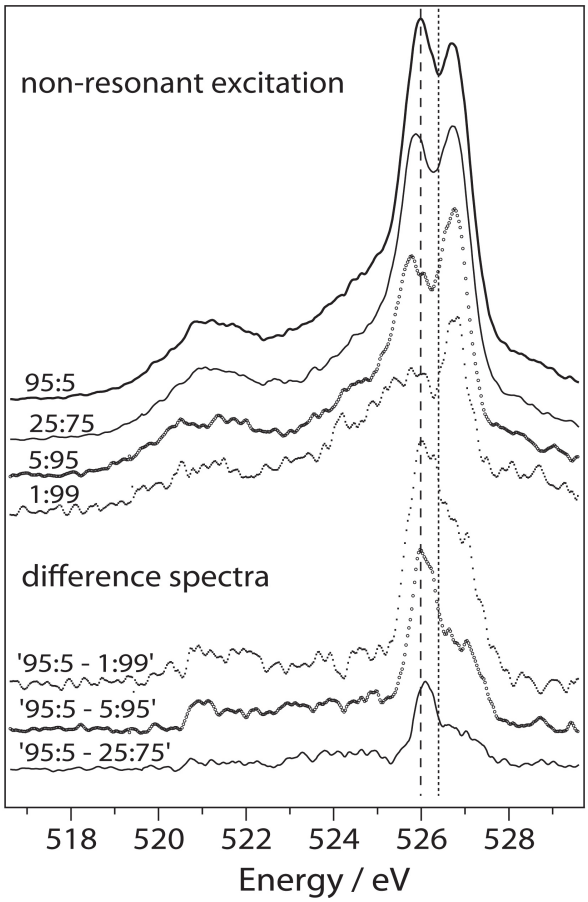

Figure 6.13.: Spectra of water-acetonitrile mixtures excited at 541 eV and difference spectra. In order to avoid negative residuals weight factors were used for the subtraction.

6.3.4. Conclusion

In this chapter the impact of reducing the water concentration in acetonitrile, which goes along with a reduction of hydrogen bonds per water molecules, on XA and XE spectra was studied. The results confirm that both techniques are very sensitive to the hydrogen bond environment. XA intensity at the pre- and main-edges is enhanced relative to the post-edge intensity upon hydrogen bond breaking and it is found that condensation effects are important for the XA spectrum even without hydrogen bonds. In the XE spectra the low-energy component of the sharp double feature is relatively reduced upon hydrogen bond breaking, and its relative intensity can thus be used as a probe for hydrogen bonds. This can be concluded without theoretical modeling. To understand the detailed mechanisms behind the variations, however, further investigations are needed.

6.4. On the Influence of Nuclear Dynamics: XA and XE of D_2O-Acetonitrile Mixtures

Lange et al., Physical Review B 85, 155104 (2012)
http://dx.doi.org/10.1103/PhysRevB.85.155104

6.4.1. Introduction

A crucial point of disagreement in the discussions on the X-ray emission spectra of water concerns the role of nuclear dynamics and the role of static hydrogen bond conformation for the spectrum formation. In attempts to settle this issue isotope and temperature effects have been thoroughly measured and discussed, without leading to a consensus regarding the assignment. [43, 116, 118] To isolate the hydrogen bond conformation effects the XE spectrum of neat H_2O was compared in the previous section with the spectrum of H_2O as a solute in acetonitrile. In the latter case the number of hydrogen bonds is significantly reduced, and thus the corresponding spectral change could be isolated. The question about the role of dynamics remained open because the dynamics is highly dependent on the hydrogen bond coordination. In this section influence of dynamics was varied by performing the corresponding study also for D_2O, where the nuclear dynamics is slower than in H_2O. The results that the spectral response on increased hydrogen bond coordination is significantly different from the response on increased nuclear rearrangement. The two effects can thus be separated experimentally, thereby establishing a firm ground for interpreting X-ray spectra of liquid water.
A further uncertainty in the current discussions stems from the fact that for most experiments so far ultrathin windows are used which potentially interact with the liquid. If the sample is only slowly replenished photolysis may also influence the structure and thus details in the spectra. [65, 67, 118] Here a liquid micro-jet was used to avoid such problems.

6.4.2. Experimental Method

The experiments were carried out at the U41 PGM undulator beamline of the BESSY II synchrotron facility using the LiXEdrom. [66] The samples were introduced with a liquid jet of 16 μm nozzle size. The parameters of the measurements are the same as presented before in section 6.3. The calibration of the spectra was done according to Tokushima *et al.*. [116] The X-ray emission spectra in figure 6.15, 6.16 and 6.17 were normalized on the $1b_2$ intensity. The spectra in figure 6.18 were area normalized.

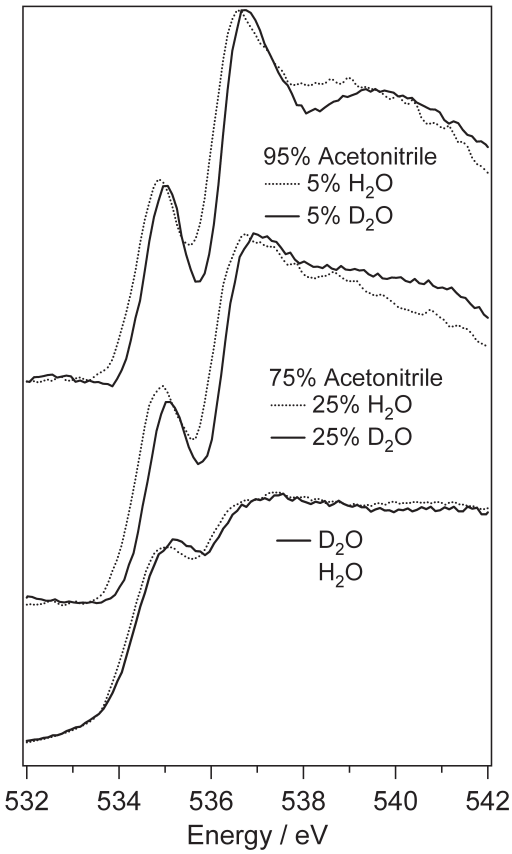

Figure 6.14.: K-edge X-ray absorption spectra of pure D_2O and D_2O-acetonitrile mixtures. For comparison the respective spectra of H_2O-acetonitrile mixtures are shown in dotted line.

6.4.3. Results and Discussion

In agreement with earlier studies the fluorescence yield (FY) spectra of both H_2O and D_2O show three characteristic features (see figure 6.14): a pre-edge around 535 eV, a main-edge around 537 eV and a post-edge around 540 eV. [122] For the pure liquids the spectra are strongly saturated [35] which leads to an overemphasizing of the pre- and post-edge with respect to the main-edge. [84] The saturation effects are reduced in the spectra of the 25 vol% solution, the post-edge intensity becoming relatively attenuated, and the pre-edge feature a well separated peak. The changes can also partly be attributed to the reduced hydrogen bond coordination, [65] which becomes even more accentuated in the 5 vol% solution. The features of the D_2O spectra are very similar to the H_2O features, at all measured concentrations. The principal differences comprise

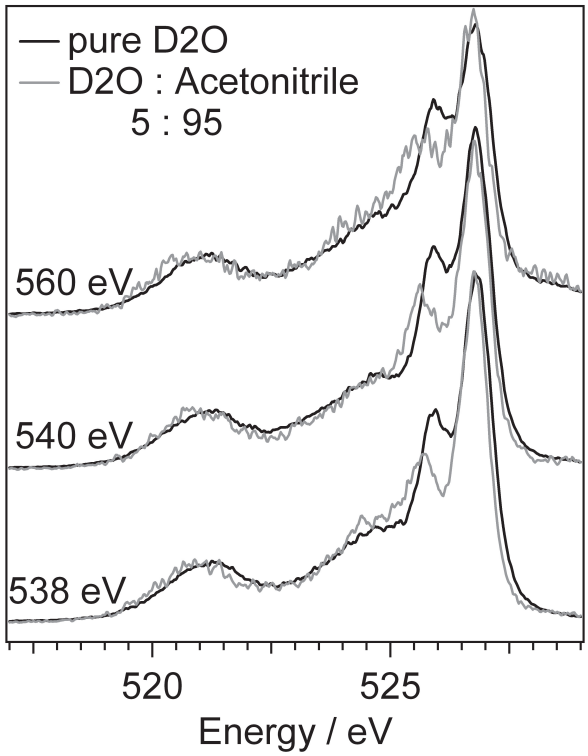

Figure 6.15.: X-ray emission spectra of D_2O and of 5 vol% D_2O-acetonitrile mixtures for three different excitation energies

a general small (0.2 eV) high-energy shift of the entire spectrum, and an additional sharpening of the main features. This isotope effect has been discussed before for the pure liquids, and can be understood in terms of the slower dynamics and the shift of the ground state zero point energy, [87] due to the heavier nuclei. Thus, there is no need to refer to the small structural differences between the H_2O and D_2O liquids to describe the spectral differences. Whereas the interaction between H_2O and acetonitrile has been well investigated over the whole concentration range, datasets for low D_2O concentrations in acetonitrile are rather scarce. The systematic changes in the XA spectra indicate that also for D_2O the number of intermolecular bonds is reduced upon dilution in acetonitrile, and the fact that the changes are similar in the two cases suggests that the reduction in hydrogen bond coordination is similar for H_2O and D_2O.

In the following the dramatic isotope and dynamic effects in the XE spectra are discussed (see figures 6.15, 6.16 and 6.17). All spectra have a broad feature at 521 eV and a sharp peak at 526.7 eV in common. Following the accepted interpretation of the gas-phase spectrum, these features are correlated to with states derived from the bonding $1b_2$ orbital and the "lone-pair" $1b_1$ orbital, respectively. In the region between these two peaks two features at around 524.4 eV and 525.6 eV can be identified,

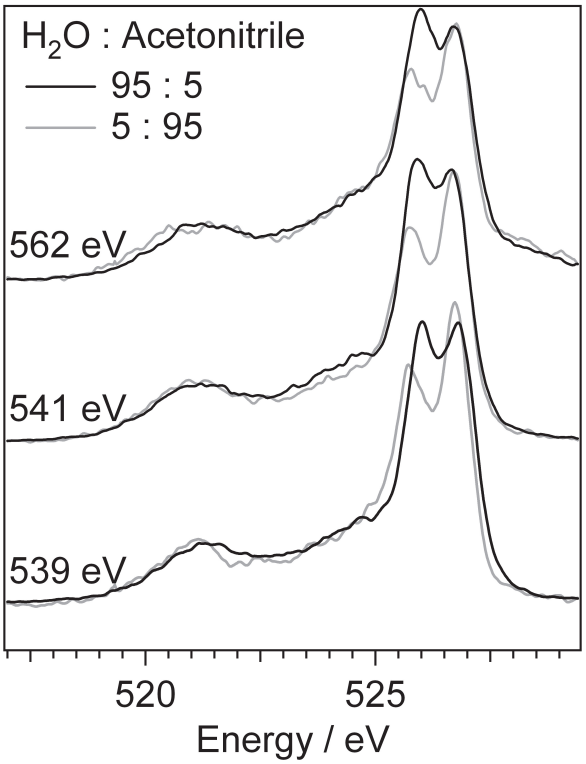

Figure 6.16.: X-ray emission spectra of H_2O and of 5 vol% H_2O-acetonitrile mixtures for three different excitation energies

where especially the latter is very sensitive to changes is dynamics and coordination. Again led by the assignment in the XE spectra of the free molecule the 524.4-eV feature is associated with $3a_1$-derived states. The 525.6-eV feature will be initially not correlated to orbital symmetry and instead labeled d_2, in-line with previous work. [43] The behaviour in this energy range will be discussed below.

The XE spectrum of the 5 vol% D_2O solution is shown in figure 6.15. One expects that this XE spectra of D_2O as a solute in acetonitrile most closely should mimic the spectra of a free molecule. Here the hydrogen bond coordination as well as dynamics due to interaction with the surrounding is reduced. Indeed the spectra show similarities to the gas-phase XE spectrum of H_2O. [104, 117] Whereas for XE spectra of free water molecules vibrational fine structure is expected if the experimental resolution allows, [24] in a hydrogen bonding liquid additional broadening due to the interaction with the environment will intrinsically smear out any vibrational fine structure. [112] Although the experimental resolution does not allow to address this question here, the similarities to the gas-phase spectra suggest that internal vibrations are the main reason for the different widths of the $1b_1$ and $1b_2$ features also in the D_2O case.
The spectral change accompanying increased hydrogen bond coordination

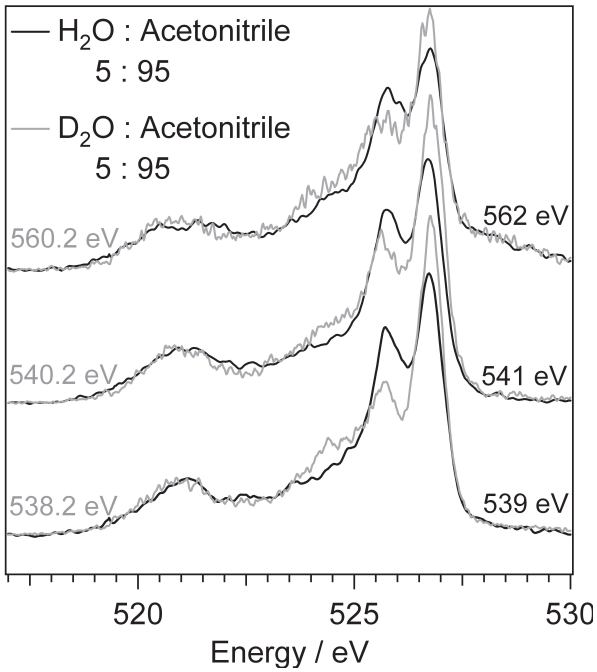

Figure 6.17.: X-ray emission spectra of 5 vol% H_2O-acetonitrile mixtures and 5 vol% D_2O-acetonitrile mixtures for three different excitation energies

(pure D_2O in figure 6.15) is primarily an increase in intensity of the d_2 peak which simultaneously shifts towards higher energies. The enhancement is relative to all other features, and intensity is not redistributed from any specific part of the spectrum.
To address the role of dynamics the corresponding comparison of the spectra of 5 vol% H_2O in acetonitrile, with the spectra of the 95 vol% H_2O liquid is made (see figure 6.16). Also in this case an enhancement of the d_2 feature relative to all other features and a slight high-energy shift is observed. The magnitude of this effect is similar for D_2O and H_2O, and it can be therefore concluded that d_2 increases in intensity with increased hydrogen bond coordination relative to all other features, almost independently of the nuclear dynamics.
It is expected that the 5 vol% H_2O and 5 vol% D_2O solutions have rather similar and low hydrogen bond coordination, and that the major difference is due to the faster nuclear dynamics as the deuterium atoms are replaced with hydrogen. Under this assumption one can observe (see figure 6.17) that faster nuclear dynamics have a similar effect on the XE spectra as increased hydrogen bond coordination: intensity piles up in the d_2 region. However, a marked difference from the effect of increased hydrogen bond coordination is that in this case the sharp $1b_1$ peak significantly drops in relative intensity, as does to some extent also intensity in the $3a_1$ region. The principal influence of the dynamics can accordingly be

described as a redistribution of intensity from close-lying energy regions to d_2. This intensity redistribution is very similar in the case when the spectra of neat H_2O and D_2O are compared (figure 6.18). It can therefore be concluded that there is a redistribution of intensity primarily from the $1b_1$ and $3a_1$ regions to the d_2 feature due to nuclear dynamics, which is not much influenced by the hydrogen bond coordination. In the following possible physical origins of the d_2 feature are discussed, considering experimental results based on other spectroscopic techniques. The XE transitions take place between states which are final states of the photoemission (PE) process, and the interpretations of the results of the different methods must be consistent. In valence PE spectroscopy of H_2O as well as D_2O emission from the $3a_1$ orbital is significantly broadened in the liquid, compared to the gas-phase. The broadening is reminiscent of the Davydov splitting in ice, and has been fitted with two peaks 1.3-1.5 eV apart, [91, 126] corresponding to bonding and anti-bonding interactions with the surrounding molecules. The PE spectra constitute clear evidence that the $3a_1$ orbital is mostly affected by condensation, and within state-of-the-art experimental accuracy the PE spectra of H_2O and D_2O are very similar. [91, 119] It would be tempting to assign the XE structures in this energy to changes in the $3a_1$ orbital under hydrogen bond influence.

The phenomenology is, however, different in XE and PE. In PE the high-energy anti-bonding partner of the $3a_1$-derived double feature peak is situated 1.7 eV from the $1b_1$ peak, whereas the distance from the $1b_1$ peak to the d_2 feature here is only around 1.1 eV. Furthermore, this interpretation does not comply with the phenomenology when hydrogen bond coordination increases. With increasing hydrogen bond interaction one would expect a broadening/splitting of a $3a_1$ feature rather than a relative increase of the high-energy component.

The "two-motif interpretation" [116, 117] assumes that intensity in the XE spectrum of liquid water in the region of the d_2 feature is due to emission from the $1b_1$ orbital of highly coordinated molecules, whereas the main part of the spectrum is due to less coordinated molecules. According to this interpretation, a large shift of the core level associated with hydrogen bond formation gives rise to a correspondingly shifted XE spectrum. Thus, one would expect that not only the d_2 feature but a full shifted XE spectrum grows as the hydrogen bonds are switched on. When comparing spectra of 5 vol% D_2O and pure D_2O such a behavior is, however, not observed. The superposition of a low-energy shifted XE spectrum would imply, e.g., an enhancement of the low-energy flank of the $1b_2$ peak accompanying the growth of the d_2 feature. In contrast a slight intensity increase on the high-energy flank is observed. Thus, the two-motif interpretation in this simple form is not supported by the present observations. It is consistent with the present data only if it can

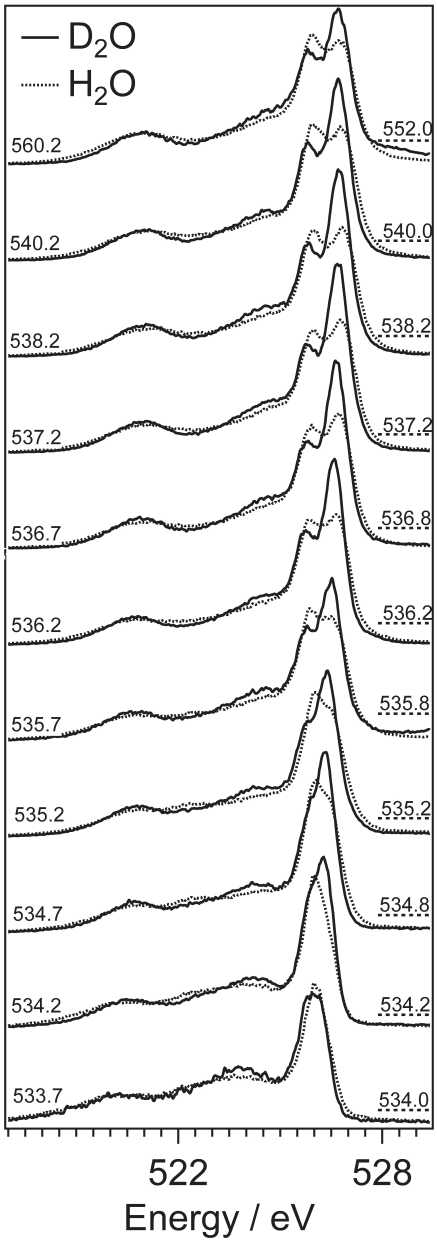

Figure 6.18.: K-edge X-ray absorption spectra of pure D_2O and D_2O-acetonitrile mixtures. For comparison the respective spectra of H_2O-acetonitrile mixtures are shown in dotted line.

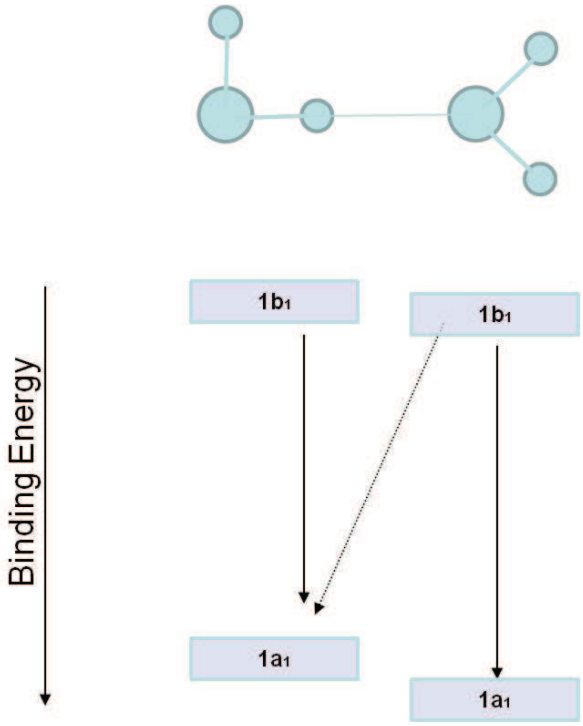

Figure 6.19.: Schematic explaining the low energy shift of the CT feature in the emission spectra of water.

be assumed that the XE spectrum of the coordinated molecules is very different from the spectrum of the less coordinated molecules.

In liquid water the PE peaks assigned to the $1a_1$ core level and the $1b_1$ lone-pair states are broad (FWHM 1.6 eV and 1.4 eV, respectively [91, 119]) and rather structure-less, whereas the XE transition between the two states shows much sharper features. Assuming that the core level PE width originates in emission from a superposition of emission from various molecules shifted due to different hydrogen bond conformations, [1] the narrowness in the XE spectrum could be understood if the shift of the $1b_1$ level due to interaction with the surrounding would be similar as the core level shift. Indeed, the core-level binding energy of the two states both decreases upon condensation albeit with different magnitudes, 1.9 eV for the core level and 1.4 eV for the $1b_1$. [91, 119] Therefore it is assumed that shifts due to increased coordination partially cancel, and that this is the principal reason for the observation of narrower $1b_1$ structures in XE than in PE spectra. Neglecting differences in excitation dynamics between PE and XE one would expect a low-energy shift of 0.5 eV in XE going from gas-phase to liquid, which is not far from the observed 0.3 eV. [117] A low-energy feature assigned to $1b_1$ states requires an additional XE shift of more than 0.7 eV. Such a shift does not contradict the PE results because it can be accommodated in the

broad PE peaks. A sharp $1b_1$ low-energy partner does require, however, that the shifts of the $1a_1$ and $1b_1$ levels are very different from the shifts leading to the main $1b_1$ peak associated with less coordinated molecules. In this case a low-energy shift of the core-level binding energy would not be accompanied by a corresponding $1b_1$ shift, but possibly the $1b_1$ binding energy may even shift in the opposite direction. For the "two-motif" interpretation this is still possible as the influence of the surrounding on the $1b_1$ and $1a_1$ may have substantially different character.
As an alternative one can consider that the observed behavior is to be expected beyond the one-center intensity model, [76, 81] which is most often used in the interpretation of XE spectra of complex systems like liquids. If "cross transitions" were prominent (see for illustration figure 6.19) one would expect a low-energy shift for transitions from core hole states of molecules with high hydrogen bond coordination or acceptor bonds broken (low BE) to $1b_1$ hole states on molecules with low coordination or donor bonds broken (high BE). [125] Such an interpretation would explain a $1b_1$ low-energy partner, and is in general consistent both with the observed XE and PE phenomenology. Since the first observation of cross transitions [119] their nature have been debated [1, 102] and it has been argued that a degree of covalency is required to generate appreciable intensity. The intensity of cross transitions is difficult to assess beyond the one-center intensity approximation, especially in the case of a fluctuating hydrogen bonding liquid, and hopefully the here presented suggestion will generate renewed theoretical interest.
The isotope effect consists primarily of a redistribution of intensity from the $1b_1$ and $3a_1$ peaks towards the d_2 region, and the present result shows that this redistribution occurs also when the hydrogen bond influence is reduced in the acetonitrile solution. The major spectral differences induced by substitution are due to the difference in nuclear dynamics, and for the pure substances there have been major efforts to predict the spectra based on semi-classical models of the nuclear movement during the core hole lifetime. [73,93,117] One pertinent question in this context concerns how far the nuclei move before the decay, and it has been pointed out that intensity corresponding to the "$1b_1$" low-energy partner almost coincides in energy with the expected intensity from dissociation fragments, [44] suggesting dissociation prior to emission. This interpretation is, however, not supported by simulations. Simulations differ in assigning $1b_1$ [88] or $3a_1$ [93] character to the 525.6-eV feature. The present observation suggests that intensity is dynamically redistributed to this region from both $1b_1$ and $3a_1$ states.
This complex problem is notoriously difficult to treat using proper quantum mechanical theory. In time-independent Kramers-Heisenberg scattering formalism the nuclear wavepacket development is reflected in lifetime-vibrational interference, most readily demonstrated for diatomic molecules.

[85, 103] Recently, the dynamics of the hydrogen bonded proton in the water dimer has been treated in this way, demonstrating an isotope-dependent redistribution of intensity from the high-energy $1b_1$ feature towards lower energies [73], a trend in line with observations. Although a quantum mechanical treatment is certainly called for, it remains to see to what extent the calculations of the simple model system is relevant for the liquid phase. In a dipolar liquid, one expects that the interaction with the surrounding molecules intrinsically smear out any vibrational fine structure for electronically excited states. [112] In the condensed phase the spectral consequences of dissipation of vibrational energy have been discussed over the years, [2, 21, 75, 92] and any counterpart to phonon damping [75] in the liquid will lead to an apparent loss of coherence and limit the applicability of a local Kramers-Heisenberg treatment.

6.4.4. Conclusion

A comparison of XE spectra of liquid H_2O and D_2O, in their pure form and as solutes in acetonitrile allows to identify and separate two distinctly different effects. First, one distinct spectral feature grows when hydrogen bond coordination increases, rather independent of nuclear dynamics. Second, a redistribution of intensity from the peak associated with the $1b_1$ and $3a_1$ orbitals to the energy region of the hydrogen bonding feature is observed when nuclear dynamics become faster, rather independent of the hydrogen bond coordination. The consequences for current interpretations of the XE spectra of liquid water are briefly discussed, and hopefully the here presented results will inspire theoretical developments.

6.5. Shared Solvation of Na^+ Ions in Water-Alcohol Mixtures

Lange et al., Physical Chemistry Chemical Physics 13, 34, pp 15423-15427 (2011) Reproduced by permission of the PCCP Owner Societies
http://dx.doi.org/10.1039/c1cp20527g

6.5.1. Introduction

Ion solvation and the driving forces behind it have been the focus of a wide range of investigations. [12, 20, 29, 128] Whereas a large number of datasets exists describing the macroscopic, thermodynamic behaviour of ion-solutions, [59] microscopic pictures of the electronic structures around the ions are rather scarce. For the macroscopic scale a helpful and commonly used measure for describing solvation is the medium effect of the solvent. It stands for the change in the total solvation energy of a solute upon transfer from one solvent to another. [59] This Gibbs energy of transfer (ΔG) can be determined experimentally via solubility, voltametry or potentiometry measurements for electroneutral combinations of ions. Note that it is not possible to determine ΔG experimentally for a single ion, for this a decomposition model has to be employed. Using theoretical calculations these information can reveal the relevance of specific parameters governing the solvation process, such as polarizability or ion and solvent size. [34, 58, 77, 100] Substantial discrepancies between theoretical predictions and experimental findings were observed concerning the excess free energy of solvation (ΔG_{exe}) of Na^+ ions in water-alcohol mixtures. [61] A positive excess free energy of solvation (2.6 kJ mol^{-1}) for Na^+ ions in binary mixtures of water-methanol (1:1) was derived from experimental results based on the tetraphenylarsonium tetraphenylborate (TATB) assumption, while for Na^+ ions in water-ethanol (1:1) a negative value (-2.25 kJ mol^{-1}) is found. [59,61] Theoretical calculations based on mean spherical approximation (MSA) however predicted for both cases a negative value. In this work the electronic structure of the Na^+ ions in these solvent-mixtures is investigated and differences in the probability for methanol and ethanol to occupy the first solvation shell are revealed. This observation allows to explain the differing excess free energy of solvation values for the binary mixtures. Further, the capability of theoretical models to predict this solvation behaviour is discussed.
The recent developments of spectroscopic techniques allow discovering the microscopic basis for the specific thermal behaviour of mixed solutions under real conditions. Such was done, e.g., by Dixit *et al.*, showing via neutron diffraction that water prevails in the form of strings or clusters

in alcohol solution. [33] Guo *et al.* came to the same conclusion based on X-ray absorption (XA) measurements at a synchrotron light source. [49] According to these studies the anomalous thermodynamic behaviour of water-alcohol mixtures is explained. Here, soft XAS at the sodium K-edge is used to systematically study sodium halides soluted in water and in low-order alcohols such as methanol and ethanol, as well as in the corresponding two-component solvents. This method is particularly suitable to reveal the microscopic details of the ion solvation shell due to its high sensitivity on the geometry of the electronic orbital structure.

6.5.2. Samples and Experimental Methods

The XA measurements of the sodium K-edge were performed at the U41 PGM beamline of the BESSY II 3rd generation synchrotron light source. The liquid samples were circulated with a flow of 1 l/min through a flow cell (made of stainless steel), directly behind a 150 nm thick Si_3N_4 membrane window allowing the irradiation by soft X-rays. The sodium K-edge spectra were measured with a resolution of 200 meV. Due to the soft X-ray attenuation length in the liquids in the range of a few micrometers, the detection was primarily bulk sensitive and surface effects were neglected. The absorption spectra were recorded in the total fluorescence yield mode using a 25 mm^2 GaAsP photodiode (type Hamamatsu G1127-04). The diode was mounted in a distance of around 4 mm from the membrane window and with an angle of 45° relative to the X-ray beam. The solutions measured were, nominally 1 M NaI dissolved in water, in ethanol, and in methanol. Due to the low solubility of NaI in propanol, a lower actual concentration of 0.1775 M NaI was chosen for this measurement. For comparison, also the spectra of 1 M NaBr in water, in ethanol and in methanol were recorded. Between measurements of different solutions, the flow cell was cleaned by flushing it with deionized water. To avoid uncertainties in the electrolyte concentration, the cell was rinsed once with the solution to be measured before each measurement. The setup allows probing the solutions as a function of irradiation time. Therefore, each sample was circulated several times through the flow cell and was measured in fixed time intervals. For a single spectrum the data collection time was 251 seconds. In order to increase the effect of the X-ray on the liquid, the cell was continuously irradiated between the measurements as well, thus giving the respective direct X-ray irradiation time dependence. As will be presented in the section of the Results and Discussion, changes in the electronic structure were observed for Na^+ ions in some of the solvents. In order to test whether these changes were due to other chemical changes in the solution, specifically the influence of I_2 and O_2 was examined. It is well known that I^- can be oxidized in alcohol forming

I_2. This influence was specifically investigated by adding different percentages (5-30 %) of fresh I_2 solution to the solutions of NaI in methanol and in ethanol and by measuring the XA spectra of the samples flown behind a membrane. The resulting spectra resemble the fresh spectra presented in figure 6.20, showing that the observed spectral changes cannot be explained by a formation of I_2 molecules upon irradiation. In order to exclude further possible oxidation effects due to the presence of dissolved O_2, also recorded XA spectra of the solutions were recorded after flushing them with O_2 gas for an hour. Again, the obtained spectra provided no evidence for an effect of the O_2 molecules on the Na^+ ions in alcohols. It was further tested whether the photochemical effect can also be induced by visible light. Therefore the XA spectra of NaI in methanol and ethanol were measured after exposing the solutions to visible light, in the energy range of 2 to 3 eV. Once more, the spectra obtained after irradiation with visible light resemble those from the fresh samples presented in figure 6.20. Accordingly, the photochemical reaction is induced by higher energy photons, such as soft X-rays. In addition, by varying the excitation energy within an extended range from 550 eV (the limit of the beamline harmonic) up to 1095 eV it was checked if the photochemical process was resonant for the Na K-edge and whether the observed spectral changes were induced also by lower energy X-ray photons.

6.5.3. Results and Discussion

In figure 6.20a the Na K-edge spectra of NaI in pure water and in pure methanol are shown in comparison to a 1:1 mixed solution of water and methanol. The characteristic spectral features of the Na^+ ion in the pure solvents have been explained previously. [5] Briefly, for water they consist of a pre-edge peak at 1071.8 eV, a main edge peak at approximately 1075 eV, and a post-edge peak at 1080 eV. Upon solution in different alcohols characteristic changes of these features are observed, fingerprinting the different geometries of the solvation shell of the Na^+ ions. The second and the third peak are shifted to lower energies, and the second peak appears sharper in the spectrum of Na^+ in methanol, as compared to water. In the water-methanol mixture, however, the spectrum shows an intermediate profile between those in water and in methanol. Such behavior is also observed for the 1:1 mixture of water and ethanol, as shown in figure 6.20b, as well as for the 1:1 methanol-ethanol mixture (figure 6.20c: the spectra of the ions in the solvent-mixtures have an intermediate profile between those of the respective pure solvents. However, in both latter cases, the intermediate profile shows a clear tendency towards one of the pure solvent spectra, i.e., towards the pure water (b) and the pure methanol (c), respectively. In the water-methanol case (a), though,

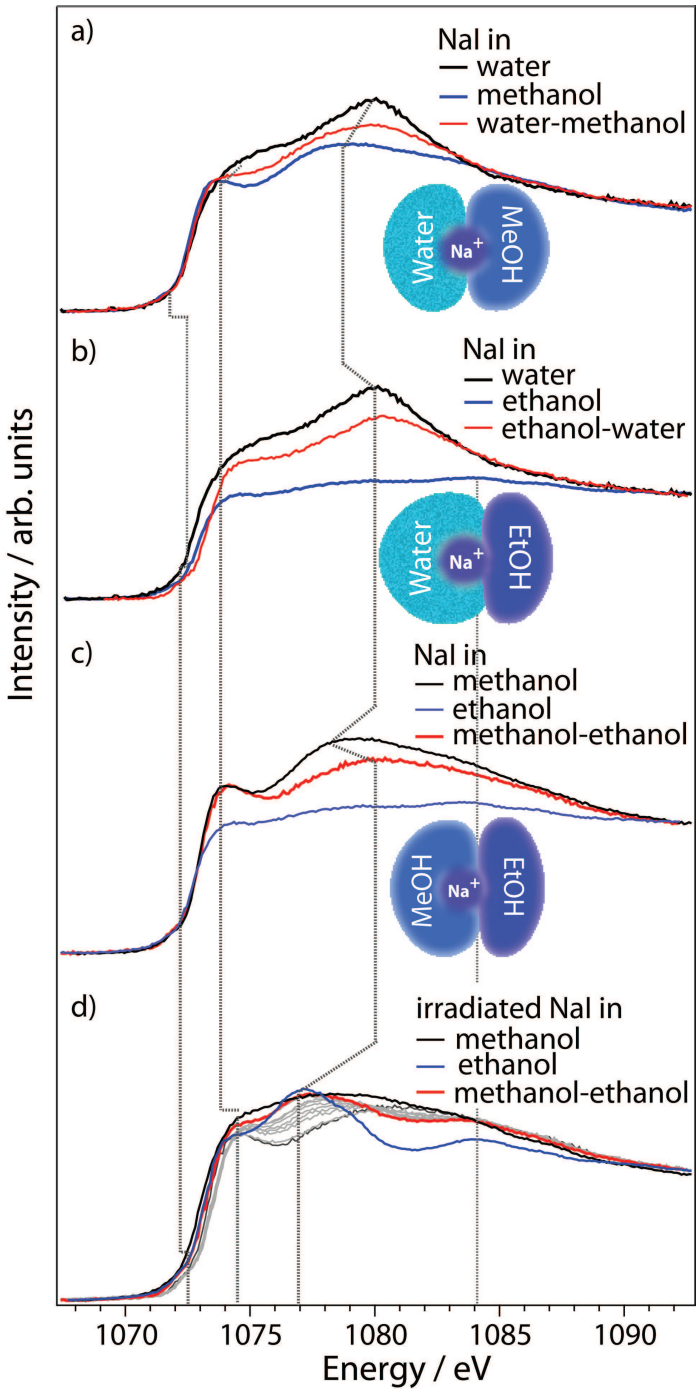

Figure 6.20.: Na K-edge soft XA spectra of NaI in different pure and binary solvent mixtures of water and alcohol. The observed spectral changes upon irradiation are shown in grey as a function of time. [64]

	Ethanol	Water : Ethanol 1:1	Methanol	Water : Methanol 1:1
ΔG [ion/kJ mol^{-1}]	14.9	5.2	7.0	6.1
ΔG_{exe} [ion/kJ mol^{-1}]		-2.25		2.6

Table 6.1.: Standard molar Gibbs energies of transfer of Na^+ cations from water to the respective alcohols or binary mixtures (taken from reference [59]). The ΔG_{exe} values were calculated according to 6.1

the profile is in the midrange between the two solvent components. Accordingly, the density of states (DOS) for the Na^+ ions in the mixtures is characteristically different from that in the pure solvents. Based on the assumption that the DOS is linearly correlated to the coordination number of the soluted species, one can conclude for the water-methanol mixture a 1:1 shared solvation shell. Na^+ ions in water or in alcohol solution have predominantly 6 hydration ligands. [10] Accordingly, the solvation shell in the water-methanol mixture is formed by three water and three methanol molecules. In the same way, for water and ethanol the spectra indicate that predominantly the first hydration shell of the Na^+ ion is composed of water and ethanol in a ratio of four water and two ethanol molecules. The same picture of a shared solvation shell can be assumed also for the methanol-ethanol mixtures, consisting of four methanol and two ethanol molecules. These findings provide a microscopic picture of the ion solution in the mixed water-alcohol solvents. In the following these microscopic picture will be correlated to the previous thermodynamic results. It will allow to understand why the excess free energy of solvation ΔG_{exe} gives a positive value for water-methanol mixtures, whereas the water-ethanol mixtures give a negative value. The excess free energy is defined as follows: [25, 80]

$$\Delta G_{exe}(x) = \Delta G(x) - [(1-x)\Delta G(x=0) + x\Delta G(x=1)] \qquad (6.1)$$

It represents the deviation in free energy of solvation ΔG for an ion at a given mole fraction x (in this case 0.5) in a binary mixture from the sum of the mole fraction weighted free energies of solvation in the pure components. It is supposed to represent better the extent of nonideality of a system. [61] In Table 6.1 the standard molar Gibbs energies of transfer for Na^+ ions from water to ethanol, methanol, and the respective binary mixtures of water are shown, taken from reference [59] These numbers show directly that a transfer of Na^+ to methanol is energetically favourable compared to a transfer to ethanol. For the binary mixtures with water however, a transfer to the ethanol containing mixture is advantageous. The results presented above can now explain this behaviour. Whereas for the water-methanol mixture both solvents partic-

ipate equally in the formation of the solvation shell around the Na^+, in the water-ethanol mixture, the ethanol contributes less to the solvation shell. The Na^+ ions energetically prefer to be surrounded by a higher number of water molecules which leads to a lower energy of transfer. Note that a direct comparison of ΔG_{exe} for the water-ethanol and water-methanol binary mixtures could misleadingly indicate that ethanol would be the solvent favoured by the Na^+ ions, which was here disproved. The MSA theory used for predicting the ΔG_{exe} values above takes the dipole moments, the solvent-solvent and ion-solvent size ratio into account. This parameter choice would imply a similar solvation shell structure around the Na^+ ions for water-methanol as for water-ethanol mixtures, since the diameters and the dipole moments of methanol and ethanol are quite similar compared to the water molecule. [12] This predicted picture however differs from the here experimentally determined one of the solvation shell. The scaled particle theory (SPT) approach allows taking the group contribution of the solvents into account. [123] According to this theory the additional methylene group (CH_2) leads to a lower probability for the ethanol molecule to be in the first solvation shell of the Na^+ ions than the methanol molecule. Also the quasi-lattice, quasi-chemical theory of preferential solvation proposes that the first solvation shell of ions in solution rather contains smaller solvent molecules than larger ones. [78] These theories substantiate distinct differences in the ion solvation by methanol as compared to ethanol solvents. They are in good agreement with the here presented data for the water-ethanol, as well as for the methanol-ethanol mixture. On the other hand, they suggest a prevalence of water in the first solvation shell. Accordingly, these theories do not agree with the XA results for the water- methanol mixture. Particularly for water-alcohol solutions, specific interactions such as hydrogen bonding and hydrophobic forces between the solvent molecules have a significant effect on the process of ion solvation. [61] These interactions can easily overcome nonspecific parameters such as size ratios and dipole interactions comprised by MSA, thus suddenly changing the balance of the involved forces. Indeed, mass spectroscopy measurements revealed that H^+ ions in small clusters of water-alcohol mixtures are more likely to bind to alcohol than to water, whereas with increasing cluster size the ions tend to be surrounded by water, [110] highlighting the importance of specific interactions. It is assumed here that the hydrogen bond network formed between the water and the alcohol, as well as between methanol and ethanol is a significant driving force for the solvation structure around ions and would thus be also a key parameter for the theoretical description of such systems. The reduction of the hydrogen bond interaction between water and methanol in the first solvation shell of the Na^+ ions could explain the thermodynamic non-ideal behaviour, which according to the presented measurements does not result from an unequally shared solvation. The evidence

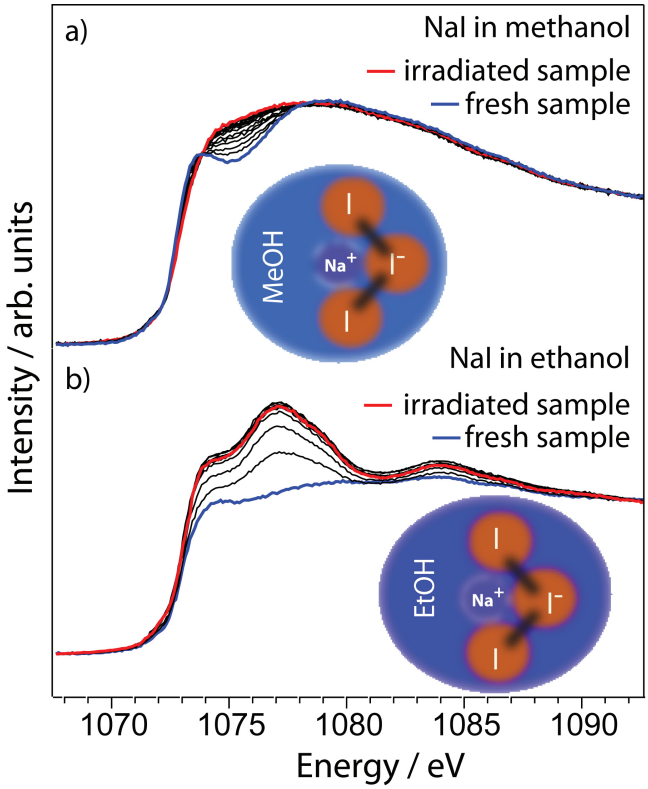

Figure 6.21.: Series of Na K-edge X-ray absorption spectra taken from NaI (a) in methanol, and (b) in ethanol. The spectra of the fresh samples are presented (blue), followed by the spectra monitoring the X-ray induced photochemical reaction. The spectrum of the irradiated sample (red) represents the final, stable state of the electronic structure of the Na^+ ions. Schematic drawings illustrate how the proposed chemical complex may cause the spectral changes. [64]

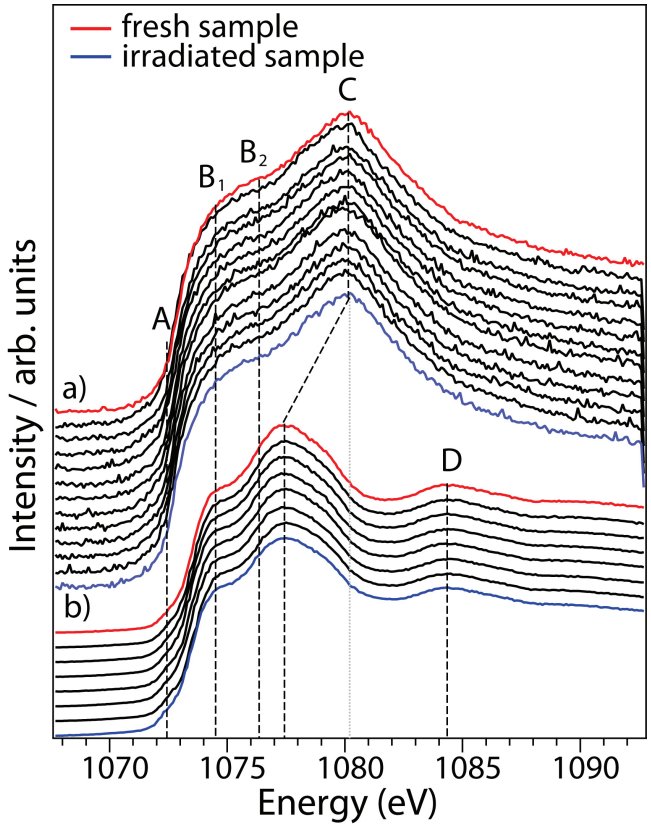

Figure 6.22.: Time dependent spectral measurement of NaI in a) water and b) propanol as solvents. The shape and positions of the peaks (A, B_1, B_2, C, D) are characteristic for each solvent. The spectral series of NaI and NaBr are displayed for increasing stages of irradiation, beginning with the spectra of the fresh samples (red). [64]

for a qualitatively different thermodynamic behaviour that is induced by small variations in the solvation structure highlights the importance of the specific interactions in the different water-alcohol mixtures. [61] This aspect receives further support from another finding shown in figure 6.20d). For NaI in the methanol-ethanol mixture, a change in the local electronic structure of the Na^+ ions was observed upon prolonged X-ray exposure. On the contrary, no such irradiation-induced changes could be observed for the water-alcohol mixtures. Note that the spectra shown in figure 6.20a-c) were obtained from freshly prepared solutions which were flown behind a Si_3N_4 membrane (speed of 1 liter per min), in order to ensure a constant renewal of the sample (every X-ray pulse measures a freshly introduced sample), while those presented in figure 6.20d) were measured without flowing. This solvent dependent effect of the irradiation on the electronic structure of the Na^+ ions was also found for the respective pure alcohol solvents, as shown in figure6.21a) and b). In the methanol solvent, changes in the spectral shape were observed for approximately 45 min-

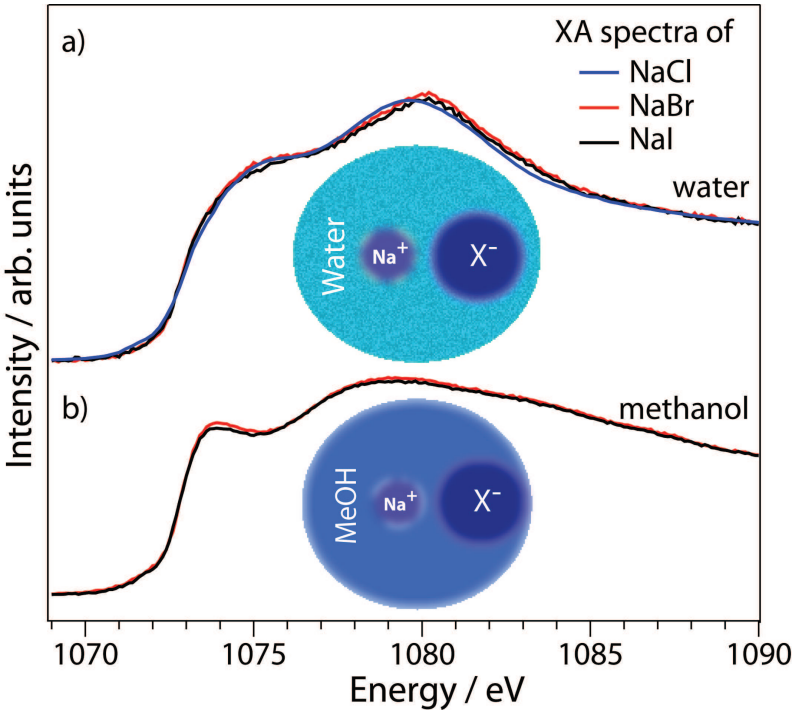

Figure 6.23.: Na K-edge X-ray absorption spectra of Na in a) water, and b) methanol, with different counter ions, respectively [64]

utes, whereas for NaI in ethanol stable spectra were obtained after just 15 minutes of irradiation. In propanol the irradiation causes an even faster changing within less than 7 minutes. Accordingly the spectra recorded in the closed-loop configuration (see figure 6.22b) do not show further time dependent changes. For NaI in pure water, however, the spectra of the irradiated sample resemble those of the fresh sample measured upon flowing, which confirms a stable hydration shell around the ions in water (see figure 6.22a). These findings suggest that specifically the presence of water molecules has a stabilizing function on the solvation shell around the Na^+ ions. For understanding this photochemical reaction complementary measurements were carried out. In situ mass spectroscopy confirmed that the observed changes are not due to chemical changes of the solvents (details about the mass spectroscopical measurements are presented in the appendix). Therefore it was investigated whether the photochemically induced changes are correlated to the charged counter anions coming in a direct interaction with the Na^+. The specific influence of the I^- was tested upon varying the counter ion of the Na^+ in different solvents as shown in figure 6.23. A substitution of the I^- by Cl^- and Br^- caused a small effect on the electronic structure of the Na^+ ions in water, as shown in figure 6.23a. Comparable small effects were observed in the spectra of Na^+ ions in methanol upon exchange of Br^- and I^- (see 6.23b.

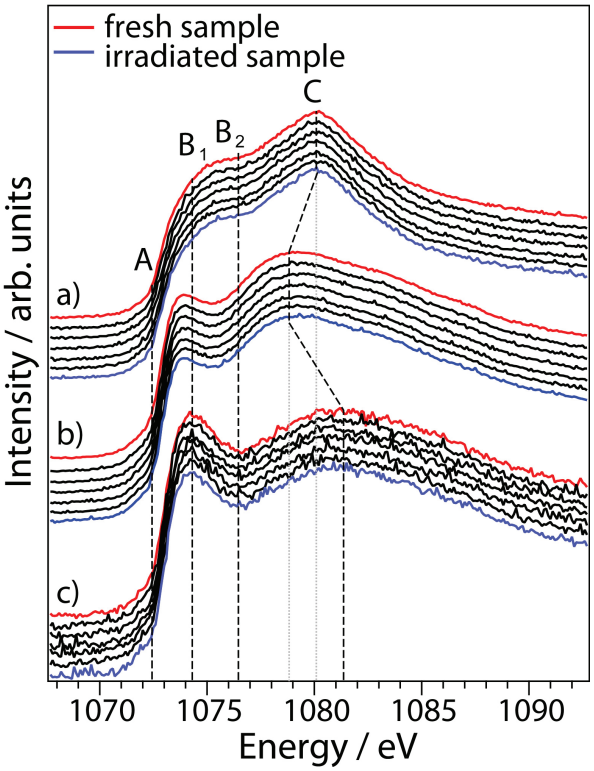

Figure 6.24.: Time dependent Na K-edge XA spectra of NaBr in a) water, b) methanol and c) ethanol as solvents. The shape and positions of the peaks (A, B_1, B_2, C, D) are characteristic for each solvent. The series of spectra of NaI and NaBr are displayed for increasing stages of irradiation, beginning with the spectra of the fresh samples (red). [64]

However, a significant photochemical changing was only observed for I^- as a counter ion, not for Cl^- or Br^- (see figure 6.24). On the basis of systematic testing, a possible side effect of I_2 formed from I^- by oxidation in the alcohols, as well as a potential influence of oxidation effects by the presence of dissolved O_2 could be excluded (see experimental section). On the other hand, it was shown that the photochemical reaction was induced by the soft X-ray photons, whereas visible light did not influence the spectra (see experimental section). It is concluded accordingly that in the NaI solutions the irradiation induced the formation of an I_3^- complex. Iodide ions can reach higher charge states than any other halide after core excitation and Auger decay (see figure A.6 in the appendix). These excited iodide ions are highly reactive and may readily form I_3^- complexes, which will affect the local electronic structure of the Na^+ ions upon pairing with them in the solution, as illustrated by a schematic picture in figure 6.23. For the formation of such a paired-ion complex, the relation of the competing solvent-solvent hydrogen bonding and the solvent-solute dipole interactions are essential. In the cases where water is involved as

a solvent, the dipole-mediated association of the water molecules with the Na^+ ions is stronger than the solvent- solvent hydrogen bonds, thus stabilizing the solvation structure around the Na^+ ions against a close interaction with the counterions. This mechanism works even if there are only few water molecules in close interaction with the Na^+ ions, as it is the case for alcohol-water mixtures. Furthermore, in water containing solvents, the Coulomb potential of the ions can be effectively screened by the high dielectric constant of the water. [14] In the pure alcoholic solvents, however, the weaker dipole interaction with the Na^+ ions allows a replacement of alcohol molecules in the solvation shell by I_3^- and the formation of paired-ion complexes. From the respective irradiation times required for this process (methanol: 45 min, ethanol: 15 min, propanol: > 7 min), the relative strength of the dipole interaction between the Na^+ and the alcohol (D_x) can be assessed as $D_{methanol} > D_{ethanol} > D_{propanol}$.

6.5.4. Conclusion

In summary, a microscopic explanation for the different values of the excess free energy of solvation for Na^+ ions in a water-methanol mixture, compared to a water-ethanol mixture was presented. This explanation is based on the structural differences of the shared solvation shell around the Na^+ ions in these solvent systems. As one key for the differing thermal behaviour of the ions in the different water-alcohol mixtures, hydrogen bond interactions are proposed, which are not yet implemented in the discussed theoretical approaches. This finding emphasizes the importance of specific interactions in the solvation of ions in binary mixtures of water and less polar media, thus providing the experimental basis for an accurate understanding of these processes. This picture receives further support from the observation that specifically the water stabilizes as a component the structure of the solvation shell around the Na^+ ions by its strong dipole interaction. By contrast, for NaI in alcohol solvents the photochemically induced formation of ionic complexes has a significant effect on the electronic structure of the sodium ions. These results are important for the fundamental picture of ion solvation, as well as for technological applications, since many thermodynamic properties of electrolyte solutions in binary polar mixtures depend on the partial polarization of the constituent solvents.

7. Summary

In the framework of this thesis a novel setup for soft X-ray absorption and emission spectroscopy on liquid samples, the LiXEdrom, was built and developed. [66] This setup allows membrane-free measurements on a liquid micro-jet. X-ray absorption measurements can be carried out in total fluorescence yield using a photodiode. High resolution X-ray emission spectra can be detected in Rowland-geometry using a MCP-CCD detection unit. The four gratings of the spectrometer, that are arranged on a rotable holder, cover an energy range from 20-1000 eV.
Proof of principle measurements were carried out on pure water. These were the first high resolution XE spectra that were obtained from a membrane free setup. The spectra show a double-peak structure in the region of the $1b_1$ molecular orbital, proving that this splitting is not correlated to membrane induced artifacts. [66]
The origin of the splitting was systematically further investigated in the framework of this thesis. By diluting water in acetonitrile the number of hydrogen bonds per water molecules is significantly reduced. FT-IR spectroscopy was used to monitor these changes of the hydrogen bonding for varying water concentrations in water-acetonitrile mixtures. [65] The behavior was compared to water-mixtures with other organic solvents which differ from acetonitrile concerning the polarity and the hydrophobicity. For the water-acetonitrile mixture it was shown that for a concentration of up to 1 % of water, the water molecules are isolated within the acetonitrile. Upon increasing water concentration the molecules begin to cluster. In the XA spectra, the reduction of hydrogen bond coordination leads to spectra that resemble the spectra of gas-phase. [67] The peaks show a significant sharpening. Condensation effects are however still present causing a blue-shift of the spectra of the isolated water molecules compared to the ones of gas-phase water. In the emission spectra, the decreasing hydrogen bond coordination only had significant effects on one spectral feature: the low-energy $1b_1$ peak. It decreases with decreasing hydrogen bond coordination. The difference spectra for varying water concentration show that the main changes observed cannot be explained by a simple decomposition approach, since this would require changes in several regions of the spectra. From the purely experimental observations, the low-energy $1b_1$ feature was identified as a sensor for the hydrogen bond coordination.

It is however well known, that the ratio between the two $1b_1$ features is also sensitive to isotopic changes. To separate these two effects from each other, the electronic structure of D_2O and D_2O-acetonitrile mixtures was investigated and compared the spectra to the previous results for H_2O. [68] In the XA spectra the dilution in acetonitrile lead to similar changes for D_2O as described before for H_2O. Concerning the XE spectra, the investigation showed that hydrogen bonding and isotopic effects can be clearly separated from each other. The experimental findings of these studies do not stand in clear agreement with the interpretations proposed until now [44, 116] concerning the origin of the $1b_1$ splitting. Therefore a mechanism of cross transitions among neighboring water molecules is proposed. Such cross transitions could explain the sensitivity of the spectra to the hydrogen bond environment, and they could explain, why only one region of the spectra is affected.
The special role of water for the thermodynamic properties of ionic solutions are addressed in this thesis as well. [64] Na^+ aqueous solutions with different counter anions in solvents with lower polarity than water were the model system in this thesis. The XA spectra allowed determining the occupancy of the first solvation shell around the ions. Whereas in water-methanol mixtures the hydration shell around Na^+ is equally shared between the two solvents, in water-ethanol mixtures the solvation shell is dominated by water molecules. This observation allowed understanding why, thermodynamically, the energy of transfer is lower for water-ethanol mixtures than for water-methanol mixtures. Furthermore for NaI solutions a photochemical process was observed, which only takes place in the alcohols solutions, but not in water and only with iodide as a counter ion. Based on further investigation including mass spectrometry it was proposed, that upon soft X-ray irradiation on NaI in alcohol solutions I_3^- is formed. In water, however, strong dipole interactions stabilize the solvation shell, preventing the interaction between the iodide ions.
Meanwhile the novel LiXEdrom spectrometer is also available for users of the BESSY II synchrotron facility. It was already employed for studies on various solvents, transition metals and complexes such as porphyrins in solution. Further development by the F-N1 group included the introduction of a flow-cell which allows now comparative studies between jet and flow-cell measurements. Also programs for measuring partial as well as inverse partial fluorescence yield with the MCP detector were developed. For the future, time-resolved experiments are planned, which allow studying the development of the occupied and unoccupied electronic states of liquids and samples in solution on the timescale of pico-seconds. This can be achieved upon combining a pico-second laser-pump with a pico-second soft X-ray probe signal from the synchrotron. Details about perspective studies can be found in reference [69].

A. Appendix

A.1. Gaussian03 Calculation of Gas Phase Water

	$1a_1$	$2a_1$	$1b_2$	$3a_1$	$1b_1$	$4a_1$	$2b_2$
O1s	0.99465	-0.20991	0.00000	-0.07343	0.00000	-0.09990	0.00000
O2s	0.02111	0.47609	0.00000	0.16517	0.00000	0.05837	0.00000
$O2p_x$	0.00000	0.00000	0.00000	0.00000	0.64002	0.00000	0.00000
$O2p_y$	0.00000	0.00000	0.50605	0.00000	0.00000	0.00000	-0.33336
$O2p_z$	-0.00133	-0.09108	0.00000	0.55302	0.00000	-0.22286	0.00000
O3s	0.00403	0.44393	0.00000	0.32478	0.00000	1.38734	0.00000
$O3p_x$	0.00000	0.00000	0.00000	0.00000	0.51105	0.00000	0.00000
$O3p_y$	0.00000	0.00000	0.30926	0.00000	0.00000	0.00000	-0.82616
$O3p_z$	0.00048	-0.05163	0.00000	0.40177	0.00000	-0.51348	0.00000
$H_1$1s	0.00034	0.12867	0.22937	-0.14267	0.00000	-0.05718	0.05377
$H_1$2s	-0.00019	0.00232	0.11472	-0.08871	0.00000	-1.02971	1.37246
$H_2$1s	0.00034	0.12867	-0.22937	-0.14267	0.00000	-0.05718	-0.05377
$H_2$2s	-0.00019	0.00232	-0.11472	-0.08871	0.00000	-1.02971	-1.37246

Figure A.1.: Atomic character of the molecular orbitals of an isolated water molecule calculated with the Gaussian03 program

A.2. Mass Spectroscopic Measurements

In order to investigate the X-ray induced photochemical reaction, which takes place only for NaI in alcohol, mass spectroscopy was performed for each sample before and after X-ray exposure. For this, gas chromatography/mass spectrometry (HP G1800 A GCD system, Agilent, Waldbronn) was used. 50 ml of the reaction mixture were placed in a sealed glass vial, and equilibrated to 50 °C for ten minutes. From the headspace, 0.5 l were injected onto a HP5-MS column (30 m, 0.25 mm) which was maintained at 25 °C for two minutes, then heated to 50 °C during the next minute. Hydrogen served as a carrier gas at a flow rate of 1 ml min^{-1} with an inlet temperature of 50 °C.
The total ion chromatograms (TIC) of the GCMS analyses (see figure A.2 of sample before irradiation with soft X-rays and figure A.3 of sample after irradiation show only one peak at 0.67 min arising from the neat solvent. At 0.56 min, the system peak is detected which indicates the void time of the system and which is also present in blank runs. No other peaks are detectable, indicating that the solvent is not affected by irradiation.

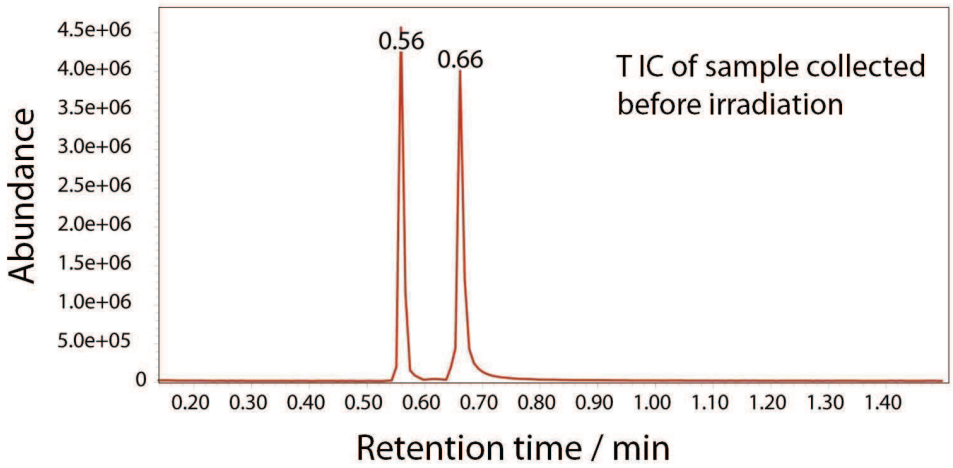

Figure A.2.: Total ion chromatogram (TIC) of NaI in alcohol solution before irradiation with soft X-rays [64]

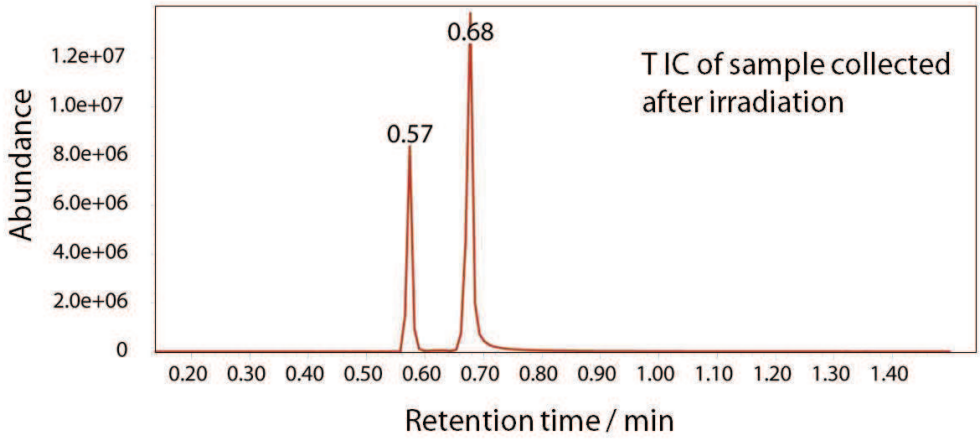

Figure A.3.: Total ion chromatogram (TIC) of NaI in alcohol solution after irradiation with soft X-rays [64]

A.3. Charge states

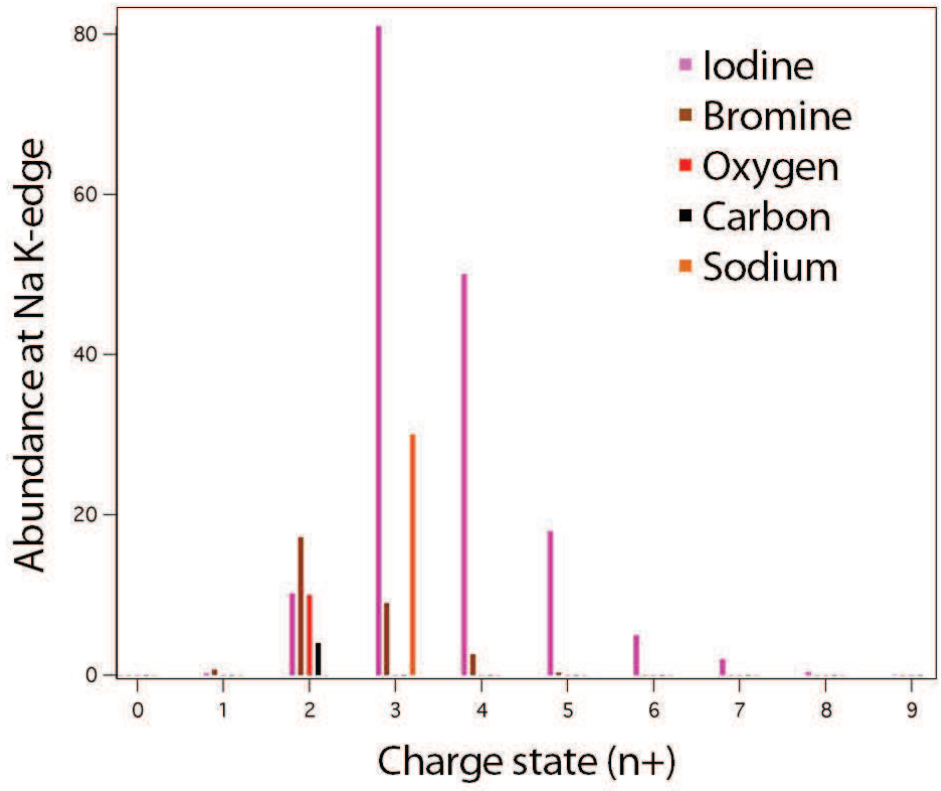

Figure A.4.: Charge states of iodine, bromine, oxygen, carbon and sodium at the sodium K-edge [64]

A.4. The LiXEdrom setup

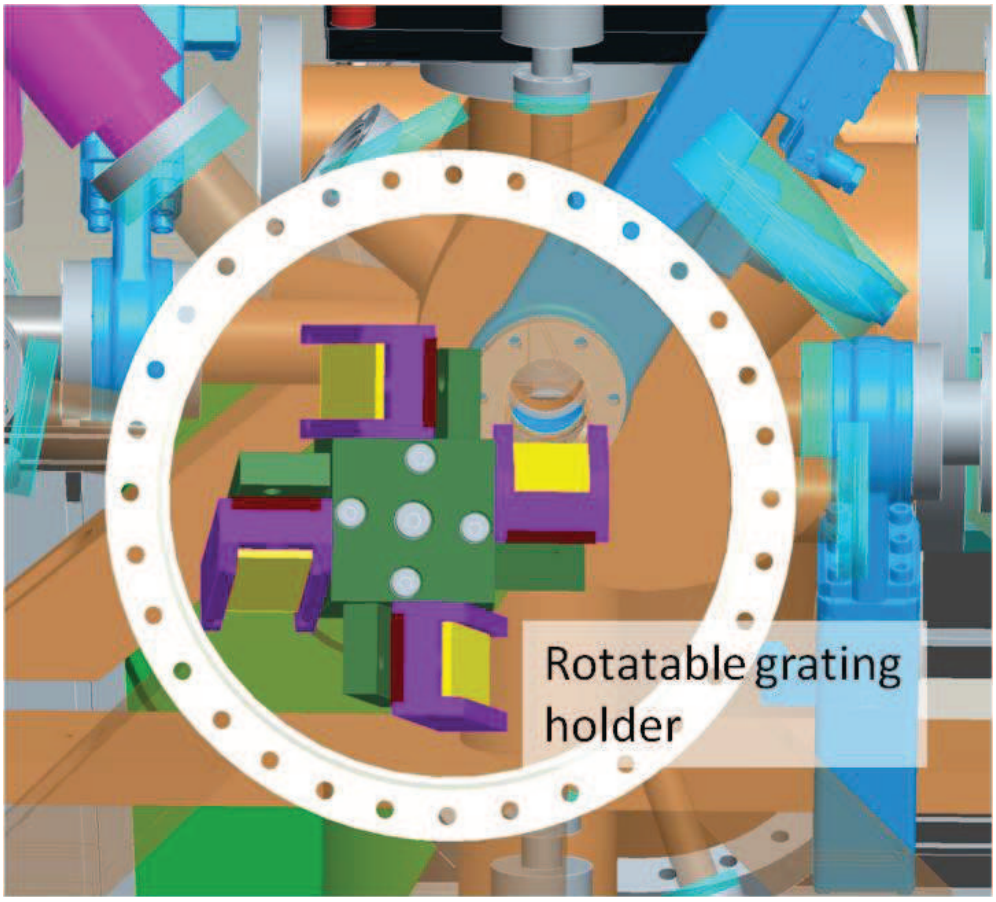

Figure A.5.: Grating chamber of the LiXEdrom setup containing the rotatable grating holder for four different gratings, covering an energy range from 20 eV to 1000 eV.

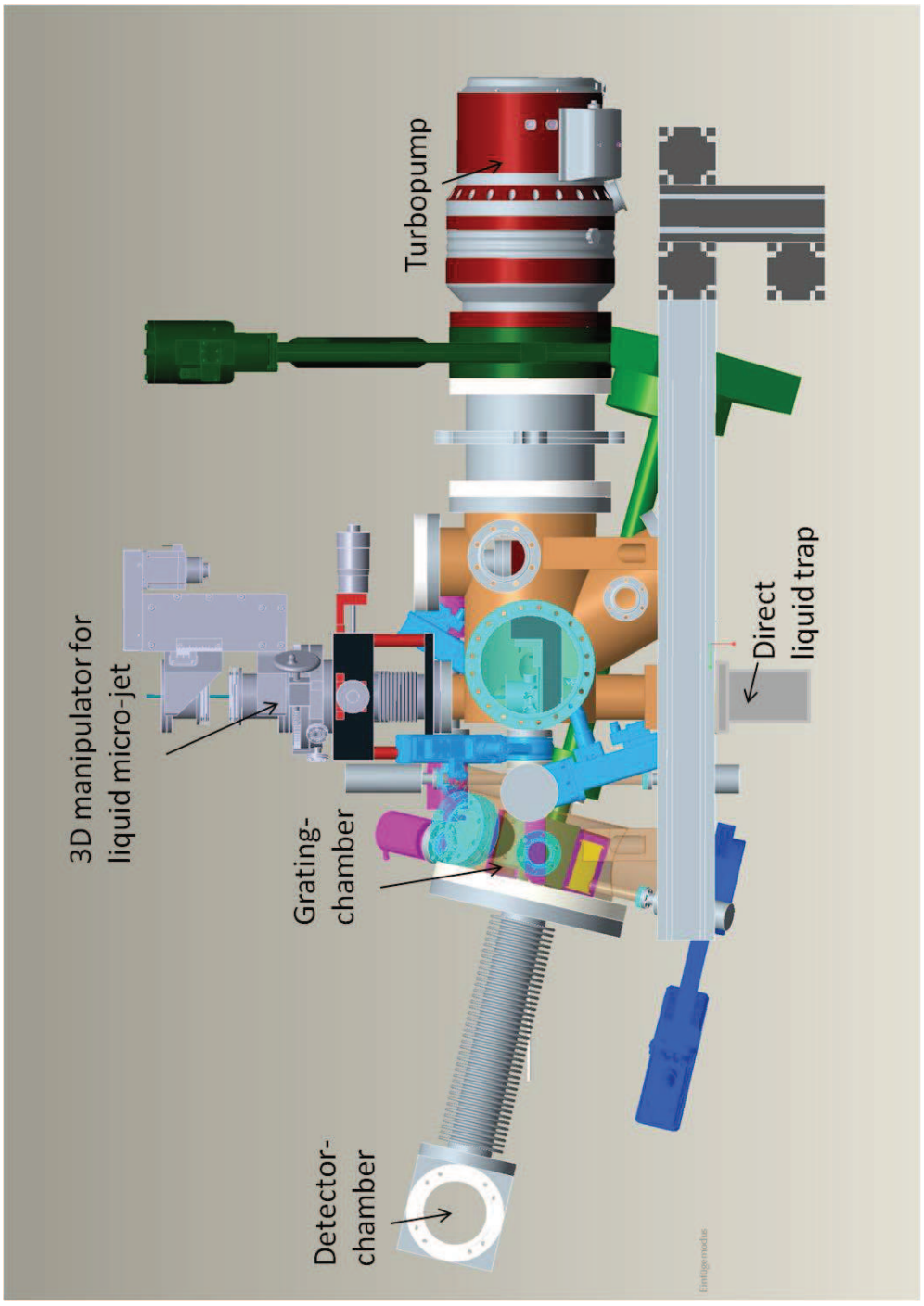

Figure A.6.: LiXEdrom setup sideview

Bibliography

[1] H. Adachi and K. Taniguchi. Discrete variational x-alpha cluster calculations .4. application to x-ray-emission study. *Journal of the Physical Society of Japan*, 49(5):1944–1953, 1980.

[2] C. O. Almbladh and A. L. Morales. Phonon effects on deep-level excitations in metals - beyond the linear-screening and linear-coupling models. *Journal of Physics F-Metal Physics*, 15(4):991–1012, 1985.

[3] D.T. Attwood. *Soft x-rays and extreme ultraviolet radiation: principles and applications*. Cambridge Univ Pr, 2000.

[4] J. L. Atwood, F. Hamada, K. D. Robinson, G. W. Orr, and R. L. Vincent. X-ray-diffraction evidence for aromatic pi hydrogen-bonding to water. *Nature*, 349(6311):683–684, 1991.

[5] E. F. Aziz. The solvation of ions and molecules probed via soft x-ray spectroscopies. *Journal of Electron Spectroscopy and Related Phenomena*, 177(2-3):168–180, 2010.

[6] E. F. Aziz, S. Eisebitt, F. de Groot, J. Chiou, C. Dong, J. Guo, and W. Eberhardt. Direct contact versus solvent-shared ion pairs in nicl2 electrolytes monitored by multiplet effects at ni(ii) l edge x-ray absorption. *J. Phys. Chem. B*, 111:4440–4445, 2007.

[7] E. F. Aziz, N. Ottosson, S. Bonhommeau, N. Bergmann, W. Eberhardt, and M. Chergui. Probing the electronic structure of the hemoglobin active center in physiological solutions. *Physical Review Letters*, 102(6), 2009.

[8] E. F. Aziz, N. Ottosson, S. Eisebitt, W. Eberhardt, B. Jagoda-Cwiklik, R. Vacha, P. Jungwirth, and B. Winter. Cation-specific interactions with carboxylate in amino acid and acetate aqueous solutions: X-ray absorption and ab initio calculations. *Journal of Physical Chemistry B*, 112(40):12567–12570, 2008.

[9] E. F. Aziz, M. H. Rittmann-Frank, K. M. Lange, S. Bonhommeau, and M. Chergui. Charge transfer to solvent identified using dark channel fluorescence-yield l-edge spectroscopy. *Nature Chemistry*,

2(10):853–857, 2010.

[10] E. F. Aziz, A. Zimina, M. Freiwald, S. Eisebitt, and W. Eberhardt. Molecular and electronic structure in nacl electrolytes of varying concentration: Identification of spectral fingerprints. *Journal of Chemical Physics*, 124(11), 2006.

[11] R. M. Badger and S. H. Bauer. Spectroscopic studies of the hydrogen bond. ii. the shift of the o-h vibrational frequency in the formation of the hydrogen bond. *The Journal of Chemical Physics*, 5(11):839, 1937.

[12] B. Bagchi and R. Biswas. Polar and nonpolar solvation dynamics, ion diffusion, and vibrational relaxation: Role of biphasic solvent response in chemical dynamics. *Advances in Chemical Physics, Vol 109*, 109:207–433, 1999.

[13] P. Ball. Water as an active constituent in cell biology. *Chemical Reviews*, 108(1):74–108, 2008.

[14] P. Ball. Water as an active constituent in cell biology. *Chemical Reviews*, 108(1):74–108, 2008.

[15] J. B. Bates. Fourier-transform infrared spectroscopy. *Science*, 191(4222):31–37, 1976. Ba930 Times Cited:18 Cited References Count:20.

[16] R.J. Bell. Introductory fourier transform spectroscopy. *London: Academic Press, 1972*, 1, 1972.

[17] N. Bergmann, S. Bonhommeau, K. M. Lange, S. M. Greil, S. Eisebitt, F. de Groot, M. Chergui, and E. F. Aziz. On the enzymatic activity of catalase: an iron l-edge x-ray absorption study of the active centre. *Physical Chemistry Chemical Physics*, 12(18):4827–4832, 2010.

[18] J. E. Bertie and Z. D. Lan. Liquid water-acetonitrile mixtures at 25 degrees c: The hydrogen-bonded structure studied through infrared absolute integrated absorption intensities. *Journal of Physical Chemistry B*, 101(20):4111–4119, 1997.

[19] M. Born. Volumen und hydratationswärme der ionen. *Zeitschrift für Physik*, 1(1), 1920.

[20] A. E. Bragg, M. C. Cavanagh, and B. J. Schwartz. Linear response breakdown in solvation dynamics induced by atomic electron-transfer reactions. *Science*, 321(5897):1817–1822, 2008.

[21] P. A. Bruhwiler, O. Karis, and N. Martensson. Charge-transfer dynamics studied using resonant core spectroscopies. *Reviews of Modern Physics*, 74(3):703–740, 2002.

[22] E. Burkel. *Erforschung der Dynamik kondensierter Materie mit Synchrotronstrahlung: Vorlesungsmanuskripte des WE-Heraeus-Ferienkurses für Physik vom 6. Bis 17. Oktober 1997 an der Universität Rostock. Vorlesungsmanuskripte*. Universität Rostock, Fachbereich Physik, 1997.

[23] Cohen-Tannoudji C., B. Diu, and F. Laloe. Quantenmechanik.

[24] A. Cesar, H. Ågren, and V. Carravetta. Vibronic emission from short-lived core-hole states - theory and applications for the water molecule. *Physical Review A*, 40(1):187–206, 1989.

[25] A. Chandra and B. Bagchi. Molecular theory of solvation and solvation dynamics in a binary dipolar liquid. *Journal of Chemical Physics*, 94(12):8367–8377, 1991.

[26] D.L.G. Cheung. *Structures and properties of liquid crystals and related molecules from computer simulation*. PhD thesis, PhD Thesis, Univ. Durham, Chemistry. http://portellen. phycmt. dur. ac. uk/sjc/thesis dlc/thesis. html, 2002.

[27] M. L. Clapp, R. E. Miller, and D. R. Worsnop. Frequency-dependent optical-constants of water ice obtained directly from aerosol extinction spectra. *Journal of Physical Chemistry*, 99(17):6317–6326, 1995.

[28] M.J. Costello, M. Coll, R. Danovaro, P. Halpin, H. Ojaveer, and P. Miloslavich. A census of marine biodiversity knowledge, resources, and future challenges. *PLoS One*, 5(8):e12110, 2010.

[29] C. J. Cramer and D. G. Truhlar. An scf solvation model for the hydrophobic effect and absolute free-energies of aqueous solvation. *Science*, 256(5054):213–217, 1992.

[30] D. Cringus, S. Yeremenko, M. S. Pshenichnikov, and D. A. Wiersma. Hydrogen bonding and vibrational energy relaxation in water-acetonitrile mixtures. *Journal of Physical Chemistry B*, 108(29):10376–10387, 2004.

[31] A. G. Császár, G. Czakó, T. Furtenbacher, J. Tennyson, V. Szalay, S. V. Shirin, N. F. Zobov, and O. L. Polyansky. On equilibrium structures of the water molecule. *Journal of Chemical Physics*,

122(21):214305, 2005.

[32] FMF De Groot, MA Arrio, P. Sainctavit, C. Cartier, and CT Chen. Fluorescence yield detection: Why it does not measure the x-ray absorption cross section. *Solid state communications*, 92(12):991–995, 1994.

[33] S. Dixit, J. Crain, W. C. K. Poon, J. L. Finney, and A. K. Soper. Molecular segregation observed in a concentrated alcohol-water solution. *Nature*, 416(6883):829–832, 2002.

[34] B. L. Eggimann and J. I. Siepmann. Size effects on the solvation of anions at the aqueous liquid-vapor interface. *Journal of Physical Chemistry C*, 112(1):210–218, 2008.

[35] S. Eisebitt, T. Boske, J. E. Rubensson, and W. Eberhardt. Determination of absorption-coefficients for concentrated samples by fluorescence detection. *Physical Review B*, 47(21):14103–14109, 1993.

[36] J. E. Enderby and G. W. Neilson. Water, a comprehensive treatise. *by F. Franks, Plenum Press, New York*, 6:1, 1979.

[37] M. Faubel, S. Schlemmer, and J. P. Toennies. A molecular-beam study of the evaporation of water from a liquid jet. *Zeitschrift Fur Physik D-Atoms Molecules and Clusters*, 10(2-3):269–277, 1988.

[38] M. Faubel, S. Schlemmer, and J. P. Toennies. A molecular-beam study of the evaporation of water from a liquid jet. *Zeitschrift Fur Physik D-Atoms Molecules and Clusters*, 10(2-3):269–277, 1988.

[39] M. Faubel, B. Steiner, and J. P. Toennies. Photoelectron spectroscopy of liquid water, some alcohols, and pure nonane in free micro jets. *Journal of Chemical Physics*, 106(22):9013–9031, 1997.

[40] J.B. Foresman, T.A. Keith, K.B. Wiberg, J. Snoonian, and M.J. Frisch. Solvent effects. 5. influence of cavity shape, truncation of electrostatics, and electron correlation on ab initio reaction field calculations. *The Journal of Physical Chemistry*, 100(40):16098–16104, 1996.

[41] HL Friedman and CV Krishnan. Water, a comprehensive treatise. *Vol*, 3:1, 1973.

[42] E. Frisch, M. Frisch, and G.W. Trucks. *Gaussian 03*. Gaussian, 2003.

[43] O. Fuchs, M. Zharnikov, L. Weinhardt, M. Blum, M. Weigand,

Y. Zubavichus, M. Bär, F. Maier, J. D. Denlinger, C. Heske, M. Grunze, and E. Umbach. Comment on "isotope and temperature effects in liquid water probed by x-ray absorption and resonant x-ray emission spectroscopy" - fuchs et al. reply. *Physical Review Letters*, 100(24):249802, 2008.

[44] O. Fuchs, M. Zharnikov, L. Weinhardt, M. Blum, M. Weigand, Y. Zubavichus, M. Bär, F. Maier, J. D. Denlinger, C. Heske, M. Grunze, and E. Umbach. Isotope and temperature effects in liquid water probed by x-ray absorption and resonant x-ray emission spectroscopy. *Physical Review Letters*, 100(2):027801, 2008.

[45] F. Gel'mukhanov and H. Ågren. Resonant x-ray raman scattering. *Physics reports*, 312(3):87–330, 1999.

[46] D. N. Glew and N. S. Rath. H2o, hdo, and ch3oh infrared spectra and correlation with solvent basicity and hydrogen bonding. *Canadian Journal of Chemistry*, 49(6):837, 1971.

[47] J. Grasjo, E. Andersson, J. Forsberg, L. Duda, E. Henke, W. Pokapanich, O. Bjorneholm, J. Andersson, A. Pietzsch, F. Hennies, and J. E. Rubensson. Local electronic structure of functional groups in glycine as anion, zwitterion, and cation in aqueous solution. *Journal of Physical Chemistry B*, 113(49):16002–16006, 2009.

[48] S. M. Greil, I. Lauermann, A. Ennaoui, T. Kropp, K. M. Lange, M. Weber, and E. F. Aziz. In situ investigation of wet chemical processes for chalcopyrite solar cells by l-edge xas under ambient conditions. *Nuclear Instruments and Methods in Physics Research Section B-Beam Interactions with Materials and Atoms*, 268(3-4):263–267, 2010.

[49] J. H. Guo, Y. Luo, A. Augustsson, S. Kashtanov, J. E. Rubensson, D. K. Shuh, H. Ågren, and J. Nordgren. Molecular structure of alcohol-water mixtures. *Physical Review Letters*, 91(15), 2003.

[50] J. H. Guo, Y. Luo, A. Augustsson, J. E. Rubensson, C. Såthe, H. Ågren, H. Siegbahn, and J. Nordgren. X-ray emission spectroscopy of hydrogen bonding and electronic structure of liquid water. *Physical Review Letters*, 89(13):137402, 2002.

[51] C. H. Hamann and W. Vielstich. Elektrochemie, 2005. 4. Auflage, Wiley VCH-Verlag, Weinheim.

[52] P. Hobza and Z. Havlas. Blue-shifting hydrogen bonds. *Chemical Reviews*, 100(11):4253–4264, 2000.

[53] N. D. Huang, D. Nordlund, C. C. Huang, U. Bergmann, T. M. Weiss, L. G. M. Pettersson, and A. Nilsson. X-ray raman scattering provides evidence for interfacial acetonitrile-water dipole interactions in aqueous solutions. *Journal of Chemical Physics*, 135(16), 2011.

[54] JH Hubbell, H.A. Gimm, and I. Øverbø. Pair, triplet, and total atomic cross sections (and mass attenuation coefficients) for 1 mev-100 gev photons in elements z= 1 to 100. *Journal of physical and chemical reference data*, 9:1023, 1980.

[55] G.A. Jeffrey and G.A. Jeffrey. *An introduction to hydrogen bonding*. Oxford University Press New York, 1997.

[56] Ch. Jung, F. Eggenstein, S. Hartlaub, R. Follath, J.S. Schmidt, F. Senf, M.R. Weiss, Th. Zeschke, and W. Gudat. First results of the soft x-ray microfocus beamline u41-pgm. *Nuclear Instruments and Methods in Physics Research Section A: Accelerators, Spectrometers, Detectors and Associated Equipment*, 467-468, Part 1(0):485–487, 2001.

[57] Ch. Jung, F. Eggenstein, S. Hartlaub, K. Holldack, R. Follath, M. Mast, J.-S. Schmidt, F. Senf, M. R. Weiss, and Zeschke Th. U41-pgm: commissioning results.

[58] P. Jungwirth and D. J. Tobias. Ions at the air/water interface. *Journal of Physical Chemistry B*, 106(25):6361–6373, 2002.

[59] C. Kalidas, G. Hefter, and Y. Marcus. Gibbs energies of transfer of cations from water to mixed aqueous organic solvents. *Chemical Reviews*, 100(3):819–852, 2000.

[60] S. Kashtanov, A. Augustsson, Y. Luo, J. H. Guo, C. Såthe, J. E. Rubensson, H. Siegbahn, J. Nordgren, and H. Ågren. Local structures of liquid water studied by x-ray emission spectroscopy. *Physical Review B*, 69(2), 2004.

[61] H. K. Kashyap and R. Biswas. Ions in a binary asymmetric dipolar mixture: Mole fraction dependent born energy of solvation and partial solvent polarization structure. *Journal of Chemical Physics*, 127(18), 2007.

[62] H. Kovacs and A. Laaksonen. Molecular-dynamics simulation and nmr-study of water acetonitrile mixtures. *Journal of the American Chemical Society*, 113(15):5596–5605, 1991.

[63] H.A. Kramers and W. Heisenberg. über die streuung von strahlung durch atome. *Zeitschrift für Physik A Hadrons and Nuclei*, 31(1):681–708, 1925.

[64] K. M. Lange, U. Bergmann, K. F. Hodeck, R. Konnecke, U. Schade, and E. F. Aziz. Shared solvation of sodium ions in alcohol-water solutions explains the non-ideality of free energy of solvation. *Physical Chemistry Chemical Physics*, 13(34):15423–15427, 2011.

[65] K. M. Lange, K. F. Hodeck, U. Schade, and E. F. Aziz. Nature of the hydrogen bond of water in solvents of different polarities. *Journal of Physical Chemistry B*, 114(50):16997–17001, 2010.

[66] K. M. Lange, R. Könnecke, S. Ghadimi, R. Golnak, M. A. Soldatov, K. F. Hodeck, A. Soldatov, and E. F. Aziz. High resolution x-ray emission spectroscopy of water and aqueous ions using the micro-jet technique. *Chemical Physics*, 377(1-3):1–5, 2010.

[67] K. M. Lange, R. Könnecke, M. Soldatov, R. Golnak, J.-E. Rubensson, A. Soldatov, and E. F. Aziz. On the origin of the hydrogen-bond-network nature of water: X-ray absorption and emission spectra of water-acetonitrile mixtures. *Angewandte Chemie International Edition*, 50(45):10621–10625, 2011.

[68] K. M. Lange, M. Soldatov, R. Golnak, M. Gotz, N. Engel, R. Könnecke, J.-E. Rubensson, and E. F. Aziz. X-ray emission from pure and dilute h_2o and d_2o in a liquid microjet: Hydrogen bonds and nuclear dynamics. *Phys. Rev. B*, 85:155104, 2012.

[69] K.M. Lange, A. Kothe, and E.F. Aziz. Chemistry in solution: Recent techniques and applications using soft x-ray spectroscopy. *Phys. Chem. Chem. Phys.*, 2012.

[70] I. Lauermann, T. Kropp, D. Vottier, A. Ennaoui, W. Eberhardt, and E. F. Aziz. In situ analysis of the zn(s,o) buffer layer preparation for chalcopyrite solar cells by zn l-edge x-ray absorption spectroscopy. *Chemphyschem*, 10(3):532–535, 2009.

[71] R. Lemus, M. Carvajal, J. C. Lopez-V, and A. Frank. Spectroscopic description of h2o in the su(2) vibron model approximation. *Journal of Molecular Spectroscopy*, 214(1):52–68, 2002.

[72] D. J. Livingstone. The characterization of chemical structures using molecular properties. a survey. *Journal of Chemical Information and Computer Sciences*, 40(2):195–209, 2000.

[73] M. P. Ljungberg, A. Nilsson, and L. G. M. Pettersson. Vibrational interference effects in x-ray emission of a model water dimer: Implications for the interpretation of the liquid spectrum. *Journal of Chemical Physics*, 134(4), 2011.

[74] R. Ludwig. Water: from clusters to the bulk. *Angewandte Chemie International Edition*, 40(10):1808–1827, 2001.

[75] G. D. Mahan. Emission-spectra and phonon relaxation. *Physical Review B*, 15(10):4587–4595, 1977.

[76] R. Manne. Molecular orbital interpretation of x-ray emission spectra - simple hydrocarbons and carbon oxides. *Journal of Chemical Physics*, 52(11):5733–, 1970.

[77] Y. Marcus. Ionic-radii in aqueous-solutions. *Chemical Reviews*, 88(8):1475–1498, 1988.

[78] Y. Marcus. Preferential solvation of ions in mixed-solvents .2. the solvent composition near the ion. *Journal of the Chemical Society-Faraday Transactions I*, 84:1465–1473, 1988.

[79] S. Miertus and J. Tomasi. Approximate evaluations of the electrostatic free energy and internal energy changes in solution processes. *Chemical physics*, 65(2):239–245, 1982.

[80] M. Morillo, C. Denk, F. Sanchez-Burgos, and A. Sanchez. Solvation in binary mixtures of dipolar hard sphere solvents: Theory and simulations. *Journal of Chemical Physics*, 113(6):2360–2368, 2000.

[81] T. Mukoyama, K. Taniguchi, and H. Adachi. Interatomic contributions to molecular x-ray-emission rates. *Physical Review B*, 41(12):8118–8121, 1990.

[82] S. Myneni, Y. Luo, L. A. Naslund, M. Cavalleri, L. Ojamae, H. Ogasawara, A. Pelmenschikov, P. Wernet, P. Vaterlein, C. Heske, Z. Hussain, L. G. M. Pettersson, and A. Nilsson. Spectroscopic probing of local hydrogen-bonding structures in liquid water. *Journal of Physics-Condensed Matter*, 14(8):L213–L219, 2002.

[83] L. A. Naslund, M. Cavalleri, H. Ogasawara, A. Nilsson, L. G. M. Pettersson, P. Wernet, D. C. Edwards, M. Sandstrom, and S. Myneni. Direct evidence of orbital mixing between water and solvated transition-metal ions: An oxygen 1s xas and dft study of aqueous systems. *Journal of Physical Chemistry A*, 107(35):6869–6876, 2003. 716NF Times Cited:32 Cited References Count:38.

[84] L. A. Naslund, D. C. Edwards, P. Wernet, U. Bergmann, H. Ogasawara, L. G. M. Pettersson, S. Myneni, and A. Nilsson. X-ray absorption spectroscopy study of the hydrogen bond network in the bulk water of aqueous solutions. *Journal of Physical Chemistry A*, 109(27):5995–6002, 2005.

[85] M. Neeb, J. Rubensson, M. Biermann, and W. Eberhardt. Determination of the exchange splitting of the shape resonance of o2 using the core hole decay spectrum as a "fingerprint.". *Physical Review Letters*, 71(19):3091–3094, 1993.

[86] A. Nilsson, D. Nordlund, I. Waluyo, N. Huang, H. Ogasawara, S. Kaya, U. Bergmann, L. A. Naslund, H. Ostrom, P. Wernet, K. J. Andersson, T. Schiros, and L. G. M. Pettersson. X-ray absorption spectroscopy and x-ray raman scattering of water and ice; an experimental view. *Journal of Electron Spectroscopy and Related Phenomena*, 177(2-3):99–129, 2010.

[87] A. Nilsson, D. Nordlund, I. Waluyo, N. Huang, H. Ogasawara, S. Kaya, U. Bergmann, L. A. Naslund, H. Ostrom, P. Wernet, K. J. Andersson, T. Schiros, and L. G. M. Pettersson. X-ray absorption spectroscopy and x-ray raman scattering of water and ice; an experimental view. *Journal of Electron Spectroscopy and Related Phenomena*, 177(2-3):99–129, 2010.

[88] A. Nilsson and L. G. M. Pettersson. Perspective on the structure of liquid water. *Chemical Physics*, 389:1, 2011.

[89] K. Nishizawa, N. Kurahashi, K. Sekiguchi, T. Mizuno, Y. Ogi, T. Horio, M. Oura, N. Kosugi, and T. Suzuki. High-resolution soft x-ray photoelectron spectroscopy of liquid water. *Physical Chemistry Chemical Physics*, 13(2):413–417, 2011.

[90] J. Nordgren, L. Selander, L. Pettersson, R. Brammer, M. Backstrom, C. Nordling, and H. Ågren. Electronic-structure of benzene studied in usx emission. *Physica Scripta*, 27(3):169–171, 1983.

[91] D. Nordlund, M. Odelius, H. Bluhm, H. Ogasawara, L. G. M. Pettersson, and A. Nilsson. Electronic structure effects in liquid water studied by photoelectron spectroscopy and density functional theory. *Chemical Physics Letters*, 460(1-3):86–92, 2008.

[92] W. L. Obrien, J. Jia, Q. Y. Dong, T. A. Callcott, K. E. Miyano, D. L. Ederer, D. R. Mueller, and C. C. Kao. Phonon relaxation in soft-x-ray emission of insulators. *Physical Review B*, 47(1):140–143, 1993.

[93] M. Odelius. Information content in o[1s] k-edge x-ray emission spectroscopy of liquid water. *Journal of Physical Chemistry A*, 113(29):8176–8181, 2009.

[94] M. Odelius. Molecular dynamics simulations of fine structure in oxygen k-edge x-ray emission spectra of liquid water and ice. *Physical Review B*, 79(14):–, 2009.

[95] M. Ohno and G. A. van Riessen. Hole-lifetime width: a comparison between theory and experiment. *Journal of Electron Spectroscopy and Related Phenomena*, 128(1):1–31, 2003.

[96] L. Onsager. Electric moments of molecules in liquids. *Journal of the American Chemical Society*, 58(8):1486–1493, 1936.

[97] D. Panzer, C. Beck, M. Hahn, J. Maul, G. Schonhense, H. Decker, and E. F. Aziz. Water influences on the copper active site in hemocyanin. *Journal of Physical Chemistry Letters*, 1(10):1642–1647, 2010.

[98] W.W. Parson. *Modern optical spectroscopy: with examples from biophysics and biochemistry*. Springer Verlag, 2007.

[99] J. B. Paul, C. P. Collier, R. J. Saykally, J. J. Scherer, and A. OKeefe. Direct measurement of water cluster concentrations by infrared cavity ringdown laser absorption spectroscopy. *Journal of Physical Chemistry A*, 101(29):5211–5214, 1997.

[100] P. B. Petersen and R. J. Saykally. On the nature of ions at the liquid water surface. *Annual Review of Physical Chemistry*, 57:333–364, 2006.

[101] L. W. Pinkley, P. P. Sethna, and D. Williams. Optical-constants of water in ir - influence of temperature. *Journal of the Optical Society of America*, 67(4):494–499, 1977.

[102] T. Åberg, G. Graeffe, Utriaine.J, and M. Linkoaho. X-ray k-emission spectrum of sodium and of fluorine in some alkali halides. *Journal of Physics Part C Solid State Physics*, 3(5):1112, 1970.

[103] J. E. Rubensson. Rixs dynamics for beginners. *Journal of Electron Spectroscopy and Related Phenomena*, 110(1-3):135–151, 2000.

[104] J. E. Rubensson, L. Petersson, N. Wassdahl, M. Backstrom, J. Nordgren, O. M. Kvalheim, and R. Manne. Radiative decay of multiply excited core hole states in h2o. *Journal of Chemical Physics*, 82(10):4486–4491, 1985.

[105] C. Sandorfy. Anharmonicity and hydrogen bonding. *Journal of Molecular Structure*, 614(1-3):365–366, 2002.

[106] Julian Schwinger. On the classical radiation of accelerated electrons. *Phys. Rev.*, 75:1912–1925, Jun 1949.

[107] R. Seidel, S. Ghadimi, K. M. Lange, S. Bonhommeau, M. A. Soldatov, R. Golnak, A. Kothe, R. Könnecke, A. Soldatov, S. Thürmer, B. Winter, and E. F. Aziz. Origin of dark-channel x-ray fluorescence from transition-metal ions in water. *Journal of the American Chemical Society*, 134(3):1600–1605, 2012.

[108] J. D. Smith, C. D. Cappa, B. M. Messer, W. S. Drisdell, R. C. Cohen, and R. J. Saykally. Probing the local structure of liquid water by x-ray absorption spectroscopy. *Journal of Physical Chemistry B*, 110(40):20038–20045, 2006.

[109] A. K. Soper, G. W. Neilson, J. E. Enderby, and R. A. Howe. Neutron-diffraction study of hydration effects in aqueous-solutions. *Journal of Physics C-Solid State Physics*, 10(11):1793–1801, 1977.

[110] A. J. Stace and A. K. Shukla. Preferential solvation of hydrogen-ions in mixed clusters of water, methanol, and ethanol. *Journal of the American Chemical Society*, 104(20):5314–5318, 1982.

[111] J. Stöhr. *NEXAFS spectroscopy*, volume 25. Springer, 1992.

[112] Y.-P. Sun, F. Hennies, A. Pietzsch, B. Kennedy, T. Schmitt, V. N. Strocov, J Andersson, M. Berglund, J.-E. Rubensson, K. Aidas, F. Gel'mukhanov, M. Odelius, and A. Föhlisch. Intramolecular soft modes and intermolecularinteractions in liquid acetone. *Physical Review B*, 84:132202, 2011.

[113] A. Szent-Györgyi. Welcoming address. *Cell-associated water*, pages 1–2, 1979.

[114] B.K. Teo. *EXAFS: Basic principles and data analysis*, volume 10. Springer-Verlag Berlin, 1986.

[115] A.C. Thompson, D. Vaughan, Center for X-ray optics, and advanced light source. *X-ray data booklet*. Lawrence Berkeley National Laboratory, University of California Berkeley, CA, 2001.

[116] T. Tokushima, Y. Harada, Y. Horikawa, O. Takahashi, Y. Senba, H. Ohashi, L. G. M. Pettersson, A. Nilsson, and S. Shin. High resolution x-ray emission spectroscopy of water and its assignment based on two structural motifs. *Journal of Electron Spectroscopy*

and Related Phenomena, 177(2-3):192–205, 2010.

[117] T. Tokushima, Y. Harada, O. Takahashi, Y. Senba, H. Ohashi, L. G. M. Pettersson, A. Nilsson, and S. Shin. High resolution x-ray emission spectroscopy of liquid water: The observation of two structural motifs. *Chemical Physics Letters*, 460(4-6):387–400, 2008.

[118] T. Tokushima, Y. Harada, O. Takahashi, L. G. M. Shin, Pettersson, S., and A. Nilsson. Comment on "isotope and temperature effects in liquid water probed by x-ray absorption and resonant x-ray emission spectroscopy". *Physical Review Letters*, 100(24), 2008.

[119] Joseph Valasek. X-ray spectroscopic data in regard to the electronic energy bands in potassium and sodium chlorides. *Physical Review*, 53:274–277, 1938.

[120] D. S. Venables and C. A. Schmuttenmaer. Spectroscopy and dynamics of mixtures of water with acetone, acetonitrile, and methanol. *Journal of Chemical Physics*, 113(24):11222–11236, 2000.

[121] L. Weinhardt, O. Fuchs, M. Blum, M. Bär, M. Weigand, J.D. Denlinger, Y. Zubavichus, M. Zharnikov, M. Grunze, C. Heske, and E. Umbach. Resonant x-ray emission spectroscopy of liquid water: Novel instrumentation, high resolution, and the map approach. *Journal of Electron Spectroscopy and Related Phenomena*, 177(2-3):206–211, 2010.

[122] P. Wernet, D. Nordlund, U. Bergmann, M. Cavalleri, M. Odelius, H. Ogasawara, L. A. Naslund, T. K. Hirsch, L. Ojamae, P. Glatzel, L. G. M. Pettersson, and A. Nilsson. The structure of the first coordination shell in liquid water. *Science*, 304(5673):995–999, 2004.

[123] F. L. Wilcox and E. E. Schrier. Salt effects in alcohol-water solutions - application of scaled particle theory to salting-out of polar molecules. *Journal of Physical Chemistry*, 75(24):3757–3761, 1971.

[124] K. R. Wilson, B. S. Rude, J. Smith, C. Cappa, D. T. Co, R. D. Schaller, M. Larsson, T. Catalano, and R. J. Saykally. Investigation of volatile liquid surfaces by synchrotron x-ray spectroscopy of liquid microjets. *Review of Scientific Instruments*, 75(3):725–736, 2004.

[125] B. Winter, E. F. Aziz, U. Hergenhahn, M. Faubel, and I. V. Hertel. Hydrogen bonds in liquid water studied by photoelectron spectroscopy. *Journal of Chemical Physics*, 126(12), 2007.

[126] B. Winter, R. Weber, W. Widdra, M. Dittmar, M. Faubel, and

I. V. Hertel. Full valence band photoemission from liquid water using euv synchrotron radiation. *Journal of Physical Chemistry A*, 108(14):2625–2632, 2004.

[127] M.W. Wong, K.B. Wiberg, and M. Frisch. Hartree–fock second derivatives and electric field properties in a solvent reaction field: Theory and application. *The Journal of chemical physics*, 95:8991, 1991.

[128] Y. F. Zhou, J. H. Morais-Cabral, A. Kaufman, and R. MacKinnon. Chemistry of ion coordination and hydration revealed by a k+ channel-fab complex at 2.0 angstrom resolution. *Nature*, 414(6859):43–48, 2001.

[129] N. F. Zobov, O. L. Polyansky, C. R. LeSueur, and J. Tennyson. Vibration-rotation levels of water beyond the born-oppenheimer approximation. *Chemical Physics Letters*, 260(3-4):381–387, 1996.

List of Figures

Abstract

Spectroscopies using soft X-ray photons allow probing the valence and the unoccupied molecular orbitals of light elements (e.g., carbon, nitrogen, oxygen) through the K-edge and of heavier elements like transition metals (e.g., iron, cobalt, nickel) through the L-edge. As part of this thesis the first membrane-free synchrotron based soft X-ray absorption (XA) and high resolution X-ray emission (XE) spectrometer was built for the investigation liquid samples delivered by a liquid micro-jet. The Rowland circle based spectrometer can cover an emission energy range from 20 eV to 1000 eV. The first proof-of-principle spectra were obtained from pure water and aqueous Ni^{2+} ions.

Hydrogen bonding in liquid water was systematically studied by varying the number of hydrogen bonds per water molecule upon dilution in organic solvents. Using Fourier transform infrared spectroscopy, evidence was provided for the mixing-ratio required for obtaining isolated water molecules in different oxygen-free solvents. This information was used for the further X-ray studies, where acetonitrile was selected as solvent, since it is a pure hydrogen bond acceptor and completely mixable with water. Oxygen K-edge XA and XE spectra of water-acetonitrile mixtures were obtained from a micro-jet. The XA spectrum of pure liquid water shows the characteristic pre-, main- and post-edge structure. Upon decreasing water concentration a strong relative increase and sharpening of the pre- and main-edge features is found. For the XE spectra of pure liquid water a vivid debate prevails concerning the physical origin of an additional spectral feature, which is not observed in the gas phase. Upon decreasing the water concentration, a relative attenuation of this additional feature is observed. The XA and XE spectral changes can be unambiguously related to the increasing amount of broken hydrogen bonds, and the hydrogen bond network of liquid water can thus be addressed on purely experimental grounds. The effect of nuclear dynamics on the absorption and emission spectra of the water-acetonitrile mixtures was investigated by substituting H_2O with D_2O. It has a clearly distinguishable spectral fingerprint compared to the effect of hydrogen bonding.

The special role of water in ionic solutions was investigated by studies of sodium ions dissolved in water, alcohol, and the respective mixed solvents. X-ray absorption spectroscopy on the Na K-edge revealed a shared solvation of the sodium ions in the mixed solvents. Specifically the water component is found to play a key role in stabilizing the solvation shell in these mixed solvents.

Abstract

Spektroskopie mit weicher Röntgenstrahlung ermöglicht die Untersuchung besetzter und unbesetzter Molekülorbitale von leichten Elementen (z.B. C, N, O) durch die K-Kante, oder von schwereren Elementen wie Übergangsmetallen (z.B. Fe, Co, Ni) durch die L-Kante. Im Rahmen dieser Arbeit wurde das erste Membran-freie Absorptions- und hochauflösende Emissionsspektrometer am freien Flüssigkeitsstrahl für weiche Synchrotronstrahlung aufgebaut. Das auf dem Rowland-Kreis basierende Spektrometer kann für Messungen im Energiebereich von 20 eV bis 1000 eV eingesetzt werden. Erste Messungen wurden an reinem Wasser und an Ni^{2+}-Ionen in wässriger Lösung durchgeführt.
Wasserstoffbrückenbindungen im flüssigen Wasser wurden systematisch untersucht, indem deren Anzahl pro Wassermolekül durch Mischung mit organischen Lösungsmitteln variiert wurde. Fourier-Transform-Infrarot-Spektroskopie wurde verwendet, um das Mischungsverhältnis zu bestimmen, ab welchem isolierte Wassermoleküle vorliegen. Für die weiterführenden Röntgenabsorptions- (XA) und Röntgenemissionsmessungen (XE) an der O K-Kante wurde Acetonitril als Lösungsmittel ausgewählt, da es ein reiner Wasserstoffbrücken-Akzeptor und vollständig mit Wasser mischbar ist. Für reines Wasser zeigen die XA Spektren den bekannten Vor-, Haupt- und Nachkanten Peak. Bei abnehmender Wasserkonzentration in den Gemischen wird ein relativer Anstieg und eine Verschmälerung von Vor- und Hauptkante beobachtet. Die XE Spektren von reinem Wasser werden derzeit intensiv diskutiert, aufgrund eines zusätzlichen spektralen Features, welches im Gasphasen-Spektrum nicht auftritt. Die abnehmende Wasserkonzentration geht mit einem relativen Intensitätsabfall dieses zusätzlichen Features einher. Diese Änderungen in den XA und XE Spektren können klar der zunehmenden Anzahl gebrochener Wasserstoffbrückenbindungen pro Wassermolekül zugeordnet werden, wodurch eine Untersuchung des Wasserstoffbrücken-Netzwerkes basierend auf einem rein experimentellen Ansatz möglich wird. Der Einfluss von nuklearer Dynamik auf XA und XE Spektren von Wasser-Acetonitril-Gemischen wurde durch eine vergleichbare Messreihe mit D_2O anstelle von H_2O überprüft. Die dadurch hervorgerufenen spektralen Veränderungen konnten klar von dem Effekt der Wasserstoffbrücken-Koordination unterschieden werden.
Das Verhalten von Wasser in ionischen Lösungen wurde mit einer Studie von Na^+ in Wasser, Alkohol und Gemischen dieser Lösungsmittel untersucht. XA Spektren an der Na K-Kante weisen eine gemeinsame Solvatisiertung der Natriumionen durch beide Lösungsmittel in den Gemischen nach. Es stellte sich heraus, dass Wasser eine Schlüsselrolle bei der Stabilisierung der Solvathülle in den Lösungsmittelgemischen zukommt.

List of publications

Parts of this thesis have been published:

1. **Nature of the Hydrogen Bond of Water in Solvents of Different Polarities**
   Kathrin M. Lange, Kai F. Hodeck, Ulrich Schade, Emad F. Aziz; *Journal of Physical Chemistry B* 114, 16997 (2010)

2. **High Resolution X-Ray Emission Spectroscopy of Water and Aqueous Ions Using the Micro-Jet Technique** *(on the cover)*
   Kathrin M. Lange, René Könnecke, Samira Ghadimi, Ronny Golnak, Mikhail A. Soldatov, Kai F. Hodeck, Alexander Soldatov, Emad F. Aziz; *Chemical Physics* 377, 1-5 (2010)

3. **Shared Solvation of Sodium Ions in Alcohol-Water Solutions Explains the Non-Ideality of Free Energy of Solvation**
   Kathrin M. Lange, Ulf Bergmann, Kai F. Hodeck, René Könnecke, Ulrich Schade and Emad F. Aziz; *Physical Chemistry Chemical Physics* 13, 15423-15427 (2011)

4. **On the Origin of the Hydrogen-Bond-Network Nature of Water: X-Ray Absorption and Emission Spectra of Water-Acetonitrile Mixtures**
   Kathrin M. Lange, René Könnecke, Mikhail Soldatov, Ronny Golnak, Jan-Erik Rubensson, Alexander Soldatov, Emad F. Aziz; *Angewandte Chemie International Edition* 123, 45, 10809-10813 (2011)

5. **Chemistry in Solution: Recent Techniques and Applications of Soft X-ray Spectroscopy** *(on the cover)*
   Kathrin M. Lange, Alexander Kothe, Emad F. Aziz; *Physical Chemistry Chemical Physics* 14, 5331-5338 (2012)

6. **X-ray Emission from Pure and Dilute H_2O and D_2O in a Liquid Microjet: Hydrogen Bonds and Nuclear Dynamics**
   Kathrin M. Lange, Mikhail Soldatov, Ronny Golnak, Malte Gotz, Nicholas Engel, René Könnecke, Jan-Erik Rubensson, Emad Flear Aziz *Physical Review B* 85, 155104 (2012)

During my PhD I contributed to the following publications:

1. **In Situ Investigation of Wet Chemical Processes for Chalcopyrite Solar Cells by L-Edge XAS Under Ambient Condition**
   Stefanie M. Greil, Iver Lauermann , Ahmed Ennaoui, Timo Kropp, Kathrin M. Lange, Matthieu Weber, Emad F. Aziz; *Nuclear Instruments and Methods in Physics Research B.* Vol. 268, 3-4, 263-267 (2010)

2. **On the Enzymatic Activity of Catalase: an X-Ray Absorption Study at the L-Edges of Iron in the Active Centre**
   Nora Bergmann, Sebastien Bonhommeau, Kathrin M. Lange, Stefanie M. Greil, Stefan Eisebitt, Frank de Groot, Majed Chergui and Emad F. Aziz; *Physical Chemistry Chememical Physics* Vol. 12, 18, 4827-4832 (2010).

3. **Charge Transfer to Solvent Identified via Dark Channel Fluorescence Yield L-Edge Spectroscopy**
   Emad F. Aziz, Hannelore Rittmann-Frank, Kathrin M. Lange, Sebastien Bonhommeau, Majed Chergui; *Nature Chemistry* 2, 853-857 (2010)

4. **Breathing Volume into Interfacial Water with Laser Light**
   Andrei P. Sommer, Kai F. Hodeck, Dan Zhu, Alexander Kothe, Kathrin M. Lange, Hans-Joerg Fecht, Emad F. Aziz; *J. Phys. Chem. Lett.*. Vol. 2, 6,562-565 (2011)

5. **Origin of Dark-Channel X-Ray Fluorescence from Transition-Metal Ions in Water**
   Robert Seidel, Samira Ghadimi, Kathrin M. Lange, Sébastien Bonhommeau, Mikhail Soldatov, Ronny Golnak, Alexander Kothe, René Könnecke, Alexander Soldatov, Stephan Thürmer, Bernd Winter, Emad F. Aziz; *Journal of the American Chemical Society.* Vol. 134, 3, 1600-1605 (2012)

6. **Atomic Structure of Cobalt-Oxide Nanoparticles Active in Light-Driven Catalysis of Water Oxidation**
   Marcel Risch, Denys Shevchenko, Magnus F. Anderlund, Stenbjörn Styring Jonathan Heidkamp, Kathrin M. Lange, Anders Thapper, Ivelina Zaharieva; *International Journal of Hydrogen Energy* (2012) DOI:10.1016/j.ijhydene.2012.01.138.

7. **Coster-Kronig Process at the L-Edge of Fe^{2+} Ions in Water: A Sensitive Probe of the Electronic Interactions in Solvents**
   Malte D. Gotz, Mikhail A. Soldatov, Kathrin M. Lange, Nicholas

Engel, Ronny Golnak, René Könnecke, Wolfgang Eberhardt, and Emad F. Aziz; *Submitted*.

8. **On the Origin of the Dips in the Total Fluorescence Yield X-Ray Absorption Spectra of Aqueous Transition Metal Ions**
   Mikhail A. Soldatov, Kathrin M. Lange, Malte D. Gotz, Nicholas Engel, Ronny Golnak, Alexander Kothe, Majed Chergui, Emad F. Aziz; *Submitted*.

9. **The Chemical Bond of the Carbonyl and Sulfinyl Groups Studied by Soft X-ray Spectroscopy and ab Initio Calculations**
   Kaan Atak, Nicholas Engel, Kathrin M. Lange, Ronny Golnak, Malte D. Gotz, Mikhail A. Soldatov, Jan-Erik Rubensson, Nobuhiro Kosugi, Emad F. Aziz; *Submitted*.

Die selbständige und eigenhändige Anfertigung versichere ich an Eides statt.

Berlin, den

Kathrin Maria Lange

Acknowledgement

First of all I would like to thank my supervisor Prof. Emad Flear Aziz. Dear Emad, I am very thankful, that we met three years ago by chance at BESSY and that you made me, like many others after, crazy about science. I don't want to miss this amazing time and this great opportunity. Thanks for all the support and that you always believed in me. I would also like to thank Prof. Holger Dau from the Freie Universität Berlin for being the second referee for my thesis and for giving me a chance to involve in interesting projects on photosynthesis and catalysis. I am very grateful to Prof. Rubensson from Uppsala University. Dear Ruben, thanks a lot for all the long discussions about water, the hydrogen bond and the conspiracy theories behind :) I really learned a lot from you. Thanks a lot to Dr. Ulli Schade, who supervised me for the FT-IR measurements. Thanks Ulli for the knowledge you shared with me. When you want to do experiments at the synchrotron and especially when you want to build up a new setup, you would be usually lost without the support of others. Therefore I would like to thank all the people that were during the last years members of the "Team Aziz" and with whom I spent endless beamtime day- and nightshifts, mixed numerous colorful chemical solutions, and flanged 1001 flanges. First I want to mention Dr. René Könnecke, with whom I build the LiXEdrom spectrometer and who is responsible for a large number of the technical drawings. Dear René, thanks for teaching me so much about XES and Pro Engineer and thanks for all your support, especially for all the times, when you actually wished to be back at home since hours, but I still needed a helping hand and could convince you to stay longer. Special thanks goes to Ronny Golnak, with whom I worked on the myoglobin-project and also a lot on the LiXEdrom and who became after his half year internship, bachelor thesis and now master thesis an inherent part of the group. Speciba to Mikhail Soldatov, for your reliability, your humor and that you always stayed cool, no matter how dangerous the chemical was. Thanks a lot also to Samira Ghadimi, with your good mood and your unlimited motivation you made work fun. Alex Kothe, I thank you for your support, your introduction to Mathematica and all the unbelievable jokes you made. Thanks to Malte Gotz for spending so much effort for the measuring programs, making life much more comfortable now. Thanks a lot to Nick Engel for the linguistic corrections in the last minute. And also to all

the other people that were or are still members of the group for their help: Dr. Kai Hodeck, Dr. Kaan Atak, Munirah Khan, Raul Garcia, Stefanie Greil, Hanni Rittmann-Frank, Britta Höpfner, Guilherme Faria, Agne Sulciute, Rafael Vescovi. A special thanks goes to the people of the BESSY workshop, electronic workshop and the vacuum group: Andreas Drescher, Torsten Wagner, Roland Fleischhauer, Olaf Pawlizki and Christian Kalus, thank you for all the help in the construction process of the LiXEdrom. And thanks a lot to Matthias Mast, whom I could even call in the middle of the night for beamline problems.
During my three years of PhD I was mainly focusing on science, but luckily I had lovely people around me who usually reminded me of more important things in life. Thanks to Katha von Laer, Daniel Kania, Astrid Mauch, Andreas Schuster, Carmen Delgado, Susi Schubert and the Band.
Without my family I would not have achieved all this, therefore thanks to Michaela, Marcus and Jonathan Manhart, Martin and Ise Lange, Tante Anneliese, Cataleen Grimann, Christoph Borch, as well as Anna-Maria and Hannes Lange.